People's Democratic Republic of Algeria
MINISTRY OF HIGHER EDUCATION AND SCIENTIFIC RESEARCH

Ferhat Abbas University - Setif 1

Faculty of Sciences

Department of Physics

**Thesis**

Submitted in partial fulfillment of the requirements for the degree of

**Doctorate ($3^{rd}$ Cycle)**

Field: **Physics**

Specialty: **Theoretical Physics**

By: **KHIAT Imene**

**THEME**

---

# Ionization of atoms and molecules by electron and positron impact: Application to Beryllium atom and Water molecule

---

Publicly defended on 17/02/2026 before the examination committee:

| | | | | |
|---|---|---|---|---|
| Prof. | **Abdelaziz MANSOURI** | Professor | at UFA setif 1 | President |
| Prof. | **Imene KADA** | Professor | at UFA setif 1 | supervisor |
| Prof. | **Salim HOUAMER** | Professor | at UFA setif 1 | Co-supervisor |
| Prof. | **Nourredine MOUSSAOUI** | Professor | at USTHB Alger | Examiner |
| Prof. | **Boumediene LASRI** | Professor | at USMT Saida | Examiner |
| Prof. | **Salah MENOUAR** | Professor | at UFA setif 1 | Examiner |

*To my dear parents, whose love, support, and sacrifices have been my greatest strength. This work is as much theirs as it is mine.*

# Acknowledgements

The doctoral research presented in this thesis was carried out within the Laboratory of Quantum Physics and Dynamical Systems (LPQSD) at Ferhat Abbas University Setif 1.

First and foremost, I express my sincere gratitude to my supervisor, professor Imene Kada, from Ferhat Abbas University Setif 1, for her continuous guidance and important scientific support throughout this research. Her insightful advice and constructive suggestions were instrumental in shaping this thesis.

A special expression of gratitude goes to my co-supervisor, professor Salim Houamer, from Ferhat Abbas University Setif 1. His remarkable efforts, commitment, perseverance, and scientific expertise were invaluable to our group and decisive in the successful completion of this thesis. I am deeply thankful for his exceptional mentorship, unwavering support, encouragement, and continuous presence.

I would also like to extend my deepest gratitude to professor Abdelaziz Mansouri, from Ferhat Abbas University Setif 1, for his support, availability, and valuable contributions throughout this work, recognizing his crucial guidance and feedback as the laboratory director.

My sincere thanks are also addressed to the members of the thesis jury: Professor Nourredine Moussaoui from the University of Science and Technology Houari Boumediene (USTHB) in Algiers, Professor Boumediene Lasri from the University MOULAY TAHAR Of SAIDA (USMT) in Saïda, and Professor Salah Menouar from Ferhat Abbas University Setif 1 (UFAS1), for their time, careful evaluation, and insightful remarks, which significantly contributed to improving the quality of this thesis.

I also wish to acknowledge with deep appreciation my colleagues and friends — Sana Mekhalfa, Ayoub Tamin , Omar Zaidi, Wafa Sakhraoui, and Maroua Attia — members of our research group, for their precious collaboration, assistance in the laboratory, and the many memorable moments we shared. Their friendship, team spirit, and good humor have made these years of research not only productive but also truly enjoyable.

My sincere thanks also go to all members of my family and friends for their support

throughout this long academic journey. In particular, I express my deepest love and gratitude to my sisters Khadidja and Insaf, and my brother Ilyes, for their constant presence, affection, and encouragement.

Finally, I extend my heartfelt thanks to everyone whose generosity, support, and motivation contributed to the realization of this work.

## ملخص

في هذا العمل، تم دراسة كل من التأين الأحادي والتأين المزدوج للذرات والجزيئات. بالنسبة للتأين الأحادي، تم استخدام نموذج $M3CWZ$ لدراسة تأثير شحنة المقذوف على تأين جزيء الماء عند تصادمه بالإلكترونات والبوزيترونات. أما بالنسبة للتأين المزدوج، فقد تم حساب $5DCS$ للذرات و$6DCS$ للجزيئات لدراسة التأين المزدوج لذرة البيريليوم والجزيء الموجه من الماء. وقد أُجريت الدراسات في إطار تقريب بورن وباستخدام نموذج $BBK$ وتقريباته. وتبرز هذه الدراسة أهمية أخذ الترابط الإلكتروني والتفاعلات طويلة المدى بعين الاعتبار من أجل إعادة إنتاج مقاطع التصادم التفاضلية وتوضيح الآليات الأساسية للتأين.



**الكلمات المفتاحية**: التأين، الإرتباط الإلكتروني، جزيء



## Abstract

In this work, both single and double ionization of atoms and molecules were studied. For single ionization, the M3CWZ model was employed to investigate the effects of the charge on the ionization of the water molecule by electron and positron impact. For double ionization, the 5DCS for atoms and 6DCS for molecules were calculated for the beryllium atom and the oriented water molecule. The calculations were performed within the Born approximation and using the BBK model and its approximations. This study emphasizes the importance of accounting for electron correlation and long-range interactions in reproducing differential cross sections and elucidating the underlying ionization mechanisms.



**Keywords:** ionization, correlation, molecule



## Résumé

Dans ce travail, l'ionisation simple et double d'atomes et de molécules a été étudiée. Pour l'ionisation simple, le modèle M3CWZ a été utilisé afin d'étudier les effets de la charge du projectile sur l'ionisation de la molécule d'eau par impact d'électrons et de positrons. Pour l'ionisation double, les 5DCS pour les atomes et 6DCS pour les molécules ont été calculés pour l'atome de béryllium et la molécule d'eau orientée. Les calculs ont été réalisés dans le cadre de l'approximation de Born et en utilisant le modèle BBK et ses approximations. Cette étude souligne l'importance de prendre en compte la corrélation électronique et les interactions à longue portée pour reproduire avec précision les sections efficaces différentielles et clarifier les mécanismes fondamentaux de l'ionisation.



**Mots Clée :** ionisation, corrélation, molécule

# Contents

# List of Figures

# List of Tables

# General Introduction

A significant part of our understanding of the structure of matter has been derived from the study of scattering phenomena. Without such investigations, the microscopic nature of the physical world would have remained largely inaccessible. Through scattering experiments, fundamental constituents of matter, such as the atomic nucleus, nucleons, and quarks have been discovered, providing essential insights into the interactions governing atomic and subatomic systems. Among the various scattering processes, ionization stands out as a fundamental inelastic mechanism, playing a vital role in elucidating the dynamics of atomic and molecular systems. The investigation of ionization induced by electron impact occupies a prominent position in modern atomic and molecular physics, as it leads to the formation of ions and provides an effective means of probing the electronic structure of matter. Moreover, ionization studies offer valuable insights into electron correlation and collision dynamics, which are essential for understanding chemical bonding, predicting reactivity, and characterizing molecular behavior.

Single ionization, in which a single bound electron is removed by an incident projectile, has been extensively investigated, as it represents the most fundamental ionization process. Among the various measurable quantities, the triple differential cross section (TDCS), obtained through coincidence (e,2e) measurements, provides highly detailed information about both the electronic structure of the target and the underlying collision dynamics. For this reason, electron-impact ionization has been studied most intensively, with significant efforts devoted to atomic targets [1, 2]. These studies were later extended to molecular systems. The first coincidence measurements were performed for the (e,2e) ionization of the hydrogen molecule ($H_2$) [3] and were subsequently applied to more complex molecular targets under a variety of kinematic conditions [4–9].

Experimental studies of double ionization are typically conducted through coincidence detection of the scattered electron along with the two ejected ones, in what are known as (e,3e) experiments. These measurements are extremely sensitive to subtle features of collision dynamics but are limited by very small cross sections. Consequently, most investigations have focused on noble gases, particularly helium, due to its simple elec-

tronic structure and suitability for theoretical modeling [10–13]. A related experimental approach, known as the (e,3–1e) measurement, involves the simultaneous detection of only two outgoing electrons—either the scattered and one ejected electron or the two ejected electrons only [14]. While resembling single-ionization (e,2e) experiments, these measurements still provide valuable insights into the mechanisms of double ionization [15].

For positron impact, experimental data remain scarce, mainly due to the inherent limitations of positron beams, including their low intensities, and the complex nature of positron–matter interactions, which involve competing processes such as annihilation and positronium formation [16, 17]. The first investigation of ionization induced by positron impact was conducted by Roy and Etienne in the 1960s, employing a Wilson cloud chamber to measure the specific ionization of nitrogen and argon. Subsequent research efforts expanded upon this pioneering work. For instance, Spicher *et al.* [18] reported the first measurements of positron-impact ionization of atomic hydrogen in the energy range 17.6–600 eV. Earlier studies had also been carried out on helium targets by Sueoka [19], Diana *et al.* [20], and Fromme *et al.* [21].

In recent years, the growing scientific interest in positron-impact ionization has led to significant progress in both experimental techniques and measurement accuracy. Notably, the implementation of triple-coincidence detection systems has enabled precise determination of the double differential cross section (DDCS) and the triple differential cross section (TDCS). Furthermore, the development of advanced reaction microscopes, such as the COLTRIMS (Cold Target Recoil Ion Momentum Spectroscopy) apparatus, has markedly improved experimental resolution, allowing for a more detailed exploration of the underlying collision dynamics and electron–positron correlation effects [22].

On the theoretical side, the description of ionization processes remains a major challenge due to the complexity of electron–electron interactions in the final state. For single ionization known as (e,2e) reaction, numerous perturbative and non-perturbative models have been developed. These developments have led to satisfactory agreement with experimental data across many energy regimes and geometrical configurations. In contrast, the double ionization process, denoted as (e,3e), is even more complex to model, as it constitutes a four-body problem in which two ejected electrons and the scattered projectile evolve within the residual ionic field [23], explicitly involving stronger electron–electron correlation effects [24].

Furthermore, the study of ionization by both positrons and electrons in molecular systems is inherently more complex than in atomic systems, due to the multicenter nature of molecular targets, the orientation dependence of their orbitals, and the additional challenges associated with both experimental measurements and theoretical modeling. Nevertheless, several theoretical approaches have been developed to address these difficulties.

Among them, the molecular three-distorted-wave (M3DW) model has been widely used to describe molecular ionization. This model was later refined by Ali et al. [25], who introduced the multicenter molecular three-body distorted-wave (MCM3DW) approach, in which the continuum electron wave functions explicitly depend on the molecular orientation at the time of ionization. However, in many cases, the inclusion of higher-order Born terms remains essential to achieve better agreement with experimental data, particularly in noncoplanar geometries. More advanced frameworks, such as the continuum-distorted-wave eikonal-initial-state (CDW-EIS) model, explicitly account for higher-order effects and have been successfully applied to calculate TDCS for orbitals such as $1b_1$ and $3a_1$ of $H_2O$ [26].

Double ionization induced by charged particle collisions provides even deeper insights, as it involves the creation of Coulomb four-body excited states, From a theoretical perspective, double ionization is far more complex than single ionization, since it explicitly involves electron correlation and the interplay of multiple interaction channels. The challenge is twofold: (A) as the number of interacting particles increases, the direct evaluation of the full four-body Green's function becomes computationally prohibitive; (B) the non-integrable character of interacting many-particle systems means that analytical treatments are necessarily approximate [23].

Our work is organized as follows:

- **Chapter 1** provides the theoretical framework essential for understanding scattering processes. It establishes the connection between theoretical concepts and experimental observations, beginning with the Schrödinger equation, which governs the scattering phenomenon. The integral form of this equation is then formulated using Green's functions, leading to its general solution and to the derivation of key quantities such as the scattering amplitude, and the differential and total cross sections. The chapter further examines the Born approximation and its various extensions. In the final section, the Schrödinger equation is solved using the partial wave method, which is applied to different scattering scenarios.

- **Chapter 2** is devoted to single and double ionization processes. It introduces the concept of electron correlation in atomic and molecular systems, along with the main wavefunction methods such as Hartree–Fock, and configuration interaction. We then detail single ionization (e,2e) process, emphasizing the structural and dynamical information that can be extracted, as well as double ionization (e,3e) process and its fundamental mechanisms. Finally, the most widely used theoretical models are presented, including the BBK model and the distorted-wave Born approximation (DWBA).

- **Chapter 3** focuses on the double ionization of the beryllium atom by electron impact. The initial and final states are analyzed, and the five-fold differential cross sections are computed using the 2CWG, 2CWWM, and BBK models. This study of the simplest two-valence-electron atom provides a fundamental testbed for understanding electron correlation effects in complex atomic processes.

- **Chapter 4** is dedicated to the ionization of the water molecule. First, we study the effect of the projectile charge (electron or positron) on single ionization using the M3CWZ model. Then, we analyze orientation effects in the double ionization of oriented water molecules by electron impact. Additionally, we investigate how the choice of the target wave function affects both the triple and six-fold differential cross section calculations.

# Bibliography

[1] O. G. de Lucio, S. Otranto, R. E. Olson, and R. D. DuBois. *Phys. Rev. Lett.*, 104:163201, 2010.

[2] O. G. de Lucio and R. D. DuBois. *Phys. Rev. A*, 93:032710, 2016.

[3] R. Dörner, V. Mergel, O. Jagutzki, I. Ullrich, R. Moshammer, and H. Schmidt-Böcking. *Phys. Rep.*, 330:95, 2000.

[4] C. J. Colyer, M. A. Stevenson, O. Al-Hagan, D. H. Madison, C. Ning, and B. Lohmann. *J. Phys. B: At. Mol. Opt. Phys.*, 42:235207, 2009.

[5] L. R. Hargreaves, C. Colyer, M. A. Stevenson, B. Lohmann, O. Al-Hogan, D. H. Madison, and C. G. Ning. *J. Phys. B: At. Mol. Opt. Phys.*, 43:205202, 2010.

[6] A. Naja, E. M. Staicu Casagrande, A. Lahmam-Bennani, M. Nekkab, F. Mezdari, B. Joulakian, O. Chuluunbaatar, and D. H. Madison. *J. Phys. B: At. Mol. Opt. Phys.*, 40:3775, 2007.

[7] D. S. Milne-Brownlie, B. Lohmann S. Cavanagh, C. Champion, P. A. Hervieux, and J. Hanssen. *Phys. Rev. A*, 69:032701, 2004.

[8] I. Toth, L. Nagy, and R. I. Campeanu. *Eur. Phys. J. D*, 68:369, 2014.

[9] D. H. Madison and O. Al-Hagan. *J. At. Mol. Opt. Phys.*, 2010:367180, 2010.

[10] A. Lahmam-Bennani, C. Dupré, and A. Duguet. *Phys. Rev. Lett.*, 63:1582, 1989.

[11] B. El Marji, C. Schröter, A. Duguet, A. Lahmam-Bennani, M. Lecas, and L. Spielberger. *J. Phys. B: At. Mol. Opt. Phys.*, 30:3677, 1997.

[12] C. Schröter, B. El Marji, A. Lahmam-Bennani, A. Duguet, M. Lecas, and L. Spielberger. *J. Phys. B: At. Mol. Opt. Phys.*, 31:131, 1998.

[13] L. K. Jha, K. Santosh, O. P. Roy, and P. Kumar. *Phys. Scr.*, 77:015304, 2008.

[14] B. El Marji, A. Duguet, A. Lahmam-Bennani, M. Lecas, and H. F. Wellenstein. *J. Phys. B: At. Mol. Opt. Phys.*, 28:L733, 1995.

[15] P. O. Löwdin. *Advances in Chemical Physics.* In *Advances in Chemical Physics*, volume 2, page 207. 1959.

[16] R. I. Campeanu. *Nucl. Instrum. Methods Phys. Res. B*, 267(2), 2009.

[17] I. Khiat, S. Houamer, I. Kada, S. Mekhalfa, A. Tamin, and C. Dal Cappello. *Eur. Phys. J. D*, 79:68, 2025.

[18] G. Spicher, B. Olsson, W. Raith, G. Sinapius, and W. Sperber. *Phys. Rev. Lett.*, 64:1019, 1990.

[19] O. Sueoka. *J. Phys. Soc. Jpn.*, 51:3757, 1982.

[20] L. M. Diana, L. S. Fornari, S. C. Sharma, P. K. Pendleton, and P. G. Coleman. In P. C. Jain et al., editors, *Positron Annihilation*, page 342. World Scientific, Singapore, 1985.

[21] D. Fromme, G. Kruse, W. Raith, and G. Sinapius. *Phys. Rev. Lett.*, 57:3031, 1986.

[22] O. Zaidi, A. Mansouri, S. Houamer, A. Tamin, T. Khatir, and C. Dal Cappello. *Eur. Phys. J. D*, 78:140, 2024.

[23] C. Dal Cappello, C. Champion, I. Kada, and A. Mansouri. *Phys. Rev. A*, 83:062716, 2011.

[24] S. M. Bellm, C. J. Colyer, B. Lohmann, and C. Champion. *Phys. Rev. A*, 85:022710, 2012.

[25] E. Ali and D. Madison. *Phys. Rev. A*, 100:012712, 2019.

[26] E. Acebal and S. Otranto. *Eur. Phys. J. D*, 73:91, 2019.

# Chapter 1

# Theoretical Elements

## 1.1 Introduction

Scattering theory is an important and fundamental part of quantum mechanics, which plays a pivotal role in understanding several physical phenomena. Historically, the development of scattering theory began in 1911 with Rutherford's groundbreaking experiments, which led to the discovery of the atomic nucleus through the scattering of alpha particles. This marked the beginning of the formal study of scattering processes, which was later extended within the framework of quantum mechanics.

In its present form, scattering theory describes how a target system interacts with an incoming particle (such as an electron or photon), leading to the emission, absorption, or deflection of particles. The primary purpose of scattering experiments and scattering theory is to extract detailed information about the structure and dynamics of the target through measurements of scattering cross sections.

Scattering theory can be classified into two types depending on whether the kinetic energy of the system is conserved: elastic and inelastic. In elastic scattering, there is no change in kinetic energy or internal states of the system, while in inelastic processes, internal excitations or ionizations appear, which change the energy distribution among the particles.

In this chapter, we present the theoretical foundation for studying scattering phenomena. We begin with a description of scattering phenomena and its relation with the differential cross sections. We proceed to formulate the scattering problem in the general case using the integral form of the Schrödinger equation with Green's functions, and we examine the behavior of the wavefunction for short- and long-range potentials, highlighting the challenges posed by each. Finally, we introduce the Born approximation, which provides a perturbative method for solving scattering problems under appropriate

conditions.

## 1.2 Scattering Theory and Cross Sections

### 1.2.1 Description of the Scattering Phenomenon

In a scattering experiment, a beam of particles is directed at a target material to observe how collisions occur. The total number of collisions depends on both the intensity of the incoming beam and the number of target particles encountered per unit area of the beam path. While some incident particles pass through unaffected, others are scattered at various angles, as illustrated in Figure 1.1.

The distribution of these scattered particles across different directions is described by the differential cross section, $\mathrm{d}\sigma(\theta, \phi)$, which represents the number of particles scattered into a specific solid angle element $\mathrm{d}\Omega$ per unit time and per unit incident flux $F_{\text{inc}}$. The solid angle element is defined as:

$$\mathrm{d}\Omega = \sin\theta \, \mathrm{d}\theta \, \mathrm{d}\phi$$

This leads to the formal definition of the differential cross section [1, 2]:

$$\frac{\mathrm{d}\sigma}{\mathrm{d}\Omega} = \frac{1}{F_{\text{inc}}} \frac{\mathrm{d}n(\theta, \phi)}{\mathrm{d}\Omega} \tag{1.1}$$

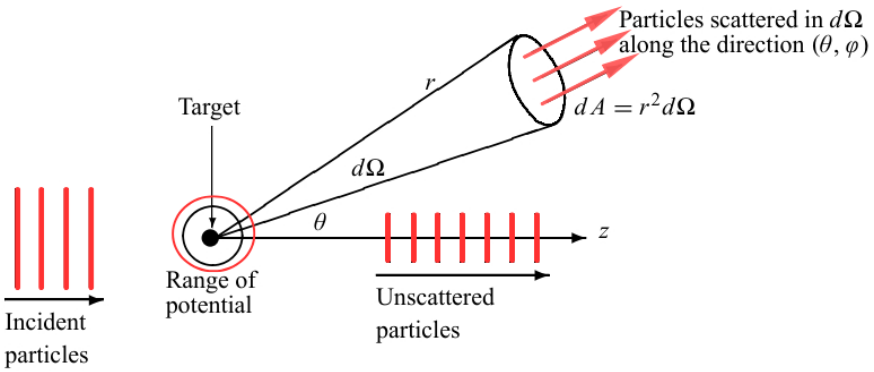


**Figure 1.1:** Scattering of incident beam from a fixed target, with the scattered particles detected within a solid angle in a specific direction.

The total cross section $\sigma$ represents the integrated probability of scattering into all possible directions. It is obtained by integrating the differential cross section over the full

solid angle:

$$\sigma = \int \frac{\mathrm{d}\sigma}{\mathrm{d}\Omega}\,\mathrm{d}\Omega = \int_0^{\pi} \sin\theta\,\mathrm{d}\theta \int_0^{2\pi} \frac{\mathrm{d}\sigma(\theta,\phi)}{\mathrm{d}\Omega}\,\mathrm{d}\phi \tag{1.2}$$

Differential cross sections offer a deeper insight into scattering processes than total cross sections, as they depend not only on the energy of the particles but also on the directions in which these particles are ejected or scattered.

It should be noted that in experimental setups, measurements are typically carried out in the laboratory (Lab) frame, where the target is at rest and the projectile is incident with a given momentum. In contrast, theoretical calculations are often performed in the center-of-mass (CM) frame, where the total momentum of the system is zero. This characteristic makes the CM frame more convenient for analyzing scattering angles and energy distributions [1, 2].

## 1.3 Integral Form of the Schrödinger Equation Using the Green's Function

Let us consider the scattered of a two-particle system of masses $m_1$ and $m_2$. The time-independent Schrödinger equation is given by:

$$\left(-\frac{\hbar^2}{2m_1}\nabla_1^2 - \frac{\hbar^2}{2m_2}\nabla_2^2 + V(\vec{r}_1,\vec{r}_2)\right)\Phi(\vec{r}_1,\vec{r}_2) = E\,\Phi(\vec{r}_1,\vec{r}_2) \tag{1.3}$$

where $V(\vec{r}_1,\vec{r}_2)$ is the interaction potential between the two particles. We take the case where the interaction between $m_1$ and $m_2$ depends only on their relative distance $r = |\vec{r}_1 - \vec{r}_2|$, then the problem reduces to solving the relative motion of two particles: One describes the center-of-mass (CM) motion, which behaves as a free particle of total mass $M = m_1 + m_2$. The other corresponds to a fictitious particle of reduced mass $\mu = \dfrac{m_1 m_2}{m_1 + m_2}$, moving under the influence of the potential $V(\vec{r})$. Then Eq. 1.3 will be:

$$\left(-\frac{\hbar^2}{2M}\nabla_{\vec{R}}^2 - \frac{\hbar^2}{2\mu}\nabla_{\vec{r}}^2 + V(\vec{r})\right)\Phi(\vec{R},\vec{r}) = E\,\Phi(\vec{R},\vec{r}) \tag{1.4}$$

One way to solve the previous equation is to look for a solution of the wavefunction $\Phi(\vec{R},\vec{r})$ in the form:

$$\Phi(\vec{r},\vec{R}) = \varphi(\vec{R})\,\psi(\vec{r}) \tag{1.5}$$

Since our objective is to determine the differential cross section in terms of the scattering amplitude of the scattered wave, the contribution associated with the center-of-mass (CM)

motion will not be considered further in this context, then Eq. 1.4 will be:

$$-\frac{\hbar^2}{2\mu}\nabla^2\psi(\vec{r}) + V(\vec{r})\psi(\vec{r}) = E\psi(\vec{r}) \tag{1.6}$$

Rewriting this equation by moving the potential term to the right-hand side, we obtain:

$$\nabla^2\psi(\vec{r}) + \frac{2\mu E}{\hbar^2}\psi(\vec{r}) = \frac{2\mu V(\vec{r})}{\hbar^2}\psi(\vec{r}) \tag{1.7}$$

We define the following quantities:

$$k^2 = \frac{2\mu E}{\hbar^2} \quad \text{and} \quad Q(\vec{r}) = \frac{2\mu V(\vec{r})}{\hbar^2}\psi(\vec{r}),$$

which simplifies Eq. (1.7) into the Helmholtz-type form:

$$\left(\nabla^2 + k^2\right)\psi(\vec{r}) = Q(\vec{r}), \tag{1.8}$$

This is an inhomogeneous differential equation, where the source term $Q(\vec{r})$ itself depends on $\psi(\vec{r})$, To solve it, we introduce the Green's function $G(\vec{r})$ obtained by solving the point source equation:

$$\left(\nabla^2 + k^2\right)G(\vec{r}) = \delta^3(\vec{r}) \tag{1.9}$$

then, the solution to expression (1.8) can be written as:

$$\Psi(\vec{r}) = \int d^3r' G(\vec{r} - \vec{r}')Q(\vec{r}') \tag{1.10}$$

where $Q(\vec{r})$ can be express as:

$$Q(\vec{r}) = \int d^3r'\delta^3(\vec{r} - \vec{r}')Q(\vec{r}') = \int d^3r'(\nabla^2 + k^2)G(\vec{r} - \vec{r}')Q(\vec{r}') \tag{1.11}$$

To compute $G(\vec{r})$ , we switch to the Fourier space [3] by multiplying Eq. (1.9) by $e^{i\vec{q}\cdot\vec{r}}$ and integrating over all space:

$$\int(\nabla^2 + k^2)G(\vec{r})e^{i\vec{q}\cdot\vec{r}}d^3r = \int \delta^3(\vec{r})e^{i\vec{q}\cdot\vec{r}}d^3r = 1 \tag{1.12}$$

After integration by parts and using properties of the Laplacian in Fourier space, we obtain:

$$(k^2 - q^2)G(\vec{q}) = 1 \tag{1.13}$$

therefore, giving the following expression for $G(\vec{q})$ gives:

$$G(\vec{q}) = \frac{1}{k^2 - q^2} = \frac{1}{(k-q)(k+q)} \tag{1.14}$$

From Eq. (1.14) , and using the inverse Fourier transformation, $G(\vec{r})$ reads:

$$\begin{aligned}
G(\vec{r}) &= \frac{1}{(2\pi)^3}\int \frac{e^{-i\vec{q}\cdot\vec{r}}}{k^2-q^2}d^3q = \frac{1}{(2\pi)^3}\int \frac{e^{-iqr\cos(\theta)}}{k^2-q^2}q^2dq\sin(\theta)d\theta d\phi \\
&= \frac{1}{(2\pi)^3}\int_0^{2\pi} d\phi \int_0^{\pi} d\theta \frac{q^2}{k^2-q^2}\sin(\theta)e^{-iqr\cos(\theta)}dq \\
&= \frac{1}{(2\pi)^2}\int dq \frac{q^2}{k^2-q^2}\int_0^{\pi}\sin(\theta)e^{-iqr\cos(\theta)}d\theta, \\
&= -\frac{1}{(2\pi)^2}\int dq \frac{q^2}{k^2-q^2}\left[\frac{e^{-iqru}}{-iqr}\right]_{-1}^{1} \\
&= \frac{1}{(2\pi)^2}\int dq \frac{q^2}{k^2-q^2}\frac{e^{iqr}-e^{-iqr}}{iqr} \\
&= \frac{1}{(2\pi)^2}\frac{1}{iqr}\int_{-\infty}^{\infty} dq \frac{q^2}{k^2-q^2}(e^{iqr}-e^{-iqr}) \\
&= \frac{1}{4\pi^2 r}\int_0^{\infty} dq \frac{q}{k^2-q^2}(e^{iqr}-e^{-iqr}) \\
&= \frac{i}{8\pi^2 r}\int_{-\infty}^{\infty} dq \frac{q}{k^2-q^2}(e^{iqr}-e^{-iqr})
\end{aligned} \tag{1.15}$$

Finally giving $G(\vec{r})$ in terms of two complex integrals from the above expression as follows:

$$\begin{aligned}
G(\vec{r}) &= \frac{i}{8\pi^2 r}\left[\int_{-\infty}^{+\infty}\frac{qe^{iqr}}{q^2-k^2}dq - \int_{-\infty}^{+\infty}\frac{qe^{-iqr}}{q^2-k^2}dq\right] \\
&= \frac{i}{8\pi^2 r}\left[\int_{-\infty}^{+\infty}\frac{qe^{iqr}}{(q-k)(q+k)}dq - \int_{-\infty}^{+\infty}\frac{qe^{-iqr}}{(q-k)(q+k)}dq\right]
\end{aligned} \tag{1.16}$$

The above integrals can be written as contour integrals. Then, $G(\vec{r})$ evaluates to:

$$G(\vec{r}) = \frac{i}{8\pi^2 r}\left[\oint_{C_+}\frac{qe^{iqr}}{(q-k)(q+k)}dq - \oint_{C_-}\frac{qe^{-iqr}}{(q-k)(q+k)}dq\right] \tag{1.17}$$

where the contours $C_+$ (anti-clockwise orientation) and $C_-$ (clockwise orientation) are defined as in Figure 1.2.

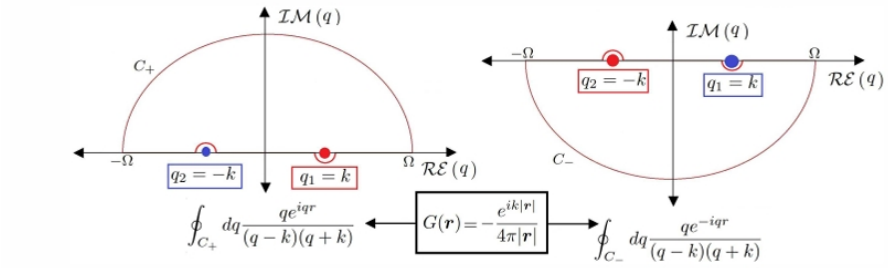


**Figure 1.2:** Definitions of the contours $C_+$ and $C_-$, to evaluate the contour integrals appearing in the evaluation of the Green's function $G(\vec{r})$.

By using the residue theorem, $G(\vec{r})$ can be calculated as follows:

$$\begin{aligned} G(\vec{r}) &= \frac{i}{8\pi^2 r}\left[2\pi i\left(\frac{qe^{iqr}}{q+k}\right)_{q=k} - (-2\pi i)\left(\frac{qe^{-iqr}}{q-k}\right)_{q=-k}\right] \\ &= \frac{i}{8\pi^2 r}\left[2\pi i\left(\frac{ke^{ikr}}{2k}\right) + 2\pi i\left(\frac{(-k)e^{-i(-k)r}}{(-2k)}\right)\right] \end{aligned} \tag{1.18}$$

giving:

$$G(\vec{r}) = \frac{i}{8\pi^2 r}(2\pi i)e^{ikr} = -\frac{e^{ik|\vec{r}|}}{4\pi|\vec{r}|} \tag{1.19}$$

Knowing $G(\vec{r})$, the particular solution to equation 1.6 is given by:

$$\begin{aligned} \Psi_p(\vec{r}) &= \int d^3r' G(\vec{r}-\vec{r}')Q(\vec{r}') \\ &= \int d^3r'\left(\frac{e^{ik|\vec{r}-\vec{r}'|}}{4\pi|\vec{r}-\vec{r}'|}\right)\frac{2\mu V(\vec{r}')}{\hbar^2}\Psi(\vec{r}') \\ &= -\frac{\mu}{2\hbar^2\pi}\int \frac{e^{ik|\vec{r}-\vec{r}'|}}{|\vec{r}-\vec{r}'|}V(\vec{r}')\Psi(\vec{r}')d^3r' \end{aligned} \tag{1.20}$$

As for the solution to the homogeneous part of Eq. 1.6, denoted by $\Psi_h(\vec{r})$, it can be obtained from:

$$(\nabla^2 + k^2)\Psi_h(\vec{r}) = 0 \tag{1.21}$$

then, the total solution to Eq. 1.6 is given by:

$$\Psi(\vec{r}) = \Psi_h(\vec{r}) - \frac{\mu}{2\hbar^2\pi}\int \frac{e^{ik|\vec{r}-\vec{r}'|}}{|\vec{r}-\vec{r}'|}V(\vec{r}')\Psi(\vec{r}')d^3r' \tag{1.22}$$

This is the standard Lippmann–Schwinger equation in position space.

### Short-Range Potentials

In what follows, we restrict our analysis to the case of *elastic scattering*, where the t otal kinetic energy of the system remains constant and no internal excitation or ionization takes place. This assumption is made for simplicity and is appropriate for a wide range of scattering problems involving short-range interactions. Under elastic conditions, the wave number $k = \sqrt{\frac{2\mu E}{\hbar^2}}$ remains the same before and after the collision. This choice simplifies the mathematical formulation and lays the groundwork for later introducing the asymptotic behavior of the wavefunction and the definition of the scattering amplitude.

In the context of scattering theory, a potential $V(\vec{r})$ is considered *short-range* if it becomes negligible as the distance from the scattering center increases [4]. More precisely, a potential is short-range if it decays faster than $1/r$ as $r \to \infty$, that is:

$$\lim_{r\to\infty} r^n V(r) = 0 \quad \text{for some } n > 1 \tag{1.23}$$

### Asymptotic Behavior of the Wavefunction

Let us now analyze the behavior of the wavefunction $\Psi(\vec{r})$ at large distances, assuming the potential is localized around the origin (i.e., significant only for small $|\vec{r}'|$).

Suppose $\vec{r}$ denotes the position of the detector (far away), and $\vec{r}'$ is a point within the interaction region. In the far-field limit, we assume $|\vec{r}| \gg |\vec{r}'|$. Then we can expand:

$$|\vec{r} - \vec{r}'|^2 = r^2 - 2\vec{r}\cdot\vec{r}' + |\vec{r}'|^2 \approx r^2 - 2\vec{r}\cdot\vec{r}' \tag{1.24}$$

so that:

$$|\vec{r} - \vec{r}'| \approx r - \hat{r}\cdot\vec{r}' \tag{1.25}$$

where $\hat{r} = \vec{r}/r$ is the unit vector in the direction of $\vec{r}$.

Now, if we define the wavevector of the scattered particle as $\vec{k} = k\hat{r}$, then:

$$e^{ik|\vec{r}-\vec{r}'|} \approx e^{ikr} e^{-ik\hat{r}\cdot\vec{r}'} \tag{1.26}$$

This approximation is called the far-field or asymptotic approximation. Thus, the central term in the integral equation becomes:

$$\frac{e^{ik|\vec{r}-\vec{r}'|}}{|\vec{r}-\vec{r}'|} \approx \frac{e^{ikr}}{r} e^{-i\vec{k}\cdot\vec{r}'} \tag{1.27}$$

Substituting this into the integral equation gives:

$$\Psi(\vec{r}) \approx \Psi_h(\vec{r}) + \left( -\frac{\mu}{2\pi\hbar^2} \int e^{-i\vec{k}\cdot\vec{r}'} V(\vec{r}') \Psi(\vec{r}') \, d^3r' \right) \frac{e^{ikr}}{r} \tag{1.28}$$

which can be written as:

$$\Psi(\vec{r}) \approx \Psi_h(\vec{r}) + f(\theta, \phi) \frac{e^{ikr}}{r} \tag{1.29}$$

where $f(\theta, \phi)$ is called the *scattering amplitude*.

In Dirac representation, this amplitude is:

$$f(\theta, \phi) = -\frac{\mu}{2\pi\hbar^2} \langle e^{i\vec{k}\cdot\vec{r}} | V | \Psi \rangle \tag{1.30}$$

The scattering amplitude $f(\theta, \phi)$ encapsulates how the incident wave is modified by the potential.

### 1.3.1 Scattering Amplitude

The number $dn(\theta, \phi)$ of particles scattered into a solid angle element $d\Omega$ in the direction $(\theta, \phi)$, and passing through a surface element $dA = r^2 \, d\Omega$ per unit time, is given by [1, 5]:

$$dn = F_{\text{sc}} \cdot r^2 \, d\Omega \tag{1.31}$$

By substituting Eq. 1.31 into Eq. 1.1, we obtain:

$$\frac{d\sigma}{d\Omega} = \frac{F_{\text{sc}}}{F_{\text{inc}}} \, r^2 \tag{1.32}$$

The incident $F_{inc}$ and scattered $F_{sc}$ flux densities are defined as follows [1, 5, 6]:

$$\vec{F}_{inc} = \frac{i\hbar}{2\mu} \left[ \Psi_{inc}(\vec{r}) \, \vec{\nabla} \Psi^*_{inc}(\vec{r}) - \Psi^*_{inc}(\vec{r}) \, \vec{\nabla} \Psi_{inc}(\vec{r}) \right] = \frac{\hbar k_i}{\mu} \tag{1.33}$$

$$\vec{F}_{sc} = \frac{i\hbar}{2\mu} \left[ \Psi_{sc}(\vec{r}) \, \vec{\nabla} \Psi^*_{sc}(\vec{r}) - \Psi^*_{sc}(\vec{r}) \, \vec{\nabla} \Psi_{sc}(\vec{r}) \right] = \frac{\hbar k_f}{\mu r^2} \, |f_k(\theta, \phi)|^2 \tag{1.34}$$

Substituting Eqs. 1.33 and 1.34 into Eq. 1.32, we finally obtain:

$$\frac{d\sigma}{d\Omega}(\theta, \phi) = \frac{k_f}{k_i} \, |f_k(\theta, \phi)|^2 \tag{1.35}$$

where $f_k$ is the transition amplitude from the initial state to the final state. The calculation of this quantity can be straightforward in some cases, but it may become quite

complicated in others, depending on the physical model used.

For an elastic collision ($k_i = k_f$):

$$\frac{d\sigma}{d\Omega}(\theta,\phi) = |f_k(\theta,\phi)|^2 \tag{1.36}$$

## 1.4 Born Approximation

The Born approximation is an important method in quantum scattering theory, originally introduced by Max Born in 1926 [7]. In this approach, the scattering potential is treated as a weak perturbation [8], allowing the scattering amplitude to be obtained through a perturbative expansion of the wave function. .

In this approximation, it is assumed that the scattering potential describing the Coulomb interaction between the projectile and the target is small compared to the total energy of the target and the incident electron, and can therefore be treated as a perturbation (the free Hamiltonian dominates over the perturbation). Consequently, the incident and scattered particles are represented by plane waves. In this case, Eq. 1.22 is defined in terms of the Green's function as follows:

$$\Psi(\vec{r}) = e^{i\vec{k}_i\cdot\vec{r}} + \int d^3r' G_+(\vec{r}-\vec{r}')U(\vec{r}')\Psi(\vec{r'}) \tag{1.37}$$

where

$$U(\vec{r}) = \frac{2\mu V(\vec{r})}{\hbar^2}$$

in other hand $\Psi(\vec{r'})$ can be written as:

$$\Psi(\vec{r'}) = e^{i\vec{k}_i\cdot\vec{r'}} + \int d^3r'' G_+(\vec{r'}-\vec{r''})U(\vec{r''})\Psi(\vec{r''}) \tag{1.38}$$

thus Eq. 1.37 becomes

$$\Psi(\vec{r}) = e^{i\vec{k}_i\cdot\vec{r}} + \int d^3r' G_+(\vec{r}-\vec{r}')U(\vec{r}')e^{i\vec{k}_i\cdot\vec{r'}} + \int d^3r' G_+(\vec{r}-\vec{r}')U(\vec{r}')\int d^3r'' G_+(\vec{r'}-\vec{r''})U(\vec{r''})\Psi(\vec{r''}) \tag{1.39}$$

And similarly for $\Psi(\vec{r''})$ and$\Psi(\vec{r'''})$ ..., we can write then

$$\begin{aligned}\Psi(\vec{r}) = e^{i\vec{k}_i\cdot\vec{r}} &+ \int d^3r' G_+ U e^{i\vec{k}_i\cdot\vec{r'}} + \int d^3r' G_+ U \int d^3r'' G_+ U(\vec{r''}) e^{i\vec{k}_i\cdot\vec{r''}} \\ &+ \int d^3r' G_+ U \int d^3r'' G_+ U \int d^3r''' G_+ U e^{i\vec{k}_i\cdot\vec{r'''}} + \dots\end{aligned} \tag{1.40}$$

This expansion is known as the Born series. In practice, only the first two terms are typically retained (referred to as the first Born term ($f_{B1}$) and the second Born term ($f_{B2}$)). The leading contribution is provided by the first Born term, while the second Born term serves as a correction to account for higher-order effects. However, the computation of the second term is significantly more complex and requires considerable numerical effort. Terms of higher order are generally neglected, as their calculation becomes impractical and their overall contribution is negligible.

### 1.4.1 Calculation of the First Born Term

The first Born approximation retains only the first term of the previous expansion, neglecting the contribution of terms with powers higher than 1; that is $\Psi(\vec{r})$ is given by:

$$\Psi(\vec{r}) = e^{i\vec{k}_i\cdot\vec{r}} + \int d^3r' G_+(\vec{r}-\vec{r}')U(\vec{r}')e^{i\vec{k}_i\cdot\vec{r}'} \tag{1.41}$$

Thus, we can write the scattering amplitude and the differential cross section in the first Born approximation as follows:

$$f_{B1}(\theta,\phi) = -\frac{\mu}{2\pi\hbar^2}\int e^{-i\vec{k}\cdot\vec{r}'}V(\vec{r}')e^{i\vec{k}_i\cdot\vec{r}'})\, d^3r' \tag{1.42}$$

$$\frac{d\sigma}{d\Omega} = \frac{\mu^2}{4\pi^2\hbar^4}|\int e^{i\vec{q}\cdot\vec{r}'}V(\vec{r}')e^{i\vec{k}_i\cdot\vec{r}'})\ d^3r'|^2 \tag{1.43}$$

where $\hbar\vec{k_i}$ and $\hbar\vec{k}$ are the linear momenta of the incident and scattered particles, respectively; and $\hbar\vec{q}$ is the momentum transfer $\vec{q} = \vec{k}_i - \vec{k}$

#### 1.4.1.1 Validity of the First Born Approximation

The first Born approximation remains reliable when the total wavefunction $\psi(\vec{r})$ departs only slightly from the incoming plane wave. In other words, the correction term to the plane-wave solution must be much smaller than the leading term:

$$\left|\frac{\mu}{2\pi\hbar^2}\int\frac{e^{ik|\vec{r}-\vec{r}'|}}{|\vec{r}-\vec{r}'|}V(r')\,e^{i\vec{k}_i\cdot\vec{r}'}\,d^3r'\right| \ll |\phi_{\text{inc}}(\vec{r})|^2 \tag{1.44}$$

Since the incident wave is $\phi_{\text{inc}} = e^{i\vec{k}_0\cdot\vec{r}}$, the criterion simplifies to:

$$\left|\frac{\mu}{2\pi\hbar^2}\int\frac{e^{ik|\vec{r}-\vec{r}'|}}{|\vec{r}-\vec{r}'|}V(r')\,e^{i\vec{k}_i\cdot\vec{r}'}\,d^3r'\right| \ll 1 \tag{1.45}$$

For elastic scattering ($k_i = k$) and assuming the interaction potential is strongest near the origin, one obtains:

$$\left| \frac{\mu}{\hbar^2} \int_0^\infty r' e^{ikr'} V(r')\, dr' \int_0^\pi e^{ikr' \cos\theta'} \sin\theta' d\theta' \right| \ll 1 \tag{1.46}$$

or equivalently,

$$\left| \frac{\mu}{\hbar^2 k} \int_0^\infty V(r') \left(e^{2ikr'} - 1\right) dr' \right| \ll 1 \tag{1.47}$$

Because the projectile's kinetic energy is $E_i = \hbar^2 k^2/(2\mu)$, these expressions show that the Born approximation applies when the incoming particle is fast and the potential is weak. In practical terms, whenever the average interaction energy between the particle and the scattering potential is much smaller than the particle's incident kinetic energy, the scattered wave can be regarded as a plane wave.

### 1.4.2 Calculation of the Second Born Term

For the calculation of the second Born approximation, we retain also the second term of the expansion given in Eq. 1.39

$$\Psi(\vec{r}) = \int d^3r' G_+(\vec{r} - \vec{r'}) U(\vec{r'}) \int d^3r'' G_+(\vec{r'} - \vec{r''}) U(\vec{r''}) \Psi(\vec{r''}) \tag{1.48}$$

Then we can write the scattering amplitude and the differential cross section in the second Born approximation as follows

$$f_{B2}(\theta, \phi) = -\frac{\mu}{2\pi\hbar^2} \int e^{-i\vec{k}\cdot\vec{r}} V(\vec{r}) \left[ \int e^{i\vec{k}_i \cdot \vec{r}'} G_+(\vec{r} - \vec{r'}) V(\vec{r'})\, d\vec{r'} \right] d\vec{r} \tag{1.49}$$

$$\frac{d\sigma}{d\Omega} = \frac{\mu^2}{4\pi^2\hbar^4} \left| \int e^{-i\vec{k}\cdot\vec{r}} V(\vec{r}) \left[ \int e^{i\vec{k}_i \cdot \vec{r}'} G_+(\vec{r} - \vec{r'}) V(\vec{r'})\, d\vec{r'} \right] d\vec{r} \right|^2 \tag{1.50}$$

In **Born 2** The system undergoes two successive interactions. Under the effect of the potential $V(\vec{r})$, the initial state evolves into an intermediate state, which, under the action of the potential $V(\vec{r})$, then evolves into the final state.

Thus, the first Born approximation is valid only when we consider a single interaction of the projectile with the target, as in the case of ionizing collisions of atomic or molecular targets by electrons whose velocity is much greater than that of the electrons bound to the target [9–11].

## 1.5 Partial Wave Solution of the Schrödinger Equation

In this section, we present the solution of the Schrödinger equation obtained using the partial wave expansion method, which describes the wavefunction of an electron moving in a radial potential field $V(r)$, either Coulombic or distorted.

The general solution $\psi(\vec{k},\vec{r})$ of the Schrödinger Eq. 1.6, in spherical coordinates, is expressed as a linear combination of partial waves [12, 13] as:

$$\psi(\vec{k},\vec{r}) = \sum_{l} C_l \, R_l(k,r) \, P_l(\cos\alpha) \tag{1.51}$$

where $R_l(k,r)$ is the radial part of the wavefunction, and $P_l(\cos\alpha)$ is the Legendre polynomial [14] that explicitly depends on the angle $\alpha$ between $\vec{k}$ and $\vec{r}$. It should be noted that the partial wave expansion is particularly useful when the Schrödinger equation for a particle in a potential $V(r)$ does not have an analytical solution, as it allows the wavefunction to be separated into a radial part and spherical harmonics.

### Case of a Free Particle

In this case, where the interaction potential vanishes ($V = 0$), the solusion simplifies to that of a free particle, which can be represented by a plane wave $\psi_p$:

$$\psi_p(\vec{k},\vec{r}) = \frac{1}{(2\pi)^{3/2}} e^{i\vec{k}\cdot\vec{r}} \tag{1.52}$$

### Case of a Coulomb Potential

In the case of a Coulomb potential; during a collision between a nucleus of charge $Z$ and an electron located at a distance $r$, the solution 1.51 take the forme:

$$\psi_c(\vec{k},\vec{r}) = 4\pi \sum_{l,m} i^l e^{-i\delta_l} Y^*_{lm}(\hat{k}) \, Y_{lm}(\hat{r}) \, F_l(k,r) \tag{1.53}$$

where $Y_{lm}(\hat{k})$ and $Y_{lm}(\hat{r})$ are complex spherical harmonics, and $\delta_l$ is the Coulomb phase shift, which is the angular change in solution relative to a plane wave [15]. Here, $\Gamma$ denotes the Gamma function, $\eta = \frac{Z}{k}$ is the Sommerfeld parameter for a purely Coulombic potential, and $F_l(k,r)$ is the radial hypergeometric function.

### Case of a Distortion Potential

The spherically symmetric distortion potential $V(r)$, representing the total interaction composed of Coulomb and short-range terms, leads to the following form of the continuum wavefunctions:

$$\psi_d(\vec{k},\vec{r}) = \frac{4\pi}{(2\pi)^{\frac{3}{2}}} \sum_{l,m} i^l e^{i\delta_l} \frac{\chi_l(k,r)}{kr} Y^*_{l,m}(\hat{k}) Y_{l,m}(\hat{r}) \tag{1.54}$$

where $\alpha$ is the angle between $\vec{k}$ and $\vec{r}$, $\delta_l$ is the phase shift, and $\chi_l(k,r)$ is the radial function.

## 1.6 Conclusion

In this chapter, we established the foundational framework of scattering theory, which serves as the theoretical backbone for understanding ionization processe in atomic and molecular systems. We began with a conceptual description of the scattering phenomenon and introduced key observables such as the differential and total cross sections.

We then examined the formal solution of the Schrödinger equation using Green's functions. The behavior of the wavefunction at large distances, particularly its asymptotic form, was shown to be directly related to the scattering amplitude, and thus determines the expression of the cross section. We also presented the Born approximation series, emphasizing its perturbative nature and its range of validity. Finally, we introduced the case of a particle moving in an arbitrary radial potential, presenting the corresponding solution of the Schrödinger equation through the partial wave approach.

This theoretical framework will be the basis for more advanced models and practical applications in the following chapters, where we study the ionization of atoms and molecules under various impact conditions and energy regimes.

# Bibliography

[1] N. Zettili. *Quantum Mechanics: Concepts and Applications*. Wiley, 2009.

[2] M. Le Bellac. *Physique quantique – Fondements (Tome 1)*. CNRS Éditions, 2013.

[3] M. Pinsky. *Introduction to Fourier Analysis and Wavelets*. Brooks/Cole, 2002.

[4] B. Najjari. PhD thesis, University of Lorraine, 1997.

[5] T. Khatir. PhD thesis, University of Setif 1, 2021.

[6] M. Le Bellac. *Physique quantique, Tome II : Applications et exercices corrigés*. CNRS Éditions, Paris, 2013.

[7] M. Born. *Z. Phys.*, 38:803–827, 1926.

[8] T. A. van der Sijs, O. El Gawhary, and H. P. Urbach. *Phys. Rev. Research*, 2:013308, 2020.

[9] H. Ehrhardt, M. Fischer, and K. Jung. *Z. Phys. A*, 304:119, 1982.

[10] F. W. Byron Jr., C. J. Joachain, and B. Piraux. *J. Phys. B: At. Mol. Opt. Phys.*, 13:L673, 1980.

[11] M. J. Brother and R. A. Bonham. *J. Phys. B: At. Mol. Opt. Phys.*, 17:4235, 1980.

[12] S. Weinberg. *Lectures on Quantum Mechanics*. Cambridge University Press, 2015.

[13] J. D. Griffiths. *Introduction to Quantum Mechanics*. Pearson Prentice Hall, 1995.

[14] M. L. Boas. *Mathematical Methods in the Physical Sciences*. Wiley, 3rd edition, 2006.

[15] K. Faezi. PhD thesis, University of Connecticut, 2020. Honors Scholar Theses, Paper 743.

# Chapter 2

# Single and Double Ionization Processes

## 2.1 Introduction

The study of ionization processes lies at the heart of atomic and molecular collision physics. When an energetic electron collides with an atom or molecule, the resulting removal of one or more electrons reveals fundamental aspects of electron correlation, many-body interactions, and the dynamical mechanisms governing the process.

In this chapter, we begin by discussing the concept of electron correlation in atomic and molecular systems, which plays a decisive role in determining the outcomes of both single and double ionization. To describe these correlations, various wavefunction–based methods are introduced, including the Hartree–Fock approximation (HFA) and configuration interaction (CI).

We then address the processes of single and double ionization by electron impact. Particular emphasis is placed on their description, the structural and dynamical information they reveal, and the importance of differential cross sections in interpreting both experimental and theoretical results. Different geometrical configurations, kinematical conditions, and incident energy regimes are also examined, along with the mechanisms underlying double ionization, such as shake-off and two-step processes.

Finally, we introduce two of the most important theoretical models that have proven especially effective in analyzing ionization phenomena: the BBK model and the Distorted Wave Born Approximation (DWBA). Together, these frameworks provide a solid foundation for understanding the complexity of ionization processes, for accurately interpreting experimental data, and for forming the basis of many other theoretical models.

## Atomic Units

In this chapter, we will use, as is customary, atomic units:

$$\hbar = e = m_e = a_0 = 1$$

with:

- $\hbar = \dfrac{h}{2\pi}$, where $h = 6.62 \times 10^{-34}$ J $\cdot$ s is Planck's constant.
- $e = -1.60 \times 10^{-19}$ C: the charge of an electron.
- $m_e = 9.11 \times 10^{-31}$ kg: the mass of an electron.
- $a_0 = 0.53 \times 10^{-10}$ m: the Bohr radius.

## 2.2 Electron Correlations in Atomic and Molecular Systems

Electron correlations are fundamental to understanding ionization processes and are essential for accurately describing the electronic structure and dynamics of atoms and molecules. The concept first emerged in the **1930s** with Wigner and Seitz [1], and a more formal definition for atomic systems was introduced by Löwdin in **1959** [2]. In atomic and molecular physics, electron correlation refers to the interdependent motion of electrons due to their mutual Coulomb repulsion. Any perturbation applied to one part of a system inevitably affects all others, making the accurate description of correlated electron behavior critical for both theoretical and experimental analysis [3].

The electron correlation energy is defined as the difference between the exact non-relativistic energy and the Hartree–Fock energy. This missing energy, although small in magnitude, plays a crucial role in accurately predicting chemical bonding, excitation spectra, and ionization probabilities.

Electron correlation can generally be classified into two types: structural and dynamical correlations. Structural correlation arises from the Coulomb interactions between bound-state electrons in atoms or molecules, as well as between continuum electrons. These interactions, typically expressed as $1/r_{ij}$ potentials, make it impossible to solve the Schrödinger equation exactly for systems with more than one electron. As a result, such systems can only be described approximately, and ongoing research continues to develop more accurate wave functions that account for this structural correlation.

On the other hand, dynamical correlation emerges during time-dependent processes such as ionization. During electron impact, for instance, the projectile perturbs the target, polarizing it and altering the wave function of the incoming electron; this is referred to as entrance-channel dynamical correlation. The Coulomb interaction between the outgoing electrons must also be included in the final-state description, leading to exit-channel dynamical correlation. These dynamical effects are typically incorporated using distorted-wave models or more advanced quantum scattering techniques.

Over recent decades, advanced electron correlation methods such as Configuration Interaction (CI), Coupled Cluster (CC), and related approaches have been developed, using Hartree–Fock theory as a reference. Combined with increased computational power, these methods enable highly accurate simulations of molecular structures, energies, and electron correlation effects in complex systems.

## 2.3 Wave–function Methods

We consider an $N$-electron system (atom or molecule) within the Born–Oppenheimer and non–relativistic approximations [4]. The Hamiltonian in the position representation is:

$$\hat{H} = \sum_{i=1}^{N} \hat{h}(\vec{r}_i) + \frac{1}{2} \sum_{i=1}^{N} \sum_{j \neq i}^{N} \frac{1}{|\vec{r}_i - \vec{r}_j|} \tag{2.1}$$

where $\hat{h}$ is the one-electron Hamiltonian, given by:

$$\hat{h}(\vec{r}_i) = -\frac{1}{2} \nabla^2_{\vec{r}_i} + v_{ne}(\vec{r}_i) \tag{2.2}$$

with $v_{ne}(\vec{r}_i) = -\sum_\beta \frac{Z_\beta}{|\vec{r}_i - \vec{R}_\beta|}$ representing the nucleus–electron interaction.

Stationary states satisfy the time-independent Schrödinger equation:

$$\hat{H}\, \Psi(x_1, x_2, \ldots, x_N) = E\, \Psi(x_1, x_2, \ldots, x_N) \tag{2.3}$$

where $\Psi(x_1, x_2, \ldots, x_N)$ is a wave function written in terms of the space-spin coordinates:

$$x_i = (\vec{r}_i, \omega_i), \quad \vec{r}_i \in \mathbb{R}^3,\ \omega_i \in \{\uparrow, \downarrow\}$$

and $E$ is the associated energy.

Because electrons are fermions, the wave function must be antisymmetric with respect

to the exchange of two space-spin coordinates:

$$\Psi(\ldots, x_i, \ldots, x_j, \ldots) = -\Psi(\ldots, x_j, \ldots, x_i, \ldots) \tag{2.4}$$

Using Dirac's bra–ket notation, we can write:

$$\hat{H}\,|\Psi\rangle = E\,|\Psi\rangle \tag{2.5}$$

The ground-state electronic energy $E_0$ can be expressed by the variational principle:

$$E_0 = \min_{\Psi} \langle\Psi|\hat{H}|\Psi\rangle \tag{2.6}$$

where the minimization is taken over all $N$-electron antisymmetric wave functions $\Psi$ normalized to unity:

$$\langle\Psi|\Psi\rangle = 1 \tag{2.7}$$

Properties such as dipole moments or optical spectra can be obtained as derivatives of the ground-state energy with respect to an external perturbation. Among the main strategies for electronic-structure calculations, wave-function methods play a central role. In this context, we focus on two key approaches: the Hartree–Fock (HF) method [5], which provides the mean-field approximation and serves as the reference for most correlated methods, and the Configuration Interaction (CI) method [5], which systematically incorporates electron correlation by considering excitations beyond the Hartree–Fock determinant.

### 2.3.1 Atomic and Molecular Orbitals

Atomic orbitals (AOs) form the basic building blocks for constructing electronic wavefunctions in atoms and molecules. For hydrogen, exact solutions of the Schrödinger equation are possible, with orbitals expressed as a product of a radial function $R_{nl}(r)$ and a spherical harmonic $Y_{lm}(\theta, \phi)$:

$$\Psi_{nlm}(r, \theta, \phi) = R_{nl}(r)Y_{lm}(\theta, \phi), \tag{2.8}$$

with energies $E_n = -\frac{13.6}{n^2}\ eV$. For hydrogen-like atoms with nuclear charge $+Ze$, the radial function depends explicitly on $Z$.

For multi–electron atoms, approximate solutions are often constructed from hydrogenic orbitals [6].

These atomic orbitals can be represented using Slater–type or Gaussian-type functions [7, 8], or alternatively by an orthogonal Laguerre basis, depending on the require-

ments of the calculation:

$$\phi_{AO}(\vec{r}) = \sum_{j=1}^{N_i} a_{ij}\, \varphi_j(\vec{r}) \tag{2.9}$$

where $k$ is a characteristic parameter of the atomic orbital, and $N_i$ denotes the number of atomic orbitals included in the expansion. The coefficients $a_{ij}$ specify the contribution of each atomic orbital and are determined using the variational method. The functions $\varphi_j(\vec{r})$ are expressed in terms of a basis of spherical harmonics $Y_{lm}(\theta, \varphi)$.

Molecular orbitals (MOs) are then constructed as linear combinations of atomic orbitals (LCAO-MO) [8]:

$$\psi_i = \sum_{k=1}^{M} C_{ik}\phi_k \tag{2.10}$$

where $\phi_k$ are atomic orbitals and $C_{ik}$ are the coefficients defining their contribution to the molecular orbital. Two conditions must be met for combination: similar orbital energies and compatibl symmetries for nonzero overlap [9].

Molecular orbitals constitute the foundation for Hartree–Fock and Configuration Interaction calculations, as well as for a wide range of other theoretical methods in quantum chemistry and atomic collision theory.

**Molecular Orbital for Water molecule ($H_2O$)**

The $H_2O$ molecule has five occupied molecular orbitals, labeled $1a_1$, $2a_1$, $1b_2$, $3a_1$, and $1b_1$ (HOMO). Using the LCAO-MO method, these MOs are constructed from linear

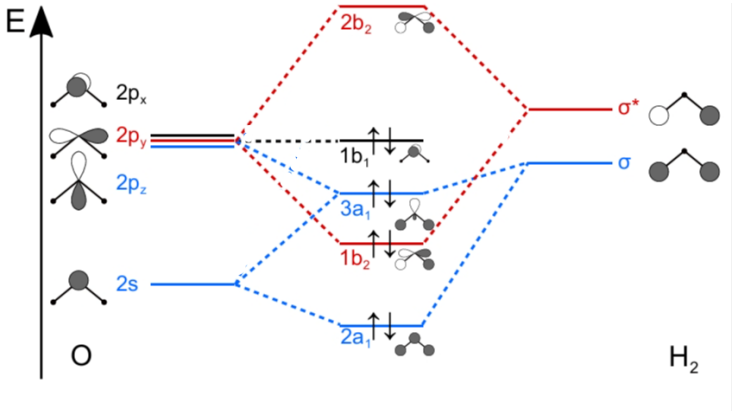


**Figure 2.1:** Energy diagram of $H_2O$ molecular orbitals.

combinations of the 1s orbitals of hydrogen and the 2s and 2p orbitals of oxygen [10]. The

ground-state electronic configuration of $H_2O$ can be represented as:

$$(1a_1)^2(2a_1)^2(1b_2)^2(3a_1)^2(1b_1)^2$$

### 2.3.2 The Hartree Fock (HF) method

The Hartree–Fock (HF) method approximates the ground-state wave function $\Psi_0$ of an $N$-electron system by a single antisymmetrized product of $N$ spin orbitals $\{\chi_i(x)\}$, denoted by $\Phi_0$:

$$\Phi_0(x_1, x_2, \ldots, x_N) = \mathcal{A}\left[\chi_1(x_1)\chi_2(x_2)\cdots\chi_N(x_N)\right] \tag{2.11}$$

where the antisymmetrizer operator $\mathcal{A}$ is defined as

$$\mathcal{A} = \frac{1}{\sqrt{N!}}\sum_{n=1}^{N!}(-1)^{p_n}P_n \tag{2.12}$$

with the sum running over the $N!$ permutations $P_n$ of the space–spin coordinates $\{x_1, .., x_N\}$, and where $p_n$ is the number of pair inversions associated with the permutation $P_n$.

A central feature of the HF formalism is that the wave function $\Phi_0(x_1, x_2, \ldots, x_N)$ can be conveniently expressed as a Slater determinant:

$$\Phi_0(x_1, x_2, \ldots, x_N) = \frac{1}{\sqrt{N!}}\begin{vmatrix} \chi_1(x_1) & \chi_2(x_1) & \cdots & \chi_N(x_1) \\ \chi_1(x_2) & \chi_2(x_2) & \cdots & \chi_N(x_2) \\ \vdots & \vdots & \ddots & \vdots \\ \chi_1(x_N) & \chi_2(x_N) & \cdots & \chi_N(x_N) \end{vmatrix} \tag{2.13}$$

For brevity, one often adopts shorthand notation such as:

$$|\Phi_0\rangle \equiv |\chi_1\chi_2\cdots\chi_N\rangle \tag{2.14}$$

Each spin orbital $\chi_i(x)$ is typically written as the product of a spatial orbital $\psi_i(\vec{r})$ and a spin function $\alpha(\omega)$ or $\beta(\omega)$:

$$\chi_i(x) = \psi_i(\vec{r})\alpha(\omega) \quad \text{or} \quad \chi_i(x) = \psi_i(\vec{r})\beta(\omega),$$

with

$$\alpha(\uparrow) = 1, \quad \alpha(\downarrow) = 0, \quad \beta(\uparrow) = 0, \quad \beta(\downarrow) = 1.$$

The spin orbitals are assumed to be orthonormal:

$$\langle \chi_i | \chi_j \rangle = \int \chi_i^*(x) \chi_j(x)\, dx = \delta_{ij} \tag{2.15}$$

The Hartree–Fock electronic energy is expressed in terms of integrals over the spin orbitals (using Slater's rules [11] for evaluating expectation values over Slater determinants):

$$E_{\mathrm{HF}}[\{\chi_i\}] = \langle \Phi_0 | \hat{H} | \Phi_0 \rangle \tag{2.16}$$

The exact ground–state energy $E_0$ is always lower than $E_{\mathrm{HF}}$, and their difference $E_c = E_0 - E_{\mathrm{HF}}$ is known as the correlation energy (see Section 2.2).

The Hartree-Fock method is therefore a mean-field approximation: instead of describing the instantaneous electron–electron repulsion exactly, it treats each electron as moving independently in the average field generated by all other electrons. This interpretation leads to a set of self-consistent equations, solved iteratively until both the orbitals and their associated energies converge [4].

Although this approach captures the average effects of electron–electron interactions (typically around 99%), it neglects dynamic correlation effects beyond the mean-field picture.

### 2.3.3 Configuration Interaction (CI) Method

The Configuration Interaction (CI) method is a post-Hartree–Fock approach designed to recover electron correlation. Whereas Hartree–Fock represents the ground state by a single Slater determinant, CI expands the wavefunction as a linear combination of several determinants constructed from excitations out of the HF reference state. It is typically written as:

$$|\Psi\rangle = c_0 |\Phi_0\rangle + \sum_{r,a} c_a^r |\Phi_a^r\rangle + \sum_{a<b,\, r<s} c_{ab}^{rs} |\Phi_{ab}^{rs}\rangle + \sum_{a<b<c,\, r<s<t} c_{abc}^{rst} |\Phi_{abc}^{rst}\rangle + \cdots \tag{2.17}$$

Here, the coefficients $c_0, c_a^r, c_{ab}^{rs}, \ldots$ are variational parameters determined in the configuration interaction procedure. $|\Phi_0\rangle$ is the so-called *reference determinant*, typically obtained from a Hartree–Fock self-consistent-field (SCF) calculation. The determinant $|\Phi_a^r\rangle$ denotes a singly excited determinant obtained by substituting the occupied spin-orbital $a$ in the reference determinant $|\Phi_0\rangle$ with an unoccupied (virtual) spin-orbital $r$, and similarly for higher excitations. The indices $a, b, c$ label occupied orbitals in the reference configuration, whereas $r, s, t$ denote virtual orbitals.

In this way, the CI wavefunction captures correlations between electrons that are neglected in the mean-field picture of Hartree–Fock. Depending on the level of excitation included—singles (CIS), doubles (CID), or higher—the method provides increasingly accurate results. In practice, the most common truncation is Configuration Interaction with Singles and Doubles (CISD), where only single and double excitations are considered relative to the reference state. For many small molecules near equilibrium geometries, CISD recovers a large fraction (often around 95%) of the total correlation energy [5, 12].

In principle, a full CI calculation that includes all possible excitations within a given basis set provides the exact solution of the nonrelativistic Schrödinger equation for that basis. However, since the computational cost of full CI increases factorially with system size, its use is limited to small systems.

### 2.3.4 Frozen Core Approximation

In many correlated electronic-structure methods (such as Configuration Interaction (CI), many-body perturbation theory, or Coupled-Cluster theory (CC)) it is standard practice to employ the so-called frozen core approximation. In this approach, the innermost molecular orbitals, which are occupied by tightly bound core electrons, are kept fixed as doubly occupied in all configurations and are not allowed to participate in ionization.

For example, in atoms ranging from lithium to neon, the $1s$ orbital is usually considered part of the frozen core. For heavier atoms, such as those between sodium and argon, the core typically includes the $1s$, $2s$, and $2p$ orbitals. When applied to molecules, the frozen orbitals mainly correspond to combinations formed from these inner atomic shells.

This approximation is justified because core electrons are much less affected by the surrounding chemical environment than valence electrons. As a result, neglecting their correlation introduces an error that remains nearly constant across molecules containing the same atomic species. Moreover, most commonly used basis sets in quantum chemistry are not sufficiently flexible in the core region to capture electron correlation accurately. For this reason, freezing the core is not only computationally convenient but often more reliable than attempting to correlate all electrons [13].

**Limitations:** While the frozen core approximation works well for ground-state properties dominated by valence electrons, it can be inadequate for processes that involve core electrons, such as core ionization, X-ray spectroscopy, or highly excited electronic states. In such cases, explicit correlation of the core orbitals may be necessary to achieve accurate results [14].

## 2.4 The Process of Single Ionization

### 2.4.1 Description of the (e,2e) Process

Single ionization (SI) is a process in which one electron is removed from an atom or molecule due to a collision with another particle, forming a positively charged ion. **The** $(e, 2e)$ **reaction** is a specific **complete** electron-scattering experiment in which a monoenergetic incident electron, possessing an initial momentum $\vec{k}_i$ relative to the center of mass of the target and energy $E_i$, collides with an atom or molecule in its ground state $|\phi_a\rangle$. During this interaction, one electron is ejected from the target (typically from the valence shell), emerging with momentum $\vec{k}_1$ and energy $E_1$, while the target becomes a positively charged ion $X^+$ with recoil momentum $\vec{q}$ and recoil energy $E_{\text{rec}}$. **Simultaneously**, the incident electron is scattered, emerging with a new momentum $\vec{k}_s$ and energy $E_s$ ( the two outgoing electrons are measured in **coincidence**).

The two electrons in the final state are fundamentally indistinguishable in quantum mechanics; however, it is common in experimental analysis to distinguish them by energy: the electron with higher energy is referred to as the scattered electron, and the less energetic one as the ejected electron. The process can be represented schematically as:

$$e^-(E_i, \vec{k}_i) + X \longrightarrow X^+(E_{\text{rec}}, \vec{q}) + e^-(E_1, \vec{k}_1) + e^-(E_s, \vec{k}_s)$$

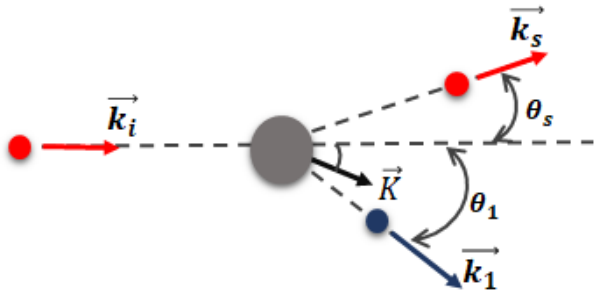


**Figure 2.2:** Diagram of an (e,2e) reaction in coplanar geometry.

This three-body process obeys the conservation of energy and momentum:

$$E_{\text{initial}} = E_{\text{final}} \quad \Longleftrightarrow \quad E_i = E_s + E_1 + IP^+ + E_{\text{rec}} \tag{2.18}$$

$$\vec{k}_i = \vec{k}_s + \vec{k}_1 + \vec{q} \tag{2.19}$$

Here, $IP^+ = E_{X^+} - E_X$ is the single-ionization potential of the target, where $E_X$ is the ground-state energy of the neutral target and $E_{X^+}$ is the ground-state binding en-

ergy of the singly charged ion. The recoil energy $E_{\text{rec}}$ is usually neglected in the energy balance because it is very small compared to the kinetic energies of the electrons.

The momentum transfer is defined as:

$$\vec{K} = \vec{k}_i - \vec{k}_s \tag{2.20}$$

The magnitude of the momentum transfer determines the collision regime and, consequently, the type of information that can be extracted. For low to moderate values ($K < 1$–$2$ a.u.), the measurements primarily probe the collision dynamics. For larger values ($K > 2$–$3$ a.u.), the results are more sensitive to the intrinsic structure of the target [3].

### 2.4.2 Structural and Dynamical Studies

The direction of the momentum transfer plays a key role in distinguishing between structural studies by electron impact (referred to Electron Momentum Spectroscopy (EMS)) and studies of collision dynamics.

- **Structural Studies:**

Structural studies in single ionization are primarily concerned with probing intrinsic electronic properties of the target, such as the ionization potentials of specific orbitals, the spatial and momentum distributions of electrons, and the underlying electron–electron correlations in the bound state. These investigations aim to minimize the complexity of the ionization process, reducing it ideally to a binary electron–electron collision. In such a regime, the incident electron acts merely as a probe, transferring energy and momentum to a bound electron without significantly perturbing the residual ion.

To ensure dominance of the binary interaction and the suppression of many-body effects, kinematic parameters are chosen to yield relatively large momentum transfers (typically in the range of 4 to 7 atomic units) and to satisfy the Bethe condition. This condition ensures that nearly all the energy and momentum transferred from the projectile is absorbed by the ejected electron, while the residual ion remains a passive spectator. In this category, symmetric coplanar geometries [15] and non-coplanar geometries [16] are the most suitable and are performed at high impact energies (1–2 keV), with the two continuum electrons having equal energies (see section 2.4.3.2). In such conditions, the reaction mechanism can be accurately described within first-order theories [17], and the measured cross sections become directly proportional to the square of the wave function in momentum space [17].

One of the most direct methods used in this context is Electron Momentum Spectroscopy (EMS) [8, 18], which provides access to the momentum space wavefunctions of the target's valence electrons and use electron–electron coincidence technique. In EMS, high incident energies and specific geometrical configurations are employed (such as the symmetric non-coplanar geometry) to satisfy conditions that simplify the reaction mechanism. Under these conditions, the Plane Wave Impulse Approximation (PWIA) [19] becomes valid, and the observed triple differential cross section (TDCS) is directly proportional to the spherically averaged momentum distribution of the Dyson orbital [8]:

$$\sigma = A \int |\langle \vec{p}\, \psi_{N-1} \mid \psi_N \rangle|^2 \, \mathrm{d}\Omega \tag{2.21}$$

where $|\vec{p}\rangle$ is a plane wave of momentum $\vec{p}$. $\psi_N$ and $\psi_{N-1}$ are, respectively, the many-electron wavefunction of the $N$ electron initial state and the wavefunction of the $(N-1)$ electron final state describing the residual ion. The term $A$ is a kinematic factor which is essentially constant.

These structural measurements serve not only as experimental benchmarks for quantum chemical calculations, but also as a means to evaluate the extent of electronic correlation captured by the wavefunction models.

- **Dynamical Studies:**

In contrast to structural investigations, dynamical studies focus on the time-dependent aspects of the ionization process, particularly the interactions that occur during and after the collision between the incident electron and the target. These studies aim to understand the detailed mechanisms by which energy and momentum are transferred within the system, including the polarization of the target, excitation of residual ions, and interactions among continuum electrons.

Dynamical correlation effects are typically divided into two classes: entrance-channel and exit-channel interactions. In the entrance channel, the incident electron may distort the electronic cloud of the target even before ionization occurs. This dynamic polarization alters the effective potential landscape and modifies the scattering wavefunction. In the exit channel, additional correlations emerge between the ejected and scattered electrons, particularly due to their mutual Coulomb repulsion. This post-collision interaction (PCI) plays a crucial role in shaping the angular and energy distributions observed in the final state.

To accurately describe these effects, more sophisticated theoretical models must be used beyond the independent-particle picture. These include the Distorted Wave Born

Approximation (DWBA) [20], Three-Coulomb-Wave (BBk) [21] models, and their improved versions such as the Modified 3CW model [22], and 3CWZ model [23], which incorporate Coulomb distortions and PCI explicitly. These models allow for the construction of more realistic final-state wavefunctions, which are essential for reproducing experimental Fully differential cross sections at low and intermediate energies.

Unlike structural studies, where the residual ion is treated as a passive spectator, dynamical studies recognize its potential influence on the scattering dynamics. This includes recoil effects, target excitation, and long-range polarization fields. Therefore, the kinematic conditions are chosen to be more flexible or asymmetric in order to enhance sensitivity to these dynamical features.

### 2.4.3 Geometries and Kinematics of the (e,2e) process

The kinematics of an $(e, 2e)$ reaction are defined by the energies of the incident and outgoing electrons, as well as the momentum transfer $\vec{K}$. The kinematics used to measure the singly differential or fully differential cross sections are commonly classified into distinct categories based on geometry: coplanar or non-coplanar, and symmetric or asymmetric configurations (see table 2.1). Each of these configurations serves a specific purpose in the study of ionization mechanisms and offers unique insights into collision dynamics.

A configuration is said to be in coplanar geometry when the scattered and ejected electrons are detected within the same plane as the incident electron beam, typically referred to as the plane of incidence (plane of collision). In contrast, a non-coplanar geometry arises when at least one of the outgoing electrons lies outside this plane. In general, the three momentum vectors involved in the reaction (the incident electron $\vec{k}_i$, the scattered electron $\vec{k}_s$, and the ejected electron $\vec{k}_1$) do not lie in the same plane, except in cases where the azimuthal angle between the two outgoing electrons, defined as $\phi = \phi_1 - \phi_s$, takes values of 0 or $\pi$.

#### 2.4.3.1 Asymmetric geometry

In the **asymmetric coplanar geometry**, the two outgoing electrons are detected in different directions and with significantly different energies. The scattering angle $\theta_s$ is fixed to a small value, typically between 0° and 12°, and generally less than 20° ($\phi_s = 0$ or $\pi$), in order to achieve high experimental resolution. Concurrently, the ejection angle $\theta_1$ is allowed to vary and is measured using a movable detector within the plane. This geometry is particularly effective for exploring the dipole regime of ionization dynamics, which is characterized by small momentum transfer. Experiments employing this configuration span a wide range of incident electron energies, from low to intermediate and high, and have

been extensively used in benchmark studies, such as those conducted by the group of Lahmam-Bennani and by Ehrhardt's team [24]. The asymmetric geometry allows for a clear separation of collision mechanisms and provides valuable insight into the angular and energy correlations in the ionized system.

Conversely, **asymmetric non coplanar** geometry is particularly valuable because it enhances the sensitivity of the measured triple differential cross section (TDCS) to electron-electron correlation and quantum interference effects. The spatial separation of the scattering planes allows for clearer observation of interference patterns arising from different quantum-mechanical pathways, which often manifest as pronounced minima or modulations in the TDCS. Moreover, the asymmetric energy sharing leads to a more complex post-collision interaction between the scattered and ejected electrons, providing a stringent test for theoretical models. As such, asymmetric non-coplanar geometry serves as a powerful diagnostic tool for probing the underlying dynamics of electron-impact ionization and exploring correlation-driven processes that remain hidden in simpler geometrical configurations.

#### 2.4.3.2 Symmetric geometry

In this geometry, the scattered and ejected electrons are detected with equal angles $\theta_s = \theta_1 = \theta$ and equal energies $E_s = E_1 = \dfrac{E_i - E_{\text{ion}}}{2}$. This geometry allows for the study of the target structure.

In the **symmetric coplanar** geometry, the two outgoing electrons are emitted within the same plane. This geometry was first introduced by Amaldi *et al.* [25]. Under these kinematic conditions, the magnitude of the recoil momentum $\vec{q}$ can be expressed as

$$q = k_i - 2k_1 \cos\theta \tag{2.22}$$

The magnitude of $\vec{q}$ remains small for scattering angles $\theta < 60°$ and reaches a minimum near $\theta = 45°$. For $\theta > 90°$, however, $q$ increases significantly, indicating that the collision is driven by large momentum transfers $\vec{K}$ [26]. The TDCS is measured as a function of the angle $\theta$. In this case, the exchange factor between the electrons must be taken into account, as it is crucial for accurately describing the reaction mechanism.

In the **symmetric non coplanar** configuration, the two outgoing electrons are emitted in different planes, with distinct non-zero azimuthal angles $\phi_s$ and $\phi_1$. This geometry is particularly suitable for probing electron momentum densities (Electron Momentum Spectroscopy; see Section 2.4.2). The TDCS can be measured either as a function of the

angle $\Phi$ or as a function of the recoil momentum of the target, which is expressed as:

$$q = \left[ (2k_s \cos\theta - k_i)^2 + 4k_s^2 \sin^2\theta \, \sin^2\left(\frac{\Phi}{2}\right) \right]^{1/2} \tag{2.23}$$

where $\Phi = \pi - |\phi_s - \phi_1|$, and $\phi_s - \phi_1$ representing the relative azimuthal angle between the two continuum electrons.

**Tableau 2.1:** Classification of possible geometries for the $(e, 2e)$ processes.

| **Geometry** | **Coplanar** $\vec{k}_1$ and $\vec{k}_s$ in the collision plane | **Non Coplanar** $\vec{k}_1$ and $\vec{k}_s$ lie outside the collision plane |
|---|---|---|
| **Symmetric** $E_1 = E_s$, $\theta_1 = \theta_s$ | 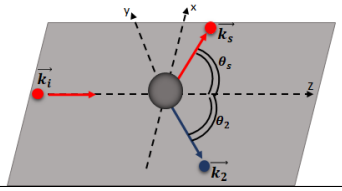 | 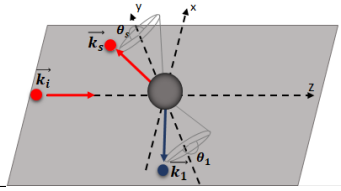 |
| **Asymmetric** $E_1 \neq E_2$, $\theta_1 \neq \theta_s$ | 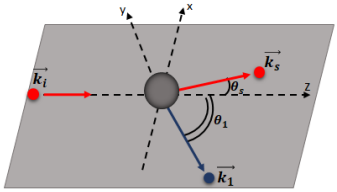 | 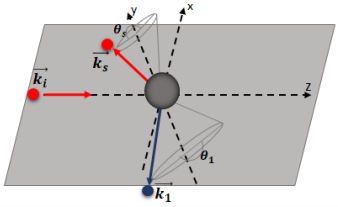 |

## 2.4.4 Differential Cross Sections for (e,2e) process

The results obtained in an $(e, 2e)$ experiment are typically expressed in terms of differential cross sections. While Chapter 1 introduced the general concept of differential cross sections, this chapter focuses on their application in the context of single and double ionization ionization. A subsequent section will address differential cross sections in the case of double ionization.

### 2.4.4.1 Triply Differential Cross Section (TDCS)

The Triply Differential Cross Section (TDCS) provides the most detailed description of the kinematics of single ionization. It corresponds to the coincident detection of both outgoing electrons, namely, the scattered and the ejected. These electrons are characterized by their respective energies $E_s$, $E_1$, and momenta $\vec{k}_s$, $\vec{k}_1$, as they emerge into the solid angles $d\Omega_s = \sin\theta_s \, d\theta_s \, d\phi_s$ and $d\Omega_1 = \sin\theta_1 \, d\theta_1 \, d\phi_1$ after a single ionization induced by an incident electron of energy $E_i$.

The TDCS is mathematically expressed as:

$$\sigma^{(3)} = \frac{d^3\sigma}{d\Omega_s\, d\Omega_1\, dE_1} = \frac{k_s\, k_1}{k_i}\, |T_{fi}|^2 \tag{2.24}$$

where $T_{fi}$ is the transition matrix element between the initial and final states.

We consider single active electron (SAE) approximation [13]. In the second Born approximation, the TDCS (Eq. 2.24) can be written as:

$$\sigma^{(3)} = \frac{d^3\sigma}{d\Omega_s d\Omega_1 dE_1} = \frac{k_s k_1}{k_i}\, |f_{B1} + f_{B2}|^2 \tag{2.25}$$

where first Born term $f_{B1}$ is expressed as:

$$f_{B1} = -\frac{1}{2\pi} \left\langle e^{i\vec{k_s}\cdot\vec{r_0}} \Psi^-(\vec{k_1}, \vec{r_1})\, |V|\, e^{i\vec{k_i}\cdot\vec{r_0}} \Phi_i(\vec{r_1}) \right\rangle \tag{2.26}$$

and the second Born term $f_{B2}$:

$$f_{B2} = \frac{1}{8\pi^4} \sum_n \int \frac{d\vec{q}}{q^2 - k_n^2 - i\varepsilon} \left\langle e^{i\vec{k}_s\cdot\vec{r}_0} \Psi^-(\vec{k}_1, \vec{r}_1)\, |V|\, e^{i\vec{q}\cdot\vec{r}_0} \Phi_n(\vec{r}_1) \right\rangle \left\langle e^{i\vec{q}\cdot\vec{r}_0} \Phi_n(\vec{r}_1)\, |V|\, e^{i\vec{k}_i\cdot\vec{r}_0} \Phi_i(\vec{r}_1) \right\rangle \tag{2.27}$$

where $\Phi_i(\vec{r_1})$ is the exact wave function of the initial state of the target and $\Psi^-(\vec{k_1}, \vec{r_1})$ is the exact wave function for the continuum state of the target.

The potential $V$ represents the Coulomb interaction between the incoming electron and the target and is written as:

$$V = \frac{1}{r_{01}} - \frac{1}{r_0} \tag{2.28}$$

For $f_{B2}$, $\varepsilon \to 0^+$ with $\frac{k_n^2}{2} = \frac{k_i^2}{2} - (E_n - E_i)$.

We neglect the exchange effects by considering the scattered electron as the fast electron and the ejected electron as the slow electron. It should be noted that if we do not employ the single active electron (SAE) approximation, we must take into account all the electrons of the target in the calculation (a multi-electron treatment) [27].

#### 2.4.4.2 Doubly Differential Cross Section (DDCS)

If both the emission angle and energy of one detected electron can be measured, the cross section is referred to as the Doubly Differential Cross Section (DDCS). Compared to the Singly Differential Cross Section, the DDCS provides more specific information about the angular and energy distributions of the scattered or ejected electrons following ionization.

The DDCS is obtained by integrating the TDCS over the solid angle of the unde-

tected electron. If the interest lies in the scattered electron:

$$\frac{d^2\sigma}{d\Omega_s\, dE_1} = \int d\Omega_1 \frac{d^3\sigma}{d\Omega_s\, d\Omega_1\, dE_1} \tag{2.29}$$

And if the focus is on the ejected electron:

$$\frac{d^2\sigma}{d\Omega_1\, dE_1} = \int d\Omega_s \frac{d^3\sigma}{d\Omega_s\, d\Omega_1\, dE_1} \tag{2.30}$$

#### 2.4.4.3 Singly Differential Cross Section (SDCS)

When only one of the outgoing electrons is selectively detected (typically at a fixed angle or with fixed energy), the measured quantity is the Singly Differential Cross Section (SDCS). This can be angular:

$$\frac{d\sigma}{d\Omega} = \int dE \frac{d^2\sigma}{d\Omega\, dE} \tag{2.31}$$

or energy-resolved:

$$\frac{d\sigma}{dE} = \int d\Omega \frac{d^2\sigma}{d\Omega\, dE} \tag{2.32}$$

The angular SDCS, $d\sigma/d\Omega$, provides directional information about the scattered or ejected electron and is useful in structural investigations of atomic and molecular targets.

On the other hand, the energy-resolved SDCS, $d\sigma/dE$, depends on the energies of the incident and ejected electrons and represents the energy distribution of the detected electron integrated over all emission angles. This quantity plays a significant role in many fields, such as atmospheric physics, especially in studies related to electron energy loss in the Earth's ionosphere.

## 2.5 The Process of Double Ionization

### 2.5.1 Description of the (e,3e) process

the kinematically **complete** double ionization experiments process is commonly called (e,3e) reaction by analogie with the (e,2e) process described in Section 2.4.1. It involves the ejection of two bound electrons from the target by an incident monoenergetic electron of momentum $\vec{k}_i$ and energy $E_i$. The final state consists of the scattered projectile with momentum $\vec{k}_s$ and energy $E_s$, two ejected electrons with momenta $\vec{k}_1$ and $\vec{k}_2$ (energies $E_1$ and $E_2$), and the residual ion $X^{2+}$ carrying a momentum $\vec{q}$ and energy $E_{\text{rec}}$ (Figure 2.3).

The reaction can be schematically expressed as:

$$e^-(E_i, \vec{k}_i) + X \longrightarrow X^{2+}(E_{\text{rec}}, \vec{q}) + e^-(E_1, \vec{k}_1) + e^-(E_2, \vec{k}_2) + e^-(E_s, \vec{k}_s)$$

These experiments are particularly challenging to perform due to the extremely small cross section associated with double ionization (DI), as well as the requirement of detecting a **triple coincidence signal** involving the three electrons in the final state. To circumvent these difficulties, a less demanding experimental approach is often employed, referred to as the $(e, 3e-1)$ configuration, in which only two out of the three electrons are detected in coincidence. The conservation of energy and momentum for the system, involv-

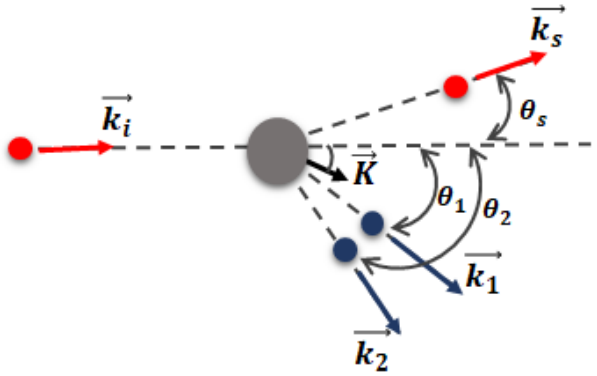


**Figure 2.3:** Diagram of an (e,3e) reaction in coplanar geometry.

ing all three final-state electrons is:

$$E_{\text{initial}} = E_{\text{final}} \quad \Longleftrightarrow \quad E_i = E_s + E_1 + E_2 + IP^{++} + E_{\text{rec}} \tag{2.33}$$

$$\vec{k}_i = \vec{k}_s + \vec{k}_1 + \vec{k}_2 + \vec{q} \tag{2.34}$$

Here, $E_{\text{initial}}$ and $E_{\text{final}}$ are the total initial and final state energies of the (projectile-target) system. $IP^{++} = E_{X^{2+}} - E_X$ is the double ionization energy of the target, where $E_X$ is the energy of the ground state of the target $X$ and $E_{X^{2+}}$ is the energy of an arbitrary state of the doubly ionized residual ion $X^{2+}$. As in the single ionization case, $E_{\text{rec}}$ is neglected in the energy balance.

The momentum transfer, defined by $\vec{K} = \vec{k}_i - \vec{k}_s$, is a ke parameter in determining the collision regime and the type of information accessible: small $K$ values probe the collision dynamics, whereas large $K$ values provide insight into the target structure [28].

### 2.5.2 Geometries and kinematics of the $(e, 3e)$ process

The geometries of the $(e, 3e)$ process are similar to those of the $(e, 2e)$ process, with some differences, which are summarized in Table 2.2. Note that plane of collision is defined by the two vectors $\vec{k}_i$ and $\vec{k}_s$.

**Tableau 2.2:** Classification of possible geometries for the $(e, 3e)$ processes.

| **Geometry** | **Coplanar**<br>$\vec{k}_1$ and $\vec{k}_2$ in the collision plane,<br>$\varphi = \lvert\varphi_1 - \varphi_2\rvert = 0\ or\ \pi$ | **Non Coplanar**<br>$\vec{k}_1$ and $\vec{k}_2$ lie outside the collision plane,<br>$\Phi = \lvert\varphi_1 - \varphi_2 - \pi\rvert$ |
|---|---|---|
| **Symmetric**<br>$E_1 = E_2$,<br>$\theta_1 = 2\pi - \theta_2$ | 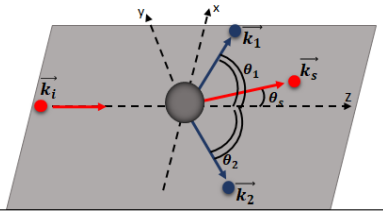 | 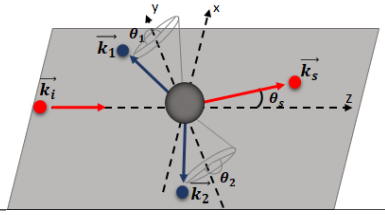 |
| **Asymmetric**<br>$E_1 \neq E_2$,<br>$\theta_1 \neq \theta_2$ | 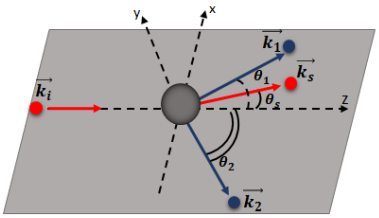 | 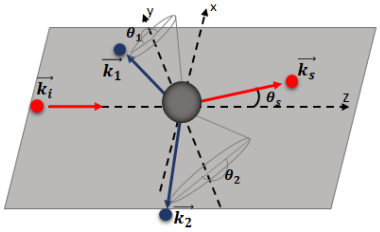 |

### 2.5.3 Differential Cross Section for (e,3e) process

The determination of the scattering cross section in the case of a double ionization collision can be obtained by considering the transition rate from an initially state to a specific final state. This final state is characterized by a density of states written as $d^3k_1\, d^3k_2\, d^3k_s$. The ratio between this transition rate and the incident flux density gives the corresponding cross section (see chapter 1). It can be expressed as:

$$d\sigma(k_s, k_1, k_2; k_i, \psi_i) = \frac{(2\pi)^4}{k_i}\, \delta(E_f - E_i)\ |T_{fi}|^2\ d^3k_1\, d^3k_2\, d^3k_s \tag{2.35}$$

where $T_{fi} = \langle\psi_f|V|\psi_i\rangle$ is the transition matrix element from the initial state to the final state.

#### 2.5.3.1 Five-fold Differential Cross Section (FDCS)

In double ionization (DI) experiments, the final state involves three electrons, which in principle requires nine kinematic parameters to fully describe their motion. By re-

stricting the measurement to a coplanar geometry and applying energy conservation, this number reduces to five independent parameters. When these five parameters are fully determined, the experiment is considered 'complete,' and the corresponding differential cross section is referred to as the fivefold differential cross section (FDCS):

$$\sigma^5 = \frac{d^5\sigma}{dE_1\, dE_2\, d\Omega_1\, d\Omega_2\, d\Omega_s} = \frac{k_1 k_2 k_s}{k_i}\, |T_{fi}|^2 \tag{2.36}$$

where $d\Omega_s$, $d\Omega_1$, and $d\Omega_2$ are the solid-angle elements of the scattered and the two ejected electrons, while $E_1$ and $E_2$ denote the energies of the ejected electrons.

If we consider the case where the projectile electron has a relatively high velocity, it can be conveniently described by a plane wave, wich Allows to use the first Born approximation (FBA) [29]. By considering low momentum transfer and employing the frozen-core approximation, the many-electron target problem can be reduced to a two-active-electron model [13], where only the electrons that will be ionized are explicitly considered. In some cases, the FBA is not sufficient, and it becomes necessary to include the Second Born Approximation(SBA) [27].

The five-fold differential cross section (FDCS) for a two electron system (helium-likes) can be expressed as:

$$\frac{d^5\sigma}{d\Omega_s\, d\Omega_1\, d\Omega_2\, dE_1\, dE_2} = \frac{k_s k_1 k_2}{k_i}\, |f_{B1} + f_{B2}|^2 \tag{2.37}$$

where

$$f_{B1} = -\frac{1}{2\pi} \left\langle \Psi^-(\vec{k}_1, \vec{k}_2; \vec{r}_1, \vec{r}_2)\, e^{i\vec{k}_s\cdot\vec{r}_0} \middle| V \middle| e^{i\vec{k}_i\cdot\vec{r}_0}\, \Phi_i(\vec{r}_1, \vec{r}_2) \right\rangle, \tag{2.38}$$

and

$$f_{B2} = \frac{1}{8\pi^4} \sum_n \int \frac{d\vec{q}}{(q^2 - k_n^2 - i\varepsilon)} \left\langle \psi^- \left(\vec{k}_1, \vec{k}_2; \vec{r}_1, \vec{r}_2\right) e^{i\vec{k}_s\cdot\vec{r}_0}\, |V|\, \Phi_n\left(\vec{r}_1, \vec{r}_2\right) e^{i\vec{q}\cdot\vec{r}_0} \right\rangle \times \left\langle \Phi_n\left(\vec{r}_1, \vec{r}_2\right) e^{i\vec{q}\cdot\vec{r}_0}\, |V|\, e^{i\vec{k}_i\cdot\vec{r}_0} \Phi_i(\vec{r}_1, \vec{r}_2) \right\rangle \tag{2.39}$$

The interaction potential $V$ is given by:

$$V = -\frac{2}{r_0} + \frac{1}{r_{01}} + \frac{1}{r_{02}} \tag{2.40}$$

Here, $\Phi_i(\vec{r}_1, \vec{r}_2)$ denotes the initial-state wavefunction of the target, while $\Psi^-(\vec{k}_1, \vec{k}_2; \vec{r}_1, \vec{r}_2)$ represents the final-state wavefunction of the two ejected electrons. The coordinate $\vec{r}_0$ corresponds to the position of the incident electron.

The summation over $n$ incorporates the full contribution from all n discrete and con-

tinuum states of the ionized target (which contains the two active electrons) [30].

#### 2.5.3.2 Four-fold Differential Cross Section (4DCS)

The four-fold differential cross section (4DCS) is obtained by integrating the five-fold differential cross section (FDCS) over the solid angle of one of the outgoing electrons (either the scattered electron or one of the two ejected electrons). This quantity is measured in an $(e, 3e-1)$ experiment:

$$\sigma^4 = \frac{d^4\sigma}{dE_1\, dE_2\, d\Omega_s\, d\Omega_1} = \int \left( \frac{d^5\sigma}{dE_1\, dE_2\, d\Omega_1\, d\Omega_2\, d\Omega_s} \right) d\Omega_2 \tag{2.41}$$

Or

$$\sigma^4 = \frac{d^4\sigma}{dE_1\, dE_2\, d\Omega_1\, d\Omega_2} = \int \left( \frac{d^5\sigma}{dE_1\, dE_2\, d\Omega_1\, d\Omega_2\, d\Omega_s} \right) d\Omega_s \tag{2.42}$$

Since one electron is not fully characterized, the 4DCS is considered an incomplete measurement. It describes instead the angular correlation between two selected electrons among the three emitted in the double ionization process [3].

### 2.5.4 The Mechanisms of Double Ionization

Over the past two decades, both theory and experiment have significantly advanced our understanding of the four-body problem involved in double ionization (DI).

A complete characterization of such a four-body system can be achieved experimentally by simultaneously measuring the momentum vectors of all final-state particles. This type of multi-coincidence measurement [31], while extremely powerful, suffers from intrinsically low counting rates, making its realization technically challenging. Recent developments in multi-detection techniques have greatly improved these measurements, and various experimental approaches to study electron-impact double ionization have been established, each with its own advantages and limitations.

On the theoretical side, the description of such four-body systems faces challenges typical of many-body correlated roblems. First, as the number of interacting particles and degrees of freedom increases, the direct numerical evaluation of the four-body Green's function, which contains the complete spectrum of the system, becomes increasingly difficult. Second, because interacting many-particle systems are generally non-integrable, analytical treatments can only provide approximate solutions.

Various theoretical methods have been developed to address these challenges and to identify qualitatively the possible mechanisms of DI, ranging from perturbative many-body treatments (first- and second-order theories) to non-perturbative and fully numeri-

cal approaches.

A very useful way to identify the dominant physical pathways that contribute to the measured cross sections is a multiple-scattering expansion of the full scattering operator. Individual terms of this expansion can be associated with pictorial scattering mechanisms and with characteristic kinematic signatures in the measured spectra [8].

Broadly, the mechanisms leading to DI can be classified into indirect and direct processes. Indirect mechanisms involve more elaborate sequences of interactions, often mediated by the residual ion or involving multiple scatterings beyond the two active electrons. These can include processes such as projectile–ion scattering followed by electron emission, recoil effects, and interference between competing pathways. Other mechanisms of this type have been reported in the literature [32], but they are generally more system specific and play a secondary role under typical high-energy collision conditions.

In contrast, direct mechanisms are those in which double ionization results primarily from one or two dominant interactions involving the projectile and the target electrons. Among these, *Shake-Off (SO)*, *Two-Step 1 (TS1)* (first-order process), and *Two-Step 2 (TS2)* (second-order process) are recognized as the principal mechanisms responsible for electron double ionization of atoms and moleculesn in many experimental and theoretical studies, especially at intermediate to high projectile energiess, [33, 34]. The FDCS corresponding to them can be expressed as:

$$\frac{d^5\sigma}{d\Omega_s d\Omega_1 d\Omega_2 dE_1 dE_2} = \frac{k_1 k_2 k_s}{k_i} \left| M_{SO} + M_{TS1} + M_{TS2} \right|^2 \tag{2.43}$$

where the transision amplitudes $M_{SO}$, $M_{TS1}$ and $M_{TS2}$ correspond respectively to the SO, TS1 and TS2 processes.

In what follows, we will focus on these three direct mechanisms, as they are the most relevant to our study. A more comprehensive discussion of all double ionization mechanisms, including these three, can be found in Berakdar et al. [35].

### 2.5.4.1 Shake-Off (SO)

The shake-off (SO) mechanism was the first pathway proposed for double ionization [34]. It is described within the first-order Born approximation, where the corresponding transition amplitude $M_{SO}$ for a helium-like atom is given by:

$$M_{SO} = -\frac{1}{2\pi} \left\langle \Psi^-(\vec{k}_1, \vec{k}_2; \vec{r}_1, \vec{r}_2)\, e^{i\vec{k}_s \cdot \vec{r}_0} \middle| -\frac{2}{r_0} + \frac{1}{r_{01}} + \frac{1}{r_{02}} \middle| e^{i\vec{k}_i \cdot \vec{r}_0}\, \Phi_i(\vec{r}_1, \vec{r}_2) \right\rangle \tag{2.44}$$

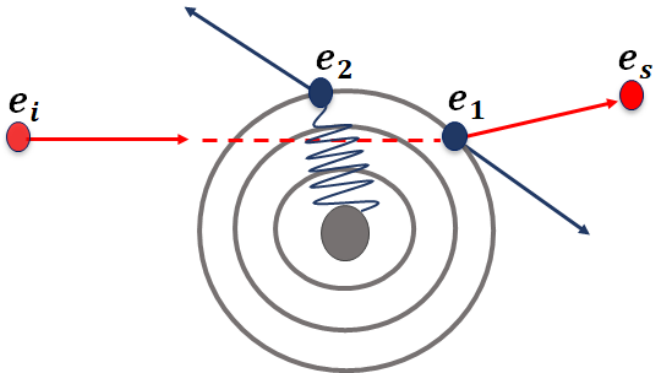


**Figure 2.4:** Diagram illustrating the Shake-Off mechanism of double ionization (DI).

In the SO mechanism the projectile removes (or strongly perturbs) one electron and is emitted into the direction of $\vec{K}$ so rapidly that the second electron, seeing effectively the sudden change from a neutral core to a doubly charged core, is projected into the continuum without further interaction with the projectile.

#### 2.5.4.2 Two-Step 1 (TS1)

TS1 is a double binary collision process in which the projectile (incident electron) first hits an active electron. In a subsequent electron–electron collision, energy is transferred to the second electron, causing its ejection. This sequential mechanism leads to the stepwise emission of the two electrons, hence the designation Two-Step 1 (TS1).

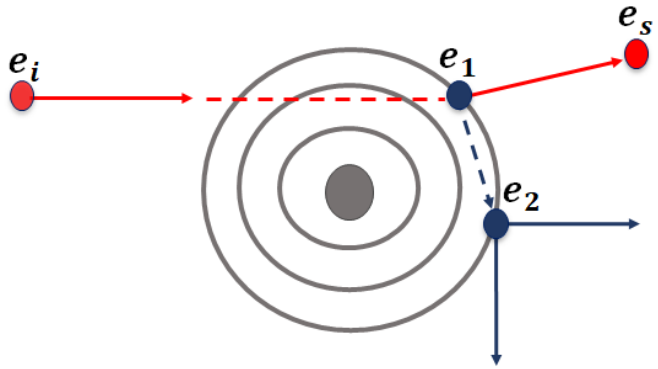


**Figure 2.5:** Diagram illustrating the Two-Step 1 mechanism of double ionization (DI).

For this mechanism, the contribution $M_{\mathrm{TS1}}$ for helium-likes is written as:

$$M_{\mathrm{TS1}} = \frac{1}{8\pi^4}\sum_n \int \frac{d\vec{q}}{(q^2 - k_n^2 - i\varepsilon)} \left\langle \psi^- \left(\vec{k}_1, \vec{k}_2; \vec{r}_1, \vec{r}_2\right) \left| \frac{1}{r_{12}} \right| \Phi_n \left(\vec{q}; \vec{r}_1, \vec{r}_2\right) \right\rangle$$
$$\times \left\langle \Phi_n \left(\vec{q}; \vec{r}_1, \vec{r}_2\right) e^{i\vec{k}_s \cdot \vec{r}_0} \left| -\frac{2}{r_0} + \frac{1}{r_{01}} + \frac{1}{r_{02}} \right| e^{i\vec{k}_i \cdot \vec{r}_0} \Phi_i(\vec{r}_1, \vec{r}_2) \right\rangle \qquad (2.45)$$

Typical TS1 kinematics include almost perpendicular emission directions for the two electrons ($\vec{k}_1 \perp \vec{k}_2$) and a small recoil ion momentum ($q \approx 0$) in the simplest cases.

Both SO and TS1 processes are of the first order in the projectile-target interaction and show axial symmetry with respect to $\vec{K}$ [36].

#### 2.5.4.3 Two-Step 2 (TS2)

TS2 is another sequential (two-step) mechanism but with a different ordering of the binary collisions, in which the incident electron undergoes two successive interactions with distinct target electrons (Figure 2.6). In the multiple-scattering series [32, 37], TS2 arises from second-order terms in the scattering potential [35]. A signature of a second or higher order processes is a break up of the symmetry of the cross section with respect to $\vec{K}$ [36].

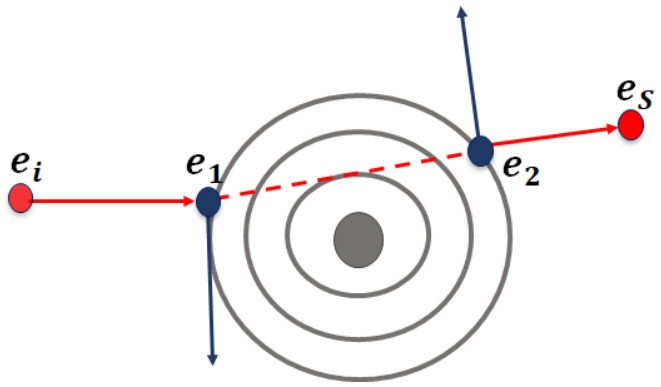


**Figure 2.6:** Diagram illustrating the Two-Step 2 mechanism of double ionization (DI).

A variant of this TS2 mechanism can also be considered. It differs from the standard process in that the first step involves a collision (elastic or inelastic) without ionization between the incident electron and the target. The second step then consists of double ionization of the target, resulting from the redistribution of energy and momentum imparted to the target during the first collision. The corresponding transition amplitude for the double ionization of the helium-like atom, $M_{\mathrm{TS2}}$, is written as [30]:

$$M_{TS2} = -\frac{1}{8\pi^4}\sum_n \int \frac{d\vec{q}}{\left(k_i^2 - q^2 - k_1^2 - 2I_n\right)} \left\langle \psi^{(-)}(\vec{k}_2, \vec{r}_2) e^{i\vec{k}_s\cdot\vec{r}_0} \left| \frac{1}{|\vec{r}_{02}|} \right| \psi_n(\vec{r}_1, \vec{r}_2) \right\rangle \times \left\langle \psi_n^{(-)}(\vec{q}; \vec{r}_1, \vec{r}_2) e^{i\vec{k}_i\cdot\vec{r}_0} \left| \frac{1}{r_0} + \frac{1}{|\vec{r}_{01}|} + \frac{1}{|\vec{r}_{02}|} \right| \psi_i(\vec{r}_1, \vec{r}_2) \right\rangle - \frac{1}{2\pi}\sum_n \int \frac{d\vec{q}}{(2\pi)^3\left(k_i^2 - q^2 - k_2^2 - 2I_n\right)} \left\langle \psi^{(-)}(\vec{k}_1, \vec{r}_1) e^{i\vec{k}_s\cdot\vec{r}_0} \left| \frac{1}{|\vec{r}_{01}|} \right| \psi_n(\vec{r}_1, \vec{r}_2) \right\rangle \times \left\langle \psi_n^{(-)}(\vec{q}; \vec{r}_1, \vec{r}_2) e^{i\vec{k}_i\cdot\vec{r}_0} \left| \frac{1}{r_0} + \frac{1}{|\vec{r}_{01}|} + \frac{1}{|\vec{r}_{02}|} \right| \psi_i(\vec{r}_1, \vec{r}_2) \right\rangle \quad (2.46)$$

where the summation over n means that we take into account all the contributions of the n discrete and continuum states of the target.

According to Eq. 2.46, interference effects between different mechanisms can arise in the calculation of FDCS [34]. Popov and co-workers [38] investigated helium double ionization at high impact energies and showed that TS1 dominates at small momentum transfer when the ejected electrons carry high energies (around 500 eV each). Their analysis included interference by adding the amplitudes of SO and TS1. Later, El Mkhanter et al. [29] and Dal Cappello et al. [33] confirmed the role of TS2 in helium double ionization at high energy, considering interference between SO and TS2, as well as combined contributions from SO, TS1, and TS2 simultaneously [39].

## 2.6 Theoretical models

The theoretical and experimental study of ionization processes induced by electron impact has attracted considerable attention. Both single ionization $(e, 2e)$ and double ionization $(e, 3e)$ provide valuable insight into the dynamics of atomic and molecular collisions. Over the years, a number of theoretical models have been proposed to interpret the information contained in differential cross sections. We briefly introduce some of them here, as they represent the most basic and accurate frameworks for describing ionization processes.

### 2.6.1 Brauner, Briggs, and Klar (BBK) model

This theoretical approach, named after its original developers Brauner, Briggs, and Klar in their study of the single ionization of hydrogen atom, provides the exact wave function for three Coulomb-interacting particles (the scattered electron, the ejected electron, and the residual ion) above their total break-up threshold and at infinite separations [21]. In their formulation, the final state is defined as the product of three Coulomb waves:

two Coulomb waves describing the interaction of the outgoing electrons with the residual ion, and the third describing the post-collisional interaction (PCI) between the two electrons. Although this type of wavefunction had already been proposed earlier by Garibotti et al. [40] in the context of ion–atom collisions, it had not been implemented until Brauner and colleagues applied it to the electron-impact problem [41].

Over time, this framework has been extended to investigate a wide range of ionization processes: for instance, electron-impact single ionization of rare gases from helium to krypton [42], as well as double ionization of helium, where Joulakian et al. [43] developed a method for calculation of the five-fold differential cross-section (FDCS) using, for the first time, correlated wavefunctions to describe the initial and final states of the colliding system within a first Born approach [39]. This BBK wavefunction satisfies the Coulomb boundary conditions exactly in the asymptotic region by representing each ejected electron by a Coulomb wave and the mutual repulsion between them by a third Coulomb wave. To render such problems tractable, the complex $N$-electron dynamics are simplified by invoking the frozen-core approximation (two active electron approximation), whereby the tightly bound inner electrons are assumed to remain unchanged during the collision. The active space is then reduced to the electrons directly involved in the ionization process. For single ionization, this leads to the single-active-electron (SAE) approximation [44], where only one electron is treated dynamically (the one that is eventually ejected). In both cases, the residual ion is represented by an effective potential arising from the nuclei and the frozen core electron density.

Later, in 1993, Dal Cappello and collaborators proposed the 2CWG model [45], in which the two ejected electrons are represented by Coulomb waves, while their mutual repulsion is incorporated through a Gamow factor. This approach simplifies the calculations and reduces computation time, providing a more accurate description of double ionization processes such as $(e, 3e)$ and $(\gamma, 2e)$ [41], although the post-collision interaction (PCI) is not treated exactly.

### 2.6.2 Distorted Wave Born Approximation (DWBA) model

The Distorted Wave Born Approximation (DWBA) model takes into account the distortions in the wavefunctions of both the incident electron and those in the outgoing channel (scattered and ejected electrons). In this approach, the incident electron is described by a distorted wave calculated in the static-exchange potential of the atom, while the scattered and ejected electrons are represented by distorted waves obtained from the exchange potential of the residual ion. The distorted wavefunctions used in this model are discussed in detail in [46].

At low projectile energies, distortion can no longer be neglected, as assumed in the standard Born approximation. The projectile then experiences a distortion potential in both the entrance and exit channels [41], representing a short-range plus Coulomb interaction between each electron and the target in its initial and final states. Consequently, the incident and outgoing electrons are described by distorted waves, while the influence of the potential becomes negligible beyond a certain distance.

At very high incident and scattered energies, distortion and exchange effects become weak for the incident and scattered electrons, which makes it useful to replace the distorted waves for these electrons with plane waves, giving rise to the Plane Wave Born Approximation (PWBA) [47].

In the context of single ionization (SI), several variants of the Distorted Wave Born Approximation (DWBA) have been proposed in the literature. For instance, the hybrid DWBA-R model, introduced by Bartschat, describes the interaction between the ejected electron and the residual ion using an R-matrix formalism [48]. Its first-order and second-order formulations are commonly referred to as DWB1-RM and DWB2-RM, respectively [49, 50].

Among the most advanced theoretical approaches developed to overcome the limitations of the DWBA is the Three-Distorted-Wave (3DW) model, proposed by Prideaux and Madison [51]. This model incorporates post-collision interactions (PCI) to more accurately describe the dynamics of the ionization process. The 3DW model, along with its molecular extension M3DW, is considered one of the most accurate and sophisticated frameworks currently used for studying electron-impact single ionization.

## 2.7 Conclusion

This chapter provided a comprehensive overview of single and double ionization, detailing both their physical mechanisms and the theoretical frameworks used for their description. The discussion emphasized the critical role of electron correlation and wavefunction-based methods in understanding many-body effects on ionization dynamics.

The rich (e, 2e) process served to illustrate single ionization, where analyzing cross sections, geometries, and incident energies yields detailed insights into electronic structure and scattering dynamics. In contrast, the (e, 3e) process highlighted the inherent complexity of double ionization, where stronger correlation effects and multiple interaction mechanisms are key.

Various theoretical models, ranging from BBK and DWBA to the more advanced 3DW/M3DW approaches, were discussed. These models demonstrate different strategies

for describing few-body interactions and underscore the necessity of accurately accounting for both electron correlation and post-collision effects.

# Bibliography

[1] J. H. McGuire. *Introduction to Dynamic Correlation in Atomic Collisions*. Cambridge University Press, 1997.

[2] P. O. Löwdin. *Advances in Chemical Physics*. In *Advances in Chemical Physics*, volume 2, page 207. 1959.

[3] R. El Mir. PhD thesis, University of Lorraine, 2015.

[4] R. Krishnan and J. B. Anderson. *J. Phys. Chem.*, 100:12960–12973, 1996.

[5] C. David Sherrill. *An Introduction to Configuration Interaction Theory*. Lecture notes, School of Chemistry and Biochemistry, Georgia Institute of Technology, 1995.

[6] M. Le Bellac. *Physique quantique, Tome II : Applications et exercices corrigés*. CNRS Éditions, Paris, 2013.

[7] P. E. Hoggan, M. B. Ruiz, and T. Özdogan. Quantum frontiers of atoms and molecules in physics, chemistry, and biology. pages 63–90. Nova Science Publishers, Inc., 1 edition, 2010.

[8] H. Hafied, A. Eschenbrenner, C. Champion, M. F. Ruiz-López, C. Dal Cappello, I. Charpentier, and P. A. Hervieux. *Chem. Phys. Lett.*, 439:55, 2007.

[9] Z. Rezkallah. PhD thesis, University of Setif1, 2011.

[10] I. Kada. PhD thesis, University of Setif1, 2009.

[11] J. L. Reed. *J. Chem. Educ.*, 76(6):802, 1999.

[12] C. David Sherrill and Henry F. Schaefer. *Adv. Quantum Chem*, 34:143–269, 1999.

[13] H. Hda, C. Dal Cappello, and J. Langlois. *Zeitschrift für Physik D*, 29:25, 1994.

[14] A. Kahros and B. J. Schwartz. *J. Phys. Chem.*, 138:054110, 2013.

[15] E. Weigold and I. E. McCarthy. *J. Phys. B*, 14:127, 1978.

[16] A. Giardini-Guidoni, R. Fantoni, R. Camilloni, and G. Stefani. *Comment. At. Mol. Phys.*, 10:107, 1981.

[17] R. Camilloni, A. Giardini-Guidoni, I. E. McCarthy, and G. Stefani. *Phys. Rev. A*, 17:1634, 1978.

[18] S. F. Zhang, C. Ning, Y. R. Huang, K. Liu, and J. K. Deng. *Acta Physica Sinica*, 58(4), 2009.

[19] Stephen R. Cotanch. *Phys. Rev. C*, 18:1941(R), 1978.

[20] D. H. Madison and O. Al-Hagan. *J. At. Mol. Opt. Phys.*, 2010:367180, 2010.

[21] M. Brauner, J. S. Briggs, and H. Klar. *J. Phys. B: At. Mol. Phys.*, 22:2265–2287, 1989.

[22] B. Mandal, M. Mondal, T. Mistry D. Jana, A. Haque, and M. Purkait. *J. Electron Spectrosc. Relat. Phenom.*, 270:147418, 2024.

[23] O. Zaidi. PhD thesis, University of Setif1, 2025.

[24] A. Lahmam-Bennani, H. F. Wellenstein, A. Duguet, and A. Daoud. *Phys. Rev. A*, 30:1511, 1984.

[25] U. Amaldi Jr, A. Egidi, R. Marconero, and G. Pizella. *Rev. Sci. Instrum.*, 40:1001, 1969.

[26] H. Houamer. PhD thesis, University of Setif 1, 2004.

[27] C. Dal Cappello, A. Haddadou, F. Menas, and A. C. Roy. *J. Phys. B: At. Mol. Opt. Phys.*, 44:015204, 2011.

[28] A. Herbadji. PhD thesis, University of Setif 1, 2022.

[29] R. El Mkhanter, C. Dal Cappello, A. L. Bennani, and Y. V. Popov. *J. Phys. B: At. Mol. Opt. Phys.*, 29:1101–1107, 1996.

[30] C. Dal Cappello, R. El Mkhanter, and P. A. Hervieux. *Phys. Rev. A*, 57(2), 1998.

[31] E. Wang, Y. Tang, Z. Shen, M. Gong, X. Shan, and X. Chen. *Phys. Rep.*, 86:066108, 2015.

[32] J. Berakdar. *Phys. Rev. A*, 63:012706, 2000.

[33] C. Dal Cappello, C. Champion, I. Kada, and A. Mansouri. *Phys. Rev. A*, 83:062716, 2011.

[34] R. J. Tweed. *Z. Phys. D*, 23:309, 1992.

[35] J. Berakdar, A. Lahmam-Bennani, and C. Dal Cappello. *Phys. Rep.*, 374:91, 2003.

[36] A. Dorn, A. Kheifets, C. D. Schröter, B. Najjari, C. Höhr, R. Moshammer, and J. Ullrich. *Phys. Rev. A*, 65:032709, 2002.

[37] J. Berakdara, A. Lahmam-Bennani, and C. Dal Cappello. *Phys. Rep.*, 374:91–164, 2003.

[38] Y. V. Popov, C. Dal Cappello, B. Joulakian, and N. M. Kuzmina. *J. Phys. B: At. Mol. Opt. Phys.*, 27:1599, 1994.

[39] B. Joulakian, C. Dal Cappello, and M. Brauner. *J. Phys. B: At. Mol. Opt. Phys.*, 25, 1992.

[40] G. Garibotti and J. E. Miraglia. *Phys. Rev. A*, 21:572, 1980.

[41] A. Naja. PhD thesis, University of Paris-Sud XI, 2008.

[42] C. Dal Cappello, H. Hda, and A. C. Roy. *Phys. Rev. A*, 51:3735, 1995.

[43] B. Joulakian and C. Dal Cappello. *Phys. Rev. A*, 47, 1993.

[44] M. Abu Samha and L. B. Madsen. *Phys. Rev. A*, 81:033416, 2010.

[45] C. Dal Cappello, B. Joulakian, and J. Langlois. *J. Phys. B: At. Mol. Opt. Phys.*, 3:125, 1993.

[46] R. van Dantzig and W. Tobocman. *Phys. Rev.*, 136:B1682, 1964.

[47] A. J. Murray. *J. Phys. B: At. Mol. Opt. Phys.*, 38:2005, 1999.

[48] K. Bartschat. *AIP Conf. Proc.*, 811:203–208, 2006.

[49] R. H. G. Reid, K. Bartschat, and A. Raeker. *J. Phys. B.* 31:563, 1998.

[50] R. H. G. Reid, K. Bartschat, and A. Raeker. *J. Phys. B.* 33:5261, 2000.

[51] A. Prideaux and D. H. Madison. *Phys. Rev. A.* 67:052710, 2003.

# Chapter 3

# Double Ionization of Beryllium Atom by Electron Impact

## 3.1 Introduction

The beryllium atom (Be) is the simplest alkaline earth metal; however, the strong interactions between its electrons make it an excellent system for studying complex many-body effects, particularly electron correlation. When investigating the double ionization of a beryllium atom that has the electronic configuration $1s^2 2s^2$, different ionization pathways may be considered. In the present work, we consider the possibility of simultaneously removing two electrons from the L-shell, which is more favorable than other pathways, such as double ionization (DI) of K-shell electrons or mixed-shell ionization (one from the K-shell and one from the L-shell). This process requires an ionization energy of $I^{++} = 27.51\,\text{eV}$. The aim of this chapter is to provide the theoretical framework for studying the double ionization of beryllium at high incident energy (1500 eV). This energy is sufficiently large to induce double ionization of almost any atom or molecule. Energies in the range of 750–5500 eV are commonly used by researchers to investigate the dynamics and cross sections of this complex process [1–4]. Furthermore, studying the high-energy electron-impact double ionization of beryllium is essential for understanding fundamental atomic processes, testing theoretical models, and providing valuable data for plasma physics applications.

In this study, the BBK model and its approximate versions, namely the 2CWG model (two Coulomb waves with Gamow factor) and the 2CWWM model (two Coulomb waves with Ward and Macek factor), are employed to present various results for the five-fold differential cross section (FDCS) of beryllium as a function of different experimental parameters of the collision system, such as the energies and angular distributions of the

incident, scattered, and the two ejected electrons. Furthermore, a comparison is made between these models, along with the 2CW model, to highlight the role of post-collision interactions (PCI).

## 3.2 The (e,3e) Double Ionization of Beryllium

The double ionization of the Be atom by electron impact, in which the two ejected electrons are detected in coincidence with the scattered electron, is schematically represented as follows:

$$e^-(E_i, \vec{k_i}) + \text{Be} \longrightarrow \text{Be}^{2+} + e^-(E_s, \vec{k_s}) + e^-(E_1, \vec{k_1}) + e^-(E_2, \vec{k_2}) \tag{3.1}$$

where $\vec{k}_i(E_i)$, $\vec{k}_s(E_s)$, $\vec{k}_1(E_1)$, and $\vec{k}_2(E_2)$ denote the momenta (energies) of the incident projectile, the scattered projectile, and the two ejected electron, respectively, as required by the conservation laws:

$$E_i = E_s + E_1 + E_2 + I^{++} \qquad \text{and} \qquad \vec{k}_i = \vec{k}_s + \vec{k}_1 + \vec{k}_2 + \vec{q}$$

$I^{++}$ and $\vec{q}$ are respectively the ionization potential and the recoil momentum.

The momentum transfer to the target is defined by:

$$\vec{K} = \vec{k}_i - \vec{k}_s$$

The magnitude and direction of the momentum transfer depend on the nature of the collision (see Chapter 2).

### 3.2.1 Initial state

The incident electron is described by a plane wave due to its relatively high energy, which allows the study of the (e,3e) process of the beryllium atom within the framework of the first Born approximation. It should be noted that, under this approximation, the theoretical models can only describe first-order processes such as shake-off (SO) and two-step 1 (TS1) (see chapter 2 ). In this case, the initial state of the collision can be expressed as:

$$\Psi_i = e^{i\vec{k}_i \cdot \vec{r}_0}\, \phi_i(\vec{r}_1, \vec{r}_2, \vec{r}_3, \vec{r}_4) \tag{3.2}$$

where $\phi_i(\vec{r}_1, \vec{r}_2, \vec{r}_3, \vec{r}_4)$ is the wavefunction of beryllium atom in its ground state.

The beryllium atom in its $^1S$ ground state, with two shells , can be expressed within the Hartree–Fock method, where it is described by a single determinant constructed

from suitable spin–orbitals. In this work, we employ the Slater-type orbitals provided by Clementi and Roetti [5]. Thus, the function $\phi_i(\vec{r}_1, \vec{r}_2, \vec{r}_3, \vec{r}_4)$ reduces to a simple product of Hartree–Fock orbitals, written as:

$$\phi_i(\vec{r}_1, \vec{r}_2, \vec{r}_3, \vec{r}_4) = u_{1s}(\vec{r}_1)\, u_{1s}(\vec{r}_2)\, u_{2s}(\vec{r}_3)\, u_{2s}(\vec{r}_4) \tag{3.3}$$

The orbitals defined by Clementi for the case $l = 0$ take the form:

$$u_{ns}(r) = \sum_i a_{ni} N_{si} e^{-\alpha_{si} r} r^{\mu_{si}} Y_0^0 \tag{3.4}$$

where each orbital $u_{ns}$ is described as a linear combination of $i$ basis functions, with the corresponding parameters $\alpha_i$ and $\mu_i$ given in Table 3.1, taken from [6]. The term $Y_0^0 = \frac{1}{\sqrt{4\pi}}$ represents the spherical harmonic corresponding to the quantum number $l = 0$. The normalization factors $N_{si}$ is defined as:

$$N_{si} = \frac{(2\alpha_{si})^{\mu_{si}+\frac{3}{2}}}{\sqrt{[2(\mu_{si}+1)]!}} \tag{3.5}$$

**Tableau 3.1:** Parameters of the HF $1s$ and $2s$ orbitals of Be [6]

| Basis of $i$ terms | | $\alpha_{si}$ | $a_{1i}$ (1s) | $a_{2i}$ (2s) |
|---|---|---|---|---|
| $i$ | $\mu_{si}$ | | | |
| 1 | 0 | 3.4703 | -0.91792 | -0.17065 |
| 2 | 0 | 6.3681 | 0.08742 | -0.01469 |
| 3 | 1 | 0.7516 | 0.00147 | 0.11551 |
| 4 | 1 | 0.9084 | -0.00267 | -0.67835 |
| 5 | 1 | 1.4236 | 0.00222 | 0.30265 |
| 6 | 1 | 2.76163 | 0.00597 | -0.09232 |

### 3.2.2 Final state

The two atomic electrons, once ejected, are found beyond the double ionization threshold but still within the Coulomb field of the ion and under their mutual interaction. The quantum description of this electronic Coulomb double continuum represents one of the fundamental problems of atomic physics [7]. In our case, we will treat this double continuum as a three-body problem, consisting of one heavy particle (the ion) and two ejected electrons, with the scattered electron assumed not to interact with them and is described by a plane wave. The double continuum is effectively described by a three-body Coulomb

(3C) wave function (BBK wave function) [8], where two wave functions represent the ejected electrons, while the third one is represents the repulsion of these two laters (post collision interaction). The final state of the collision is then given by:

$$\Psi_f = e^{i\vec{k}_s\cdot\vec{r}_0}\,\phi_f(\vec{k}_1,\vec{r}_1,\vec{k}_2,\vec{r}_2) \tag{3.6}$$

The wavefunction for the double continuum state of the beryllium atom $\phi_f(\vec{k}_1,\vec{r}_1,\vec{k}_2,\vec{r}_2)$ can be written (taking into account the possible exchange between the two ejected electrons) as follows:

$$\phi_f(\vec{k}_1,\vec{r}_1,\vec{k}_2,\vec{r}_2) = \frac{1}{\sqrt{2}}\Big[\phi_c(\vec{k}_1,\vec{r}_1)\phi_c(\vec{k}_2,\vec{r}_2) \pm \phi_c(\vec{k}_1,\vec{r}_2)\phi_c(\vec{k}_2,\vec{r}_1)\Big]C(a_{12},\vec{k}_{12},\vec{r}_{12}) \tag{3.7}$$

with

$$\phi_c(\vec{k_j},\vec{r_j}) = \frac{e^{i\vec{k_j}\cdot\vec{r_j}}}{(2\pi)^{3/2}}\,{}_1F_1\Big(-i\alpha_j,\,1,\,-i(\vec{k_j}\cdot\vec{r_j}+k_jr_j)\Big)\;e^{\frac{\pi\alpha_j}{2}}\,\Gamma(1+i\alpha_j)\,, \qquad j=1,2 \tag{3.8}$$

The term $C(a_{12},k_{12},\vec{r}_{12})$ describes the PCI in the final state, and it is expressed as:

$$C(\alpha_{12},\vec{k}_{12},\vec{r}_{12}) = \exp\left(-\frac{\pi\alpha_{12}}{2}\right)\Gamma\left(1-i\alpha_{12}\right)\,{}_1F_1\left(-i\alpha_{12},1,-i(\vec{k}_{12}\cdot\vec{r}_{12}+k_{12}r_{12})\right) \tag{3.9}$$

where $\alpha_j = -\frac{Z}{k_j}$ with $Z=2$, and $\alpha_{12} = \frac{1}{2k_{12}}$ with $\vec{k}_{12} = \frac{1}{2}\left(\vec{k}_1-\vec{k}_2\right)$.

### Two Coulomb Waves (2CW) model

This model, introduced by Byron and Joachain [9, 10], simplifies the final state of the reaction, by taking into account the Coulomb interaction between the two ejected electrons and the residual ion, and neglects the interactions between these two electrons, so The wavefunction for the double continuum state is represented by two non-correlated Coulomb waves, written as follows:

$$\phi_f(\vec{k}_1,\vec{r}_1,\vec{k}_2,\vec{r}_2) = \frac{1}{\sqrt{2}}\Big[\phi_c(\vec{k}_1,\vec{r}_1)\phi_c(\vec{k}_2,\vec{r}_2) \pm \phi_c(\vec{k}_1,\vec{r}_2)\phi_c(\vec{k}_2,\vec{r}_1)\Big] \tag{3.10}$$

The Coulomb wave $\phi_c(\vec{k}_j,\vec{r}j)_{j=1,2}$ is given by the expression in Eq. (3.8).

### Two Coulomb Waves with Gamow factor (2CWG) model

In order to simplify the calculations while maintaining physical accuracy, we employ the two Coulomb Waves with Gamow factor (2CWG) model. In this model, the incident and

the scattered particles are described by plane waves, while the two ejected electrons are described by Coulomb waves with a Gamow factor to take into account the repulsion between them. Hunce, the term in Eq. 3.9 will be approximate to the Gamow factor [11]:

$$\varphi_G(k_{12}) = \frac{\pi \exp(-\pi/k_{12})}{k_{12}\left[1 - \exp(-\pi/k_{12})\right]} \tag{3.11}$$

**Two Coulomb Waves with Ward and Macek factor (2CWWM) model**

Another way to simplify the calculation and achieve a shorter computation time without losing the physical aspect of the Coulomb repulsion between the two continuum electrons is by using the 2CWWM model. It is well established in the literature that the Gamow factor leads to a significant reduction in the amplitude of the cross sections [12]. For this reason, the 2CWWM model was developed to partially correct the effect of the Gamow factor. This model, proposed by Ward and Macek [13], is based on evaluating the distortion $C(\alpha_{12}, \vec{k}_{12}, \vec{r}_{12})$ at a fixed, nonzero distance. The Ward and Macek factor is given by:

$$\varphi_{WM}(k_{12}, r_{312\text{ave}}) = \frac{\pi \exp(-\pi/k_{12})}{k_{12}\left[1 - \exp(-\pi/k_{12})\right]} \left|{}_1F_1(-i\alpha_{12},\, 1,\, -2ik_{12}r_{12\text{ave}})\right|^2 \tag{3.12}$$

The distance $r_{12\text{ave}}$ obtained by Ward and Macek [13] is given by:

$$r_{12\text{ave}} = \frac{\pi^2}{16\varepsilon}\left(1 + \frac{0.627}{\pi}\sqrt{\varepsilon}\ln\varepsilon\right)^2 \tag{3.13}$$

Where $\varepsilon = \frac{1}{2}(k_1^2 + k_2^2)$

## 3.3 Five-Fold Differential Cross Section (FDCS)

The expression of the five-fold differential cross section (FDCS) in the first Born approximation (FBA) takes the form:

$$\frac{d^5\sigma}{d\Omega_s\, d\Omega_1\, d\Omega_2\, dE_1\, dE_2} = \frac{k_s k_1 k_2}{k_i}\left|f_{B1}\right|^2 \tag{3.14}$$

where $d\Omega_s$, $d\Omega_1$, and $d\Omega_2$ are the solid angle elements of the scattered and the two ejected electrons, respectively.

The scattering amplitude $f_{B1}$ is:

$$f_{B1} = -\frac{1}{2\pi}\langle\Psi_f|V|\Psi_i\rangle \tag{3.15}$$

where $V$, the interaction potential between the incident electron and the beryllium atom, is giving by:

$$V = \sum_{k=1}^{4} \frac{1}{|\vec{r}_k - \vec{r}_0|} - \frac{Z}{|\vec{r}_0|} \tag{3.16}$$

with $Z = 4$, where $\vec{r}_0$ denotes the position vector of the incident electron relative to the nucleus, and $\vec{r}_k$ denotes the position vectors of each of the four target electrons relative to the nucleus.

## Approximation method

We assume that only the $2s^2$ valence electrons are ionized, while the tightly bound $1s^2$ electrons remain unaffected (frozen-core approximation [14]). Thus, Eq. (3.15) can be written as:

$$f_{B1} = -\frac{1}{2\pi} \left\langle \phi_f(\vec{k}_1, \vec{k}_2, \vec{r}_1, \vec{r}_2)\, e^{i\vec{k}_s \cdot \vec{r}_0} \mid V' \mid e^{i\vec{k}_i \cdot \vec{r}_0}\, \phi_i(\vec{r}_1, \vec{r}_2) \right\rangle \tag{3.17}$$

where the Coulomb interaction potential between the incident electron and the two active electrons (which will be ejected subsequently) is:

$$V' = -\frac{2}{r_0} + \frac{1}{|\vec{r}_0 - \vec{r}_1|} + \frac{1}{|\vec{r}_0 - \vec{r}_2|} \tag{3.18}$$

The calculation of FDCS using the BBK model has already been applied in several studies for different targets. In particular, we note the work of Joulakian *et al.* [15], who used this approach to investigate the double ionization of helium. However, this procedure involves a large number of derivatives. An alternative method is based on the double Fourier transform according to Kornberg and Miraglia [16], which reduces the six-dimensional integral to three dimensions while avoiding the use of ${}_1F_1$. This makes it possible to employ more sophisticated initial wavefunctions, such as those of Clementi and Roetti [5] or configuration–interaction wavefunctions. However, this method requires the introduction of a parameter $\beta$ (via the factor $e^{-\beta r12}$, see Appendix A), which must approach zero. In our calculations, we adopted the value $\beta = 0.005$, as it provides an optimal balance between computational cost and numerical accuracy. The detailed calculation of the scattering amplitude (Eq. 3.17) by BBK, 2CWG and 2CWWM models is giving in Appendix A.

## 3.4 Results

The present study is carried out in the context of the first Born approximation, where the initial state of the bound electrons in the beryllium atom is represented by a HF function (Table 3.1). The three-Coulomb-wave model (BBK), 2CWG, 2CWWM, and 2CW are used to describe the final state of the electrons emerging into the continuum. To our knowledge, no (e,3e) experiments on beryllium have been performed so far. In this work we aim to determine optimal energies and angular conditions for the experimental realization of the double ionization of the beryllium atom, comparable to those widely used in experimental studies of atomic double ionization, such as the experiments performed in France (Orsay group) [17] and in Germany (Max Planck Institute in Heidelberg) [18].

We propose to study the double ionization process at a high impact energy of 1500 eV, which was found by Becher et al. [2] to exhibit remarkable FDCS features in the study of the double ionization of the $L$ shell of beryllium in coplanar geometry, and for relatively low ejection energies $E_1, E_2 \leq 40\,\text{eV}$. The experimental detection characteristics of the scattered and the two ejected electrons are obtained through the analysis of the plots describing the variation of the Five-fold differential cross section (FDCS) with the different system parameters (energies and directions of the scattered or ejected electrons).

### 3.4.1 Variation of the (e,3e)-Be FDCS with the scattering angle $\theta_s$

Among all possible scenarios, we consider the case where the two ejected electrons have the same energy $E_1 = E_2 = 10\,\text{eV}$, in which one of them is parallel to the momentum transfer $\vec{K}$ Figures 3.1(a) and 3.1(b).

Indeed, as $\theta_s$ increases, the vector $\vec{K}$ passes through a situation where it's magnitude becomes equal to that of the ejected electron, $\vec{K} = \vec{k}_1$. Momentum conservation then leads to the equality $\vec{q} = \vec{k}_2$. This particular situation corresponds graphically to the peak observed on the Figure 3.1 (a) with $(\vec{k}_1 = -\vec{k}_2)$ located around $\theta_s = 0.2° - 0.3°$ , and on the Figure 3.1 (b) with $(\vec{k}_1 \perp \vec{k}_2)$ located at $\theta_s = 0.2°$ .

### 3.4.2 Variation of the (e,3e)-Be FDCS as function of $\theta_2$ (with $\theta_1 = 2\pi + 2\theta_K - \theta_2$)

We will start by discussing the binary and recoil peaks using BBK, 2CWG and 2CWWM models. We consider in Figures 3.2 and 3.3, the vareation of the FDCS with $\theta_2$, where $\theta_1$ and $\theta_2$ are varied simultaneously around the momentum transfer direction$\vec{K}$, that is, by

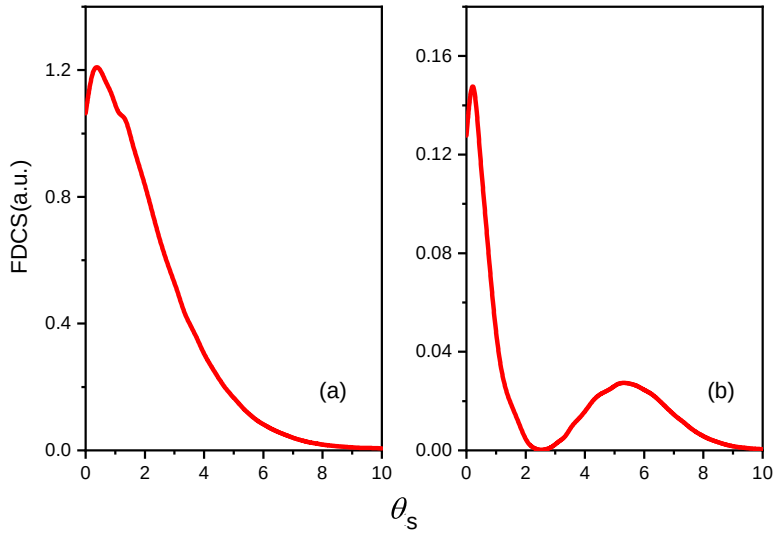


**Figure 3.1:** FDCS for the double ionization of the Be by 1.5 keV electron impact as a function of the scattering angle, with $E_1 = E_2 = 10$ eV. The first electron is ejected along the direction of the momentum transfer $\vec{K}$, while the second is ejected: a) along $-\vec{K}$,b) at an angle perpendicular to the direction of$-\vec{K}$.

taking the direction $\vec{K}$ as an axis of symmetry for the vectors $\vec{k}_1$ and $\vec{k}_2$ of the two ejected electrons ($\theta_2 = 2\pi + 2\theta_K - \theta_1$). The momentum transfer of the reaction is nearly 0.17 a.u. This discussion was already carried out by Becher et al. [2] using the BBK model, with all electrons of the beryllium atom included in the initial state.

It is clear from Figures 3.2 and 3.3 that two peaks appear. The first, known as the binary peak, occurs when $\vec{K} = \vec{k}_1 + \vec{k}_2$ ($\vec{q} = 0$). The second, referred to as the recoil peak, corresponds to the symmetric situation where $\vec{k}_1 + \vec{k}_2 = -\vec{K}$ ($\vec{q} = 2\vec{K}$).

**Tableau 3.2:** Positions of the binary and recoil peaks for theoretical and graphical results

| | **Binary peak position** | **Recoil peak position** |
|---|---|---|
| | $K = 0.17 \quad \theta_K = 347.86°$ | $K = 0.17 \quad \theta_K = 347.86°$ |
| **Classically calculated [6]** | $\theta_{1_{b,t}} = 72.2°, \quad \theta_{2_{b,t}} = 263.6°$ | $\theta_{1_{b,t}} = 83.6°, \quad \theta_{2_{b,t}} = 252.2°$ |
| **Graph Figure 3.2 (BBK results)** | $\theta_{1_{b,g}} = 60.6°, \quad \theta_{2_{b,g}} = 275.7°$ | $\theta_{1_{b,g}} = 91.4°, \quad \theta_{2_{b,g}} = 244.5°$ |
| **Graph Figure 3.3 (2CWG and 2CWWM results)** | $\theta_{1_{b,g}} = 37.2°, \quad \theta_{2_{b,g}} = 298.8°$ | $\theta_{1_{b,g}} = 104°, \quad \theta_{2_{b,g}} = 230.4°$ |
| **Graph (BBK CI results [2])** | $\theta_{1_{b,g}} = 55 - 60°, \quad \theta_{2_{b,g}} = 280°$ | $\theta_{1_{b,g}} = 90°, \quad \theta_{2_{b,g}} = 246°$ |

When comparing our BBK results with those of Becher et al. [2] (see Table 3.2), we find that the results are generally similar, with some minor differences. The position of the

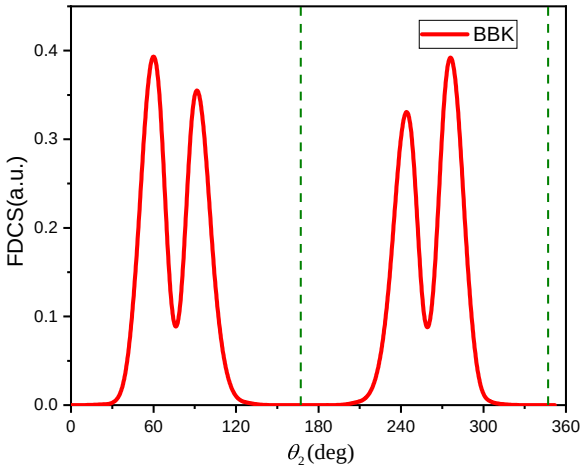


**Figure 3.2:** Variation of the FDCS with $\theta_2$ and $\theta_1 = 2\pi + 2\theta_K - \theta_2$ for $E_1 = E_2 = 10\,\text{eV}$ , $E_i = 1.5\,\text{keV}$ and $\theta_s = 0.2°$. Red solid line represents theoretical results of BBK model. The dashed vertical lines indicate the momentum transfer $\vec{K}$ and its opposite direction$-\vec{K}$. $K = 0.17$ a.u. and $\theta_k = 347.86°$.

binary peak is closer to the classical theoretical prediction [6] than the result obtained by Becher et al., while in the recoil region, the opposite behavior is observed. Furthermore, we observe that the 2CWG and 2CWWM models (Figure 3.2) exhibit similar shapes, with peaks located at the same angular positions, although the 2CWWM model predicts a higher FDCS intensity than 2CWG model. However, these results differ significantly from our BBK calculations, from Becher et al. results [2], and from the classical theoretical predictions [6]. This leads to the conclusion that the BBK model provides a more accurate description of the double-ionization process for this particular kinematic condition. In addition, Becher [6] highlights The difference between the results obtaind from the classical theory and graphs of BBK model to that quantum phenomena can only be described approximately using a classical approach.

### 3.4.3 Variation of the (e,3e)-Be FDCS with the ejection angles $\theta_1$ and $\theta_2$

#### 3.4.3.1 Case $E_1 = E_2 = 10\,\text{eV}$

We present in this section (Figure 3.4), the Variation of the FDCS for the double ionization of Be as function of ejection angles $\theta_1$ and $\theta_2$ ($E_i = 1500\,\text{eV}$ , $\theta_s = 0.2°$ , $E_1 = E_2 = 10\,\text{eV}$). Figure 3.4 highlight the spatial regions where experimental detection would be most favorable. The distribution exhibits a symmetric pattern, which is a direct consequence of

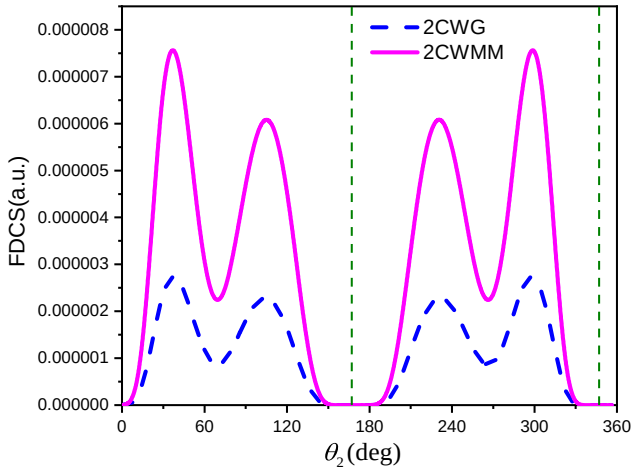


**Figure 3.3:** same as in Figure 3.2, with theoretical 2CWG results are represented by a bleu dashed line and the theoretical results of 2CWWM results are represented by a magenta solid line. The vertical dashed line represents the momentum transfer $\vec{K}$ and its opposite direction$-\vec{K}$ with $K = 0.17$ and $\theta_k = 347.86°$

the choice $E_1 = E_2$. In fact, the diagonal corresponding to $\theta_1 = \theta_2$ defines a forbidden region, where the cross section vanishes since both electrons cannot be ejected in the same direction with identical energies (Coulomb repulsion) [19].

We observe three lobes. The first one extends over $\theta_1 \in [0°, 75°]$ and $\theta_2 \in [260°, 335°]$, with a maximum characterized by $|\theta_1 - \theta_2| \approx 260°$ corresponding to a forward scattering mainly due to the TS1 mechanism, in which the incoming electron collides with a target electron that is ejected along the direction of the momentum transfer $\vec{K}$ (or symmetrically in the opposite direction). This ejected electron then collides with another target electron. This second collision is not purely elastic (quasi-elastic) [20], and the strong electrostatic repulsion leads to an angle $|\theta_1 - \theta_2| = 100° > 90°$. We also observe two secondary lobes with less pronounced maxima. The first extends over $\theta_1 \in [140°, 188°]$ and $\theta_2 \in [334°, 358°]$, with a maximum characterized by $|\theta_1 - \theta_2| = 180°$. The second extends over $\theta_1 \in [88°, 114°]$ and $\theta_2 \in [216°, 243°]$, with a maximum characterized by $|\theta_1 - \theta_2| = 130°$ associated to a backward emission of the TS1. The remaining three lobes are obtained directly through symmetry considerations.

#### 3.4.3.2 Case $E_1 = 5\,\mathbf{eV}$ and $E_2 = 15\,\mathbf{eV}$

Figure 3.5 represents the same situation as in Figure 3.4, but for different ejection energies ($E_1 = 15$ eV, $E_2 = 5$ eV).

The results obtained here show four lobes: two large lobes with maximum amplitudes

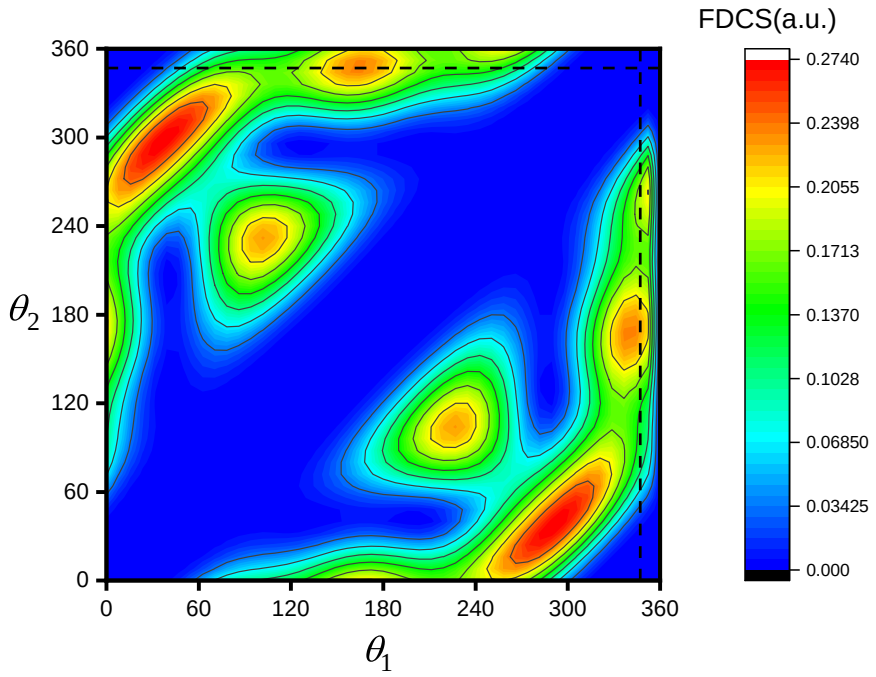


**Figure 3.4:** color-scale representation of the FDCS in a.u., for L-shell double ionization, as a function of the ejection angles $\theta_1$ and $\theta_2$ and for equal asymptotic energies$E_1 = E_2 = 10\,\text{eV}$. The energy of the incident electron is fixed at $E_i = 1.5\,\text{eV}$ and the scattering angle is $\theta_s = 0.2°$.

on the order of $1.59\,a.u.$, characterized by $|\theta_1 - \theta_2| \approx 175°$. This indicates that the SO mechanism is the main process involved in the double-ionization. The first lobe extends over $\theta_1 \in [0°, 30°]$ and $\theta_2 \in [100°, 260°]$, with a maximum centered around $(\theta_1, \theta_2) = (0°, 176°)$, while the second extends over $\theta_1 \in [298°, 356°]$ and $\theta_2 \in [66°, 263°]$, with a maximum centered around $(\theta_1, \theta_2) = (341°, 165°)$. The SO mechanism is identified by the emission of one electron along the momentum transfer $+\vec{K}$, which induces a rearrangement of the target electrons and leads to the ejection of a second electron in the opposite direction.

The other two lobes are characterized by $|\theta_1 - \theta_2| \approx 130°$. One extends over $\theta_1 \in [298°, 356°]$ and $\theta_2 \in [66°, 263°]$, with a maximum centered around $(\theta_1, \theta_2) = (141°, 270°)$, while the other extends over $\theta_1 \in [158°, 222°]$ and $\theta_2 \in [28°, 102°]$, with a maximum centered around $(\theta_1, \theta_2) = (194°, 63.8°)$. These two lobes are associated with the TS1 mechanism.

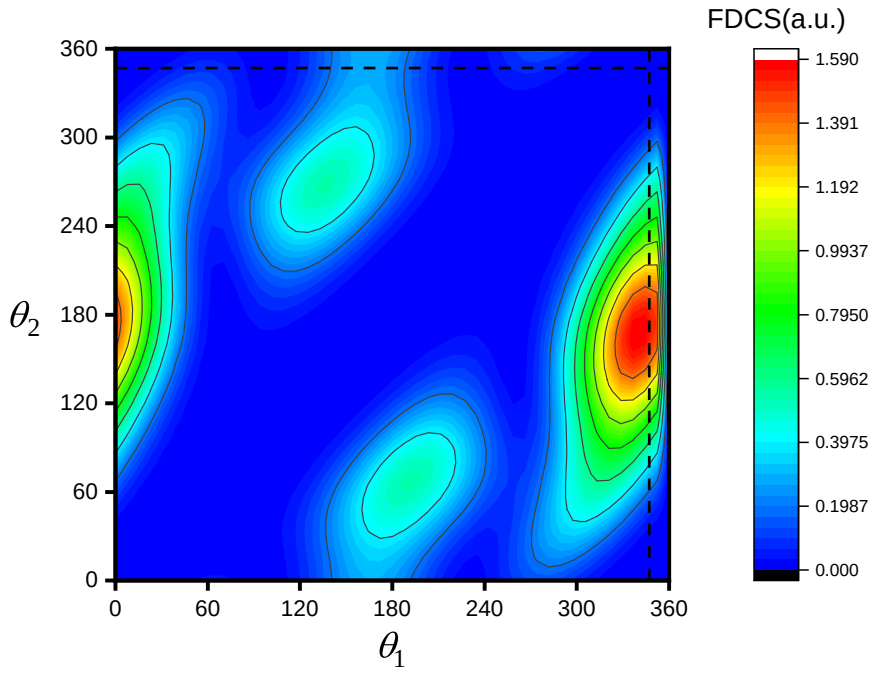


**Figure 3.5:** color-scale representation of the FDCS in a.u., for L-shell double ionization, as a function of the ejection angles $\theta_1$ and $\theta_2$ and for ejection energies $E_1 = 15$ and $E_2 = 5\,\text{eV}$. The energy of the incident electron is fixed at $E_i = 1.5\,\text{eV}$ and the scattering angle is $\theta_s = 0.2°$. The dashed lines are the direction of the transfert momentum.

### 3.4.4 Variation of the (e,3e)-Be FDCS with one ejection angle $\theta_1$ (with $\theta_2$ fixed)

In Figures 3.6-(a) and 3.6-(b), the FDCS is plotted as a function of $\theta_2$ for $\theta_1 = \theta_k = 347.86°$ by 1.5 keV impact energy, with $\theta_s = 0.2°$ in coplanar geometry. We compared the BBK results with the 2CW, 2CWG, and 2CWWM models. The data obtained from BBK model are cross normalized to 2CWWM model to establish an absolute scale, as well as for 2CW and 2CWG models. We observe for both cases (a) and (b) that the shape of the 2CW result is different from the others, and the peak is not pronounced. This may be attributed to the neglect of the post-collision interaction (PCI), unlike in the BBK, 2CWG, and CWWM models, where it is included either through the Coulomb wave (BBK), the Gamow factor (2CWG), or the Ward and Macek factor (2CWWM).

Figure 3.6-(a) corresponds to the energy case $E_1 = 15$ and $E_2 = 5$ eV, where the faster ejected electron is detected along the momentum transfer direction. The maximum is observed at $\theta_2 = 168° \approx -\theta_K$ for BBK, 2CWG, and 2CWWM models. This angular position corresponds to the condition of minimum recoil ion momentum, where $\vec{q} = \vec{K}$. This behavior can be interpreted in terms of the SO mechanism. Such a back-to-back

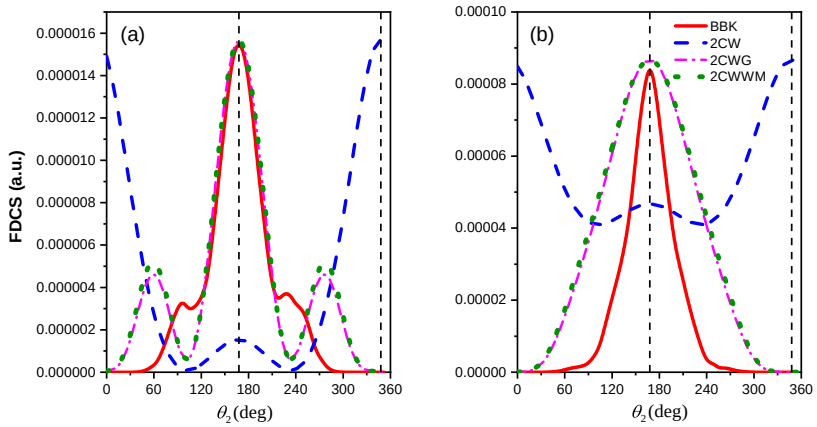


**Figure 3.6:** Variation of the FDCS with $\theta_2$ for L-shell double ionization, with $\theta_1 = \theta_k$, $E_i$ = 1.5 keV, and $\theta_s = 0.2°$. BBK theoretical results are represented by a red solid line. 2CW (multiplied by 0.02 in (a) and by 0.27 in (b)), 2CWG (multiplied by 2.7 in (a) and (b)) and 2CWWM theoretical results are represented by a bleu dashed line, magenta dashed dotted line, and green dotted line,respectively. The vertical dashed line represents the momentum transfer $\vec{K}$ and its opposite direction$-\vec{K}$ with $K = 0.17\,a.u.$ and $\theta_k = 347.86°$. (a) $E_1 = 15\,, E_2 = 5$ eV. (b) $E_1 = 5\,, E_2 = 15$ eV.

emission of the two outgoing electrons has been previously reported in many studies (such as [18, 21]).

Figure 3.6-(b) corresponds to the same configuration as Figure 3.6-(a), but with $E_1 = 5$ eV and $E_2 = 15$ eV. In this case, the slower ejected electron is detected along the momentum transfer direction, and the angular position of the maximum ($\theta_2 = 167.6° \approx -\theta_K$) remains consistent across the BBK, 2CWG, and 2CWWM models. However, the 2CWG and 2CWWM models exhibit a larger peak compared to the BBK model.

The slow electron (5 eV) is ejected along $+\vec{K}$, and the second electron (15 eV) is ejected along $-\vec{K}$. This corresponds to the back-to-back emission (the SO mechanism).

We now consider another situation corresponding to equal energy sharing, where $E_1 = E_2 = 10$ eV (Figures 3.7-(a) and 3.7-(b)). The present analysis is performed within the framework of the BBK model (red solid line), and the obtained results are compared with those reported by Becherer *et al.* [2], who employed the BBK model with the Jastrow fully correlated function for the Be initial state where the influence of the inner electrons has been also effectively considered (green dashed dotted line). The choice of the kinematical conditions are also taking from [2]. In this context, our primary objective is to simplify the computational procedure in order to reduce the overall calculation time while maintaining a satisfactory level of accuracy with the existence theoratical results. Our results are normalized to the maximum value of those obtained by Becher et al. [2], to provide the best visual comparison. In Figure 3.7-(a) ($\theta_1 = 285°$), two distinct peaks are clearly

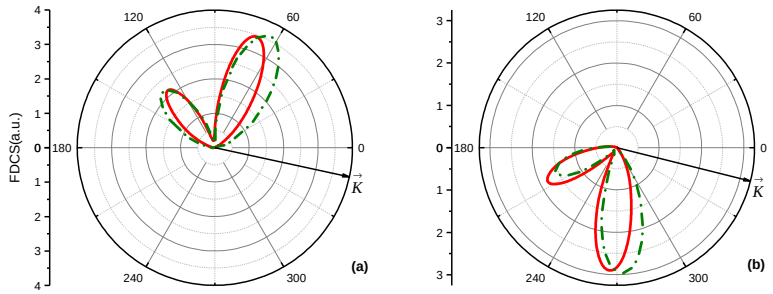


**Figure 3.7:** Variation of the FDCS with $\theta_2$ for L-shell double ionization, for different values of $\theta_1$, with $E_i = 1.5$ keV, and $\theta_s = 0.2°$. Our theoretical $BBK$ results are represented by a red solid line and the theoretical results of Becher et al. are represented by a green dashed dotted line. (a) $\theta_1 = 285°$. (b) $\theta_1 = 50°$.

observed around $\theta_2 = 70°$ (binary peak) and $\theta_2 = 130°$ (recoil peak) in our results, and around $\theta_2 = 64°$ and $\theta_2 = 134°$ in those of Becherer *et al.* [2]. It is evident that the two sets of results exhibit a similar shape, with a slight shift in the position of both peaks (6° for binary peak and 4° for recoil peak). Here, the binary lobe is more pronounced than the recoil lobe for both models. It should be noted that there is an interference between the TS1 and SO mechanisms. The same analysis can be applied to the case $\theta_1 = 50°$ shown in Figure 3.7(b). Once again, both results exhibit a similar shape, with a slight shift in the position of the recoil peak. It should be noted that the lobe with the highest amplitude here corresponds to the recoil peak. Furthermore, an interference between the TS1 and SO mechanisms can be observed. In general, there is a good agreement between the two theoretical models in terms of shape, with only a small shift in the positions of the peaks, most likely caused by the correlation effects of the initial-state wave function used.

## 3.5 Conclusion

In this chapter, the L–shell double ionization of beryllium by electron impact was investigated using the BBK model and its approximation 2CWG and 2CWWM models, in which the post-collision interaction (PCI) is included and treated exactly. The analysis of the five-fold differential cross sections (FDCS) revealed a strong dependence on the scattering geometry, as well as on the ejected electron energies and directions. The results exhibited distinct binary and recoil structures with a pronounced forward–backward asymmetry, which is most prominent at small momentum transfer. Moreover, a comparison between

our results and those obtained by Becherer et al. [2] (Figure 3.7), show a reasonable consistency between the two theories, confirming the reliability of our simplified approach and its effectiveness in reducing computational time.

# Bibliography

[1] M.-T. Huang, L. Zhang, S. Hasegawa, and S. H. Southworth. *Phys. Rev. A*, 66(1), 2002.

[2] M. Becher, B. Joulakian, C. Le Sech, and M. Chrysos. *Phys. Rev. A*, 77:052710, 2008.

[3] N. Watanabe, K. A. Kouzakov, Yu. V. Popov, and M. Takahashi. *Phys. Rev. A*, 77:032725, 2008.

[4] C. Dal Cappello, R. El Mkhanter, and P. A. Hervieux. *Phys. Rev. A*, 57(2), 1998.

[5] E. Clementi and C. Roetti. *Atomic Data and Nuclear Data Tables*, 14:177, 1974.

[6] M. Becher. PhD thesis, University of Paul Verlaine Metz, France, 2008.

[7] C. W. McCurdy, M. Baertschy, and T. N. Rescigno. *J. Phys. B: At. Mol. Opt. Phys.*, 37:R137, 2004.

[8] M. Brauner, J. S. Briggs, and H. Klar. *J. Phys. B: At. Mol. Phys.*, 22:2265–2287, 1989.

[9] F. W. Byron Jr. and C. J. Joachain. *Phys. Rev.*, 164, 1967.

[10] F. W. Byron Jr. and C. J. Joachain. *Phys. Rev. Lett.* 16:1139, 1966.

[11] C. Dal Cappello, B. Joulakian, and J. Langlois. *J. Phys.*, 3:125, 1993.

[12] R. El Mir. PhD thesis, University of Lorraine, 2015.

[13] S. J. Ward and J. H. Macek. *Phys. Rev. A*, 49:1049, 1994.

[14] H. Hda, C. Dal Cappello, and J. Langlois. *Zeitschrift für Physik D*, 29:25, 1994.

[15] B. Joulakian and C. Dal Cappello. *Phys. Rev. A*, 47, 1993.

[16] M. A. Kornberg and J. E. Miraglia. *Phys. Rev. A*, 48:3714, 1993.

[17] A. Lahmam-Bennani, C. Dupré, and A. Duguet. *Phys. Rev. Lett.*, 63:1582, 1989.

[18] A. Dorn, A. Kheifets, C. D. Schröter, B. Najjari, C. Höhr, R. Moshammer, and J. Ullrich. *Phys. Rev. A*, 65:032709, 2002.

[19] P. Bolognesi, G. C. King, and L. Avaldi. *Radiation Physics and Chemistry*, 70:207–236, 2004.

[20] C. Dal Cappello, C. Champion, I. Kada, and A. Mansouri. *Phys. Rev. A*, 83:062716, 2011.

[21] A. Mansouri I. Kada, C. Dal Cappello, P. A. Hervieux, and A. C. Roy. *J. Phys. B: At. Mol. Opt. Phys.*, 42:025201, 2009.

# Chapter 4

# Single and Double Ionization of Water Molecule

## 4.1 Introduction

As water is the main constituent of biological matter, studying the ionization of water molecules is essential for understanding the damage caused to living tissues by ionizing radiation [1, 2]. It is now well established that there are strong correlations between exposure to ionizing radiation and the biophysical processes that lead to complex DNA damage, as well as gene and chromosomal mutations. In particular, the production of low-energy secondary electrons resulting from the primary ionization of water is important to elucidate the mechanisms that lead to cellular damage.

In this chapter, we will study the single ionization (SI) of the water molecule[1] and the double ionization (DI) of the oriented water molecule by electron and positron impact.

For single ionization (SI), we investigate the influence of the projectile charge. While electron-impact ionization has been extensively studied [3–5], positron-impact ionization remains relatively unexplored, offering new insights into charge-related effects. The calculations are carried out using the M3CWZ model, which incorporates a variable charge approximation within the BBK framework [6, 7]. This model has already been applied in our previous works on nitrogen and water molecules [3, 8]. The continuum particles for positron impact are represented by Coulomb waves with position-dependent charges $Z(r)$.

For double ionization (DI), we investigate the influence of the initial-state wavefunction

[1] This part of the chapter (in particular sections 4.2 and 4.4) is reproduced from: I. Khiat, S. Houamer, I. Kada, S. Mekhalfa, A. Tamin, and C. Dal Cappello, "Projectile charge effects in ionization of water molecule by positron and electron impact." *Eur. Phys. J. D* **79**, 68 (2025), with the permission of Springer Nature.

on the (e,3e) differential cross sections of $H_2O$ at a fixed molecular orientation. Using the 2CWG model within the framework of the first Born approximation (FBA) (see Chapter 3), we calculate the six-fold differential cross sections (6DCSs) and compare our results with previous studies [9, 10].

## 4.2 Description of the target

In this work, we investigate the single ionization (SI) of the water molecule induced by electron and positron impact, as well as its double ionization (DI) caused by electron impact. To model the target, the $H_2O$ molecular wave functions are represented following the approach of Hafied et al. [11], in which the bound state is expressed as a linear combination of single–center atomic orbital–molecular orbital (LCAO-MO) functions localized on the oxygen atom. The resulting symmetry properties are essential for data interpretation, theoretical calculations, and for averaging the target wavefunctions over all orientations prior to the collision. Representing the molecular states with single-center orbitals is particularly convenient for systems of the type $XH_n$, such as $H_2O$ (see [7, 12, 13]). Below, we outline the procedure used to construct the single-center wave functions.

The first step consists of calculating the molecular orbitals using the Gaussian 03 package [14] within the Hartree–Fock framework. The accuracy of these orbitals is verified by comparing selected computed molecular properties with available experimental data (see [11] and references therein). In the second step, the multicentered orbitals obtained from these calculations are transformed into single–center expansions of Slater–type functions centered on the oxygen nucleus, by means of a partial–wave expansion technique [15], namely:

$$\phi_i(\vec{r}) = \sum_{k=1}^{N_i} a_{ik}\, \Phi^{\xi_{ik}}_{n_{ik}l_{ik}m_{ik}}(\vec{r}) \tag{4.1}$$

where $N_i$ denotes the number of Slater functions employed in the expansion of the $i^{\text{th}}$ orbital, and $a_{ik}$ represents the weight of each atomic component.

In Eq. 4.1, the basis function $\Phi^{\xi_{ik}}_{n_{ik}l_{ik}m_{ik}}(\vec{r})$ is given by:

$$\Phi^{\xi_{ik}}_{n_{ik}l_{ik}m_{ik}}(\vec{r}) = R^{\xi_{ik}}_{n_{ik}l_{ik}}(r) Y'_{l_{ik}m_{ik}}(\hat{r}) \tag{4.2}$$

with the radial part expressed as:

$$R^{\xi_{ik}}_{n_{ik}l_{ik}}(r) = r^{\,n_{ik}-1} e^{-\xi_{ik} r} \tag{4.3}$$

The accuracy of the single–center molecular orbitals employed in this work can be

assessed through structural investigations using electron momentum spectroscopy (EMS) in (e,2e) process, typically carried out in noncoplanar geometry at high impact energies (1–2 keV, see chapter 2). The theoretical framework of EMS is detailed in [12].

In EMS experiments, the reaction mechanism is simple enough that continuum particles can be described by plane waves, allowing the triple-differential cross section (TDCS) to be evaluated within the plane–wave impulse approximation (PWIA) [11, 16]. Previous EMS studies of $H_2O$ have validated the molecular orbitals used here [11]. Figure 4.1 shows theoretical TDCSs for the $1b_1$, $1b_2$, $2a_1$, and $3a_1$ orbitals in comparison with measurements at 1200 eV [17]. The ionization energies required for removing one electron from each molecular orbital of water are as follows: 32.2 eV($2a_1$), 18.5 eV($1b_2$), 14.7 eV($3a_1$), and 12.6 eV($1b_1$). The results demonstrate very good agreement, confirming that the adopted single-center molecular orbitals provide a reliable description of the target for dynamical studies (see chapter 2).

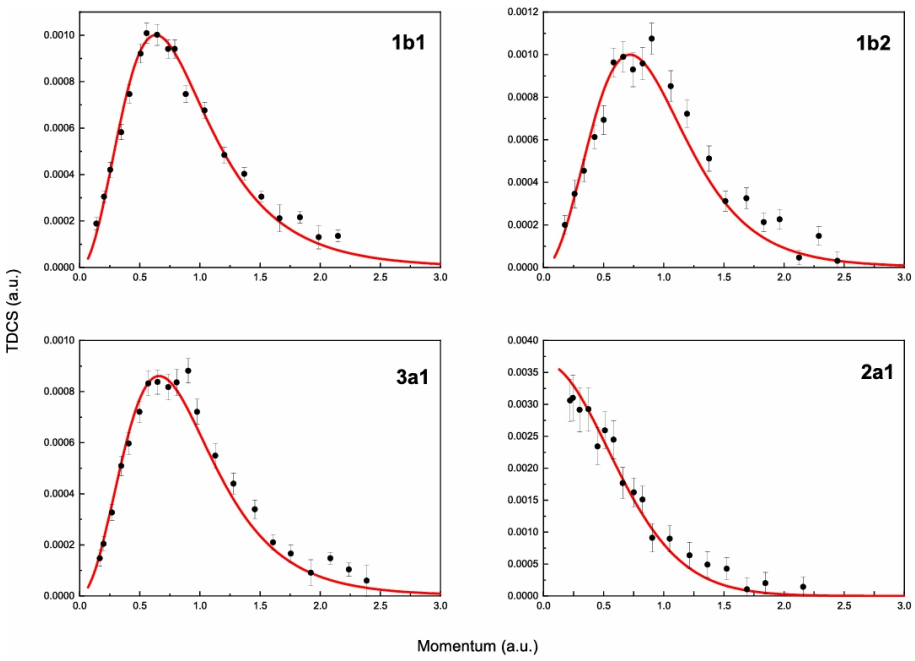


**Figure 4.1:** EMS momentum profile reported in a noncoplanar symmetric geometry at an impact energy of 1200 eV, as a function of the recoil momentum. The outgoing electrons are detected at 45°, sharing the same energy. Theoretical PWIA results (red solid line) are compared with experimental data (black solid circles) taken from [17]. The experimental results have been normalized to the theoretical result for optimal visual comparison.

For further validation, we compare this wave function with the older Moccia orbitals [18], which are constructed as expansions of Slater-type orbitals (STOs) combined with real spherical harmonics. These orbitals were obtained using the variational method to optimize the orbital parameters and coefficients in order to minimize the total molecular

energy, and have been extensively used in several studies involving both (e,2e) and (e,3e) processes [3, 9, 19, 20]. Table 4.1 reports ground state properties, including the bound length $d_{\mathrm{OH}}$, the angle $\alpha_{\mathrm{HOH}}$ , dipole moment$\mu$, and the ionization potential IP, computed with both sets of orbitals and compared to experiment [21–23]. The results clearly show that the present wave function yields a more accurate description, supporting its use in this work.

**Tableau 4.1:** Geometrical parameters as well as dipole moment $\mu$ and ionization potential (IP) of the equilibrium configuration of $H_2O$

| | $d_{\mathrm{OH}}$ (a.u.) | $\alpha_{\mathrm{HOH}}$ (deg.) | $\mu$ (a.u.) | IP (eV) |
|---|---|---|---|---|
| Moccia wave function [18] | 1.814 | 106.54 | 0.82 | 13.47 |
| Present wave function [11] | 1.812 | 104.3 | 0.731 | 12.9 |
| Exp. | 1.809 [21] | 104.5 [21] | 0.728 [22] | 12.6 [23] |

## 4.3 Laboratory Frame and Molecular Frame

It is important to note that the wavefunction describing the ground state of the water molecule in our work is defined in a coordinate system $(OXYZ)$ attached to the molecule. However, in the laboratory frame the wavefunction is defined in a fixed coordinate system $(Oxyz)$. Therefore, it is necessary to transform the molecular wavefunctions into the laboratory frame, which is done by applying the rotation operator according to the usual Euler angles $(\alpha, \beta, \gamma)$ [20].

A rotation about a point $O$ is a displacement of all points in space such that $O$ remains fixed. Let $(Oxyz)$ be a fixed right-handed trihedron and $(OXYZ)$ the trihedron obtained when the rotation $R(\alpha, \beta, \gamma)$ is applied to $(Oxyz)$. Let $(O, \mathbf{u})$ be an axis perpendicular to the plane $(O, z, Z)$ (see Figure 4.2). The Euler angles are defined as follows:

$$\alpha = (Oy, Ou), \quad \beta = (Oz, OZ), \quad \gamma = (Ou, OY).$$

The rotation $R(\alpha, \beta, \gamma)$ is the result of three successive rotations:

- rotation $R_z(\alpha)$ by an angle $\alpha$ around $Oz$ (bringing $Oy$ to $Ou$).
- rotation $R_u(\beta)$ by an angle $\beta$ around $Ou$ (bringing $Oz$ to $OZ$).
- rotation $R_Z(\gamma)$ by an angle $\gamma$ around $OZ$ (bringing $Ou$ to $OY$).

Thus, the rotation $R(\alpha, \beta, \gamma)$ [24] can be written as

$$R(\alpha, \beta, \gamma) = R_Z(\gamma) R_u(\beta) R_z(\alpha) \tag{4.4}$$

where

$$R_z(\alpha) = \begin{pmatrix} \cos\alpha & -\sin\alpha & 0 \\ \sin\alpha & \cos\alpha & 0 \\ 0 & 0 & 1 \end{pmatrix}; \quad R_u(\beta) = \begin{pmatrix} \cos\beta & 0 & \sin\beta \\ 0 & 1 & 0 \\ -\sin\beta & 0 & \cos\beta \end{pmatrix}; \quad R_Z(\gamma) = \begin{pmatrix} \cos\gamma & -\sin\gamma & 0 \\ \sin\gamma & \cos\gamma & 0 \\ 0 & 0 & 1 \end{pmatrix}$$

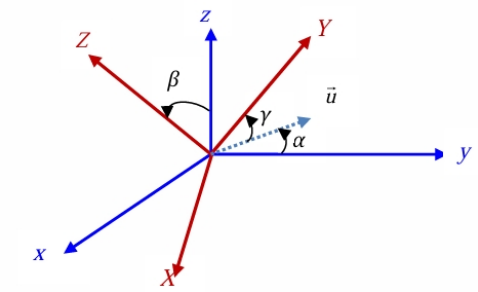


**Figure 4.2:** Representation of the Euler angles $(\alpha, \beta, \gamma)$ linking the laboratory frame $(Oxyz)$ to the molecular framE (OXYZ).

The wave function of the target molecule is expressed as a function of the Euler angles:

$$\phi_{i(\text{lab})}(\vec{r}, \alpha, \beta, \gamma) = \sum_{k=1}^{N_i} a_{ik} R^{\xi}_{n_{ik}}(r) \sum_{\mu=-l_{ik}}^{l_{ik}} D^{l_{ik}}_{\mu,m_{ik}}(\alpha, \beta, \gamma) Y_{l_{ik},\mu_{ik}}(\hat{r}) \tag{4.5}$$

where $D^{l_k}_{\mu,m_{ik}}(\alpha, \beta, \gamma)$ is the Wigner rotation matrix that rotates the molecular frame to the laboratory frame. The Wigner $D$-matrix is defined as:

$$D^{j}_{m',m}(\alpha, \beta, \gamma) = \left\langle j, m' \left| e^{-i\alpha J_z} \, e^{-i\beta J_y} \, e^{-i\gamma J_Z} \right| j, m \right\rangle \tag{4.6}$$

or in its explicit form:

$$D^{j}_{m',m}(\alpha, \beta, \gamma) = e^{-im'\alpha} \, d^{j}_{m',m}(\beta) \, e^{-im\gamma} \tag{4.7}$$

where $d^{j}_{m',m}(\beta)$ is the Wigner small $d$-matrix for rotation about the $y$-axis.

The indices $\mu$ and $m_{ik}$ are the projections of angular momentum in the molecular and laboratory frames, respectively.

The operators $J_y$ and $J_z$ are the components of the angular momentum operator $J$.

## 4.4 Projectile Charge Effects in Single Ionization of $H_2O$ Molecule by Positron and Electron impact

We consider the single ionization of $H_2O$ in its ground state by electron $e^-$ (or positron $e^+$) impact, which can be represented as:

$$e^-/e^+(E_i, \vec{k_i}) + \mathrm{H_2O} \longrightarrow \mathrm{H_2O^+} + e^-/e^+(E_s, \vec{k_s}) + e^-(E_1, \vec{k_1}), \tag{4.8}$$

where $\vec{k}_i(E_i)$ $\vec{k}_s(E_s)$, and $\vec{k}_1(E_1)$ denote the momenta (energies) of the incident projectile, the scattered projectile, and the ejected electron, respectively, as required by the conservation laws:

$$E_i = E_s + E_1 + I^+ \qquad \text{and} \qquad \vec{k}_i = \vec{k}_s + \vec{k}_1 + \vec{q}$$

$I^+$ and $\vec{q}$ denote, respectively, the ionization potential and the recoil momentum.

The momentum transfer to the target is defined as:

$$\vec{K} = \vec{k}_i - \vec{k}_s,$$

The magnitude and direction of the momentum transfer depend on the nature of the collision (see Chapter 2).

### 4.4.1 The M3CWZ model

For high incident energies, the ionization process can be reasonably described by the first Born approximation, provided that the interaction between the ejected electron and the residual ion is taken into account. One of the models developed under this framework is the BBK model, which includes post-collision interaction (PCI) and is generally used for such studies. Although the BBK model performs well in high to intermediat energy cases, it often fails at lower incident energies, as it neglects distortion effects and fails to consistently reproduce experimental results, particularly for molecular targets. More sophisticated approaches, such as the 3DW and M3DW models, improve accuracy by representing the projectile and ejected electrons with distorted waves and by accounting for molecular orientation effects. Yet, even these models may exhibit discrepancies for certain systems and require complex numerical procedures. In the present work, we propose the M3CWZ model, an approximate approach in which distortion is represented by Coulomb waves with a variable charge $Z(r)$.

The M3CWZ model was developed through the continued efforts of our research group.

The idea originated from enhancing the BBK model by introducing the variable charge approximation [7]. This modification laid the foundation for a series of theoretical developments that culminated in the formulation of the Three Coulomb Waves with a Variable Charge (3CWZ) model for atomic target, first proposed by our group for electron-impact ionization [25] and later extended to positron-impact ionization [26]. The approach was ultimately extended to molecular targets, leading to the establishment of the Molecular Three Coulomb Waves with a Variable Charge (M3CWZ) model [3, 8, 27].

#### 4.4.1.1 Approximation of Variable Charge

Distortion is a widely recognized concept underlying many advanced theoretical approaches [28]. This purely numerical method starts by solving the Schrödinger equation with a distortion potential (see chapter 1). In this work, distortion is approximated by Coulomb Waves with a Variable Charge $Z(r)$ [7].

The variable charge $Z(r)$ is evaluated using the spherically averaged potential $U_i$, which is given by:

$$U_i(r_1) = \frac{1}{4\pi}\int V_i(\vec{r}_1, \vec{R}_i)d\Omega_1 = -\frac{Z(r_1)}{r_1} \tag{4.9}$$

where $V_i(\vec{r}_1, \vec{R}_i)$ is the standard Hartree potential (or static potential), defined for molecules by:

$$V_i(\vec{r}_1, \vec{R}_i) = -\sum_{N=1}^{M}\frac{Z_N}{|\vec{r}_1 - \vec{R}_N|} + \sum_{j=1}^{N_0} N_{ij}\int \frac{|\varphi_j(\vec{r})|^2}{|\vec{r}_1 - \vec{r}|}\,d\vec{r} \tag{4.10}$$

$N_0$ is the number of occupied orbitals, $N_{ij}$ the number of electrons in the orbital, $M$ is the number of nuclei, $Z_N$ their charges and $\vec{R}_N$ their positions with respect to the molecular center of mass. $\varphi_j(\vec{r_j})$ are the molecular orbitals that describe the target. The variable charges used in the M3CWZ model are called $Z_i(r)$, $Z_s(r)$ and $Z_1(r)$ for the incident, scattered and ejected electron, respectively.

The calculation of matrix elements generally requires multicenter integrals, which makes the task quite complex. In the present work, we use single center molecular orbitals [11], as a result all calculations are performed with respect to one common center and the molecular problem is reduced to a quasi-atomic one. For the water molecule, the molecular orbitals are centred on the oxygen atom, and Eq. (4.10) becomes:

$$V_i(\vec{r}_1, \vec{R}_1, \vec{R}_2) = -\frac{8}{r_1} - \frac{1}{|\vec{r}_1 - \vec{R}_1|} - \frac{1}{|\vec{r}_1 - \vec{R}_2|} + \sum_{j=1}^{5} N_{ij}\int \frac{|\varphi_j(\vec{r})|^2}{|\vec{r}_1 - \vec{r}|}\,d\vec{r} \tag{4.11}$$

where $R_1 = R_2 = R = 1.812\ a.u.$, $R_1$ and $R_2$ represent the bond lengths.

After averaging over $d\Omega_1$, the spherically potential $U_i(r)$ given by Eq. 4.9, is written as:

$$U_i(r_1) = \frac{1}{4\pi}\int\left\{-\frac{8}{r_1} - 2\begin{cases}1/r_1 & \text{if } r_1 > R\\ 1/R & \text{if } r_1 < R\end{cases} + \sum_{j=1}^{5} N_{ij}\int\frac{|\varphi_j(\vec{r})|^2}{|\vec{r}-\vec{r}_i|}\,d\vec{r}\right\}d\Omega_1 \tag{4.12}$$

In the present study, since the molecular orbitals are centered on the oxygen atom, both the projectile and the ejected electron experience a charge $Z = 8$ at the molecular center (the oxygen nucleus). As the projectile (electron or positron) moves far from the target, it asymptotically experiences a charge $Z = 0$, while in the exit channel, the two outgoing electrons encounter a charge of $Z = 1$. As an example, Figure.4.3 shows the variable charges for ionization of the $2a_1$ orbital. It can be seen that the charges decrease from $Z = 8$ at $r = 0$ to their asymptotic values: $Z_s(r)$ and $Z_1(r)$ approach $Z = 1$ for the outgoing electrons, whereas $Z_i(r)$ approaches $Z = 0$ for the incident particle. These asymptotic values are reached rapidly, at a distance around $r_0 \approx 3$ a.u. Additionally, a pronounced peak is observed at $r = R$, where $R$ corresponds to the O–H bond length; this feature is not present in atomic targets.

To justify the use of the Coulomb wave model with a variable charge, we refer to the comparative analysis presented by Tamin [29], where the distorted wave function was compared with a spherical Coulomb wave of variable charge. The study demonstrated that the variable charge model reproduces the essential distortion effects with reasonable accuracy, particularly for higher angular momentum values, while significantly reducing computational cost. This supports the validity of using the Coulomb wave with a variable charge as an efficient and accurate approximation in our model.

#### 4.4.1.2 Calculation of The Triply Differential Cross Section (TDCS)

The Molecular Fully Differential Cross Section (FDCS) for the ionization of water molecule by electron and positron impact, for a particular orientation of the molecule and considering the ionization process as a pure electronic transition, is given by:

$$\sigma^{(4)}(\alpha,\beta,\gamma) = \frac{d^4\sigma}{d\Omega_{Euler}d\Omega_s d\Omega_1 dE_s} = (2\pi)^4\frac{k_s k_1}{k_i}\left(|T_{\text{dir}}|^2 + |T_{\text{exc}}|^2 + |T_{\text{dir}} - T_{\text{exc}}|^2\right) \tag{4.13}$$

$T_{\text{dir}}$ and $T_{\text{exc}}$ are the direct and exchange transition amplitudes respectively. For the positron impact ionization reaction, there is no exchange so that we take $T_{\text{exc}} = 0$, in Eq. (4.13).

In the frozen core and the single approximation picture [30], $T_{\text{dir}}$ and $T_{\text{exc}}$ are respec-

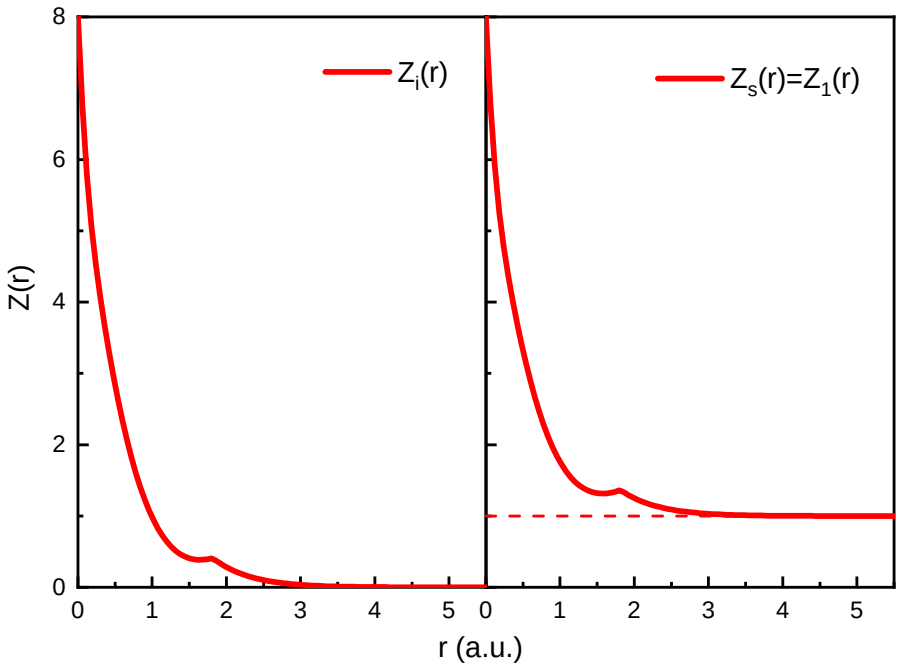


**Figure 4.3:** Variable charge Z(r) felt by (a) the incident electron and (b) the outgoing particles during the ionization process for the 2a1 molecular orbital of $H_2O$.

tively expressed as:

$$T_{\text{dir}} = \langle \phi_c^{Z(-)}(\vec{k}_s, \vec{r}_0)\, \phi_c^{Z(-)}(\vec{k}_1, \vec{r}_1)\, C(a_{01}, \vec{k}_{01}, \vec{r}_{01}) |V| \phi_c^{Z(+)}(\vec{k}_i, \vec{r}_0)\, \phi_{nlm}(\vec{r}_j) \rangle \tag{4.14}$$

and

$$T_{\text{exc}} = \langle \phi_c^{Z(-)}(\vec{k}_s, \vec{r}_1)\, \phi_c^{Z(-)}(\vec{k}_1, \vec{r}_0)\, C(a_{01}, \vec{k}_{01}, \vec{r}_{01}) |V| \phi_c^{Z(+)}(\vec{k}_i, \vec{r}_0)\, \phi_{nlm}(\vec{r}_j) \rangle \tag{4.15}$$

For the interaction potential $V$, we adopt the purely Coulomb form:

$$V = \frac{1}{r_{01}} - \frac{1}{r_0} \tag{4.16}$$

The functions $\phi_c^{Z(+)}$ and $\phi_c^{Z(-)}$ represent the incoming and outgoing Coulomb waves, respectively (see chapter 1), and are expressed as [31]:

$$\phi_c^{Z(+)}(\vec{k}, \vec{r}) = \frac{\exp(i\vec{k}\cdot\vec{r})}{(2\pi)^{3/2}}\, {}_1F_1\Big(i\alpha(r),\, 1,\, i(kr - \vec{k}\cdot\vec{r})\Big) \exp\left(\frac{\pi\alpha(r)}{2}\right) \Gamma(1 - i\alpha(r)) \tag{4.17}$$

and

$$\phi_c^{Z(-)}(\vec{k},\vec{r}) = \frac{\exp(i\vec{k}\cdot\vec{r})}{(2\pi)^{3/2}}\,{}_1F_1\Big(-i\alpha(r),\,1,\,-i(\vec{k}\cdot\vec{r}+kr)\Big)\exp\left(\frac{\pi\alpha(r)}{2}\right)\Gamma(1+i\alpha(r)) \quad (4.18)$$

The functions $\phi_c^{Z(+)}$ and $\phi_c^{Z(-)}$ represent Coulomb wave solutions corresponding to hydrogen-like systems characterized by an effective continuum charge $Z$. For single-ionization processes, this parameter is generally set to $Z = 1$. Within the framework of the M3CWZ model, instead of employing a fixed effective charge, we use a variable charge $Z(r)$ in Eqs. 4.17 and 4.18, which consequently modifies the Sommerfeld parameter into a spatially varying form, $\alpha(r)$.

The term $C(a_{01},\vec{k}_{01},\vec{r}_{01})$ represents the Coulomb interaction in the final state (PCI). It should be noted that the post-collision interaction (PCI) term in single ionization refers to the interaction between the scattered and ejected electrons, whereas in double ionization it corresponds to the interaction between the two ejected electrons (see chapter 3). It takes the form:

$$C(\alpha_{01},\vec{k}_{01},\vec{r}_{01}) = \exp\left(-\frac{\pi\alpha_{01}}{2}\right)\Gamma\left(1-i\alpha_{01}\right)\,{}_1F_1\left(-i\alpha_{01},1,-i(\vec{k}_{01}\cdot\vec{r}_{01}+k_{01}r_{01})\right) \quad (4.19)$$

For electron impact reaction, we have:

$$\alpha(r) = \frac{Z(r)}{k} \quad \text{and} \quad \alpha_{01} = \frac{1}{2k_{01}} \quad \text{where} \quad \vec{k}_{01} = \frac{1}{2}\left(\vec{k}_1 - \vec{k}_s\right)$$

${}_1F_1$ is a confluent hypergeometric function and $\Gamma$ is the gamma function.

For positrons, the potential will be $V = \frac{-1}{r_{01}} + \frac{1}{r_0}$ and $\alpha(r)$ and $\alpha_{01}$ given above for electrons are changed as follows:

$$\alpha(r) \to -\alpha(r) \quad \text{and} \quad \alpha_{01} \to -\alpha_{01}.$$

The initial bound state $\phi_{nlm}(\vec{r})$ has been introduced in the preceding section (see section 4.2).

Since molecular targets are randomly oriented in space, the expressions given in Eqs 4.14 and 4.15 must be averaged over the Euler angles. The triply differential cross section (TDCS) is therefore defined as:

$$\sigma^{(3)}_{\text{molecule}} = \frac{1}{8\pi^2}\int \sigma^{(4)}\, d\Omega_{\text{Euler}} \quad (4.20)$$

Within our theoretical approach, this integration is performed analytically [12] by

applying the following property of the rotation matrix:

$$\frac{1}{8\pi^2}\int d\Omega_{\text{Euler}} D^{l}_{\mu,m}(\alpha,\beta,\gamma) D^{l'*}_{\mu',m'}(\alpha,\beta,\gamma) = \frac{1}{2l+1}\delta_{ll'}\delta_{mm'}\delta_{\mu\mu'} \tag{4.21}$$

The TDCS is calculated by means of the M3CWZ model in which the continuum states are represented by Coulomb waves with variable charges, including the mutual interaction between the particles in the exit channel (positron–electron or electron–electron interactions). The evaluation of the matrix elements in the M3CWZ model involves the evaluation of a 6D integral, which is not an easy task because of the presence of the relative distance $r_{01} = |\vec{r}_0 - \vec{r}_1|$, approximations are generally used to simplify calculations.

Within our modelling, matrix 4.14 and 4.15 are evaluated by using a Fourier transform scheme, according to the method of Kornberg and Miraglia [32]. To this end, we use the Fourier transform definition:

$$\tilde{f}(\vec{p}) = \frac{1}{(2\pi)^{3/2}}\int e^{-i\vec{p}\cdot\vec{r}} f(\vec{r}) d\vec{r}, \quad f(\vec{r}) = \frac{1}{(2\pi)^{3/2}}\int e^{i\vec{p}\cdot\vec{r}} \tilde{f}(\vec{p}) d\vec{p} \tag{4.22}$$

so that we finally write the function $f(\vec{r})$ as follows:

$$f(\vec{r}) = \frac{1}{(2\pi)^3}\iint e^{i\vec{p}\cdot\vec{r}} e^{-i\vec{p}\cdot\vec{r}'} f(\vec{r}') d\vec{r}' d\vec{p} \tag{4.23}$$

As an example, let's consider the first term of Eq. 4.14:

$$I = \langle \varphi_c^{Z(-)}(\vec{k}_s,\vec{r}_0)\, \varphi_c^{Z(-)}(\vec{k}_1,\vec{r}_1)\, C(\alpha_{01},\vec{k}_{01},\vec{r}_{01})| \frac{1}{r_{01}} |\varphi_c^{Z(+)}(\vec{k}_i,\vec{r}_0)\, \Phi_{nlm}(\vec{r}_1)\rangle \tag{4.24}$$

By using Eq. 4.23, the matrix elements Eq. 4.24 is finally written in a more convenient form as follows:

$$I = \frac{1}{(2\pi)^3}\int I_1(\vec{p})\, I_2(\vec{p})\, I_3(\vec{p})\, d\vec{p} \tag{4.25}$$

where $I_1(\vec{p})$, $I_2(\vec{p})$ and $I_3(\vec{p})$ are, respectively, given by:

$$I_1(\vec{p}) = \int \phi_c^{Z*}(\vec{k}_1,\vec{r}_1)\, e^{-i\vec{p}\cdot\vec{r}_1}\, \Phi_{nlm}(\vec{r}_1)\, d\vec{r}_1 \tag{4.26}$$

$$I_2(\vec{p}) = \lim_{\lambda\to 0^+}\int \phi_c^{Z*}(\vec{k}_s,\vec{r}_0)\, e^{i\vec{p}\cdot\vec{r}_0}\, \varphi_c^{Z}(\vec{k}_i,\vec{r}_0) e^{-\lambda r_0}\, d\vec{r}_0 \tag{4.27}$$

$$I_3(\vec{p}) = \lim_{\beta\to 0^+}\int C^*(\alpha_{01},k_{s1},\vec{r}_{01})\, e^{-i\vec{p}\cdot\vec{r}_{01}}\, \frac{e^{-\beta r_{01}}}{r_{01}}\, d\vec{r}_{01} \tag{4.28}$$

where $\lambda$ and $\beta$ are two parameters approaching 0 (it was found that by taking $\lambda = \beta = 0.005$ we obtain a good compromise between the computer time and the accuracy).

We are able to express the quantities $I_1(\vec{p})$, $I_2(\vec{p})$ and $I_3(\vec{p})$ in a practically analytical form so that the matrix element given by Eq. 4.24 is reduced to simple three-dimensional numerical integrations, enabling a considerable economy of computing time. To check the accuracy of the method, comparison was made between results obtained within the method of Kornberg and Miraglia [32] with those within the method of Brauner et al. [6] for various targets (hydrogen atom, neon, argon and methane). When compared to the well-known sophisticated M3DW model, our theoretical approach allows a huge advantage in terms of computational time as one point in the TDCS is finally obtained in a few hours instead of a few days within the M3DW [33] model.

### 4.4.2 Results and discussion

We examine in this part how the projectile charge affects the triple differential cross sections (TDCS) by analyzing the ionization of the water molecule induced by both electron and positron impacts. Theoretical calculations were carried out using the M3CWZ model for incident energies of 250, 81, and 65 eV. The computed results are compared with available experimental measurements and other theoretical predictions. Initially, we focus on the experiments for electron impacts reported by Milne Brownlie et al. [34], conducted at 250 eV with a scattering angle of 15°; the corresponding TDCS results are displayed in Figures 4.4 and 4.5. The angular distributions of the TDCS are presented for the $1b_1$, $3a_1$, $1b_2$, and $2a_1$ molecular orbitals as a function of the ejection angle, setting the ejected electron energy to $E_2 = 10$ eV for all orbitals except for $3a_1$, where $E_2 = 8$ eV. The associated momentum transfer is approximately 1.11 a.u. As shown in Figure 4.4, the M3CWZ calculations for electron impact exhibit a double-peak structure in the binary region for the outer orbitals $1b_1$, $1b_2$, and $3a_1$, with a minimum near the direction of the momentum transfer $\vec{K}$, in agreement with the experimental data.

The observed double-peak structure is attributed to the dominant p-character of these orbitals, particularly in kinematic conditions close to the Bethe ridge regime, where the ejected electron absorbs most of the transferred energy. In the recoil region, the experimental data show a significant recoil peak for the $1b_2$ orbital, which is accurately captured by the M3CWZ calculations. For the $2a_1$ orbital, dominated by s-character, the M3CWZ model predicts a single peak in the binary region that aligns well with the experiments but fails to reproduce the pronounced recoil peak observed experimentally.

Examining the position-impact TDCSs, the overall shapes are similar to those for

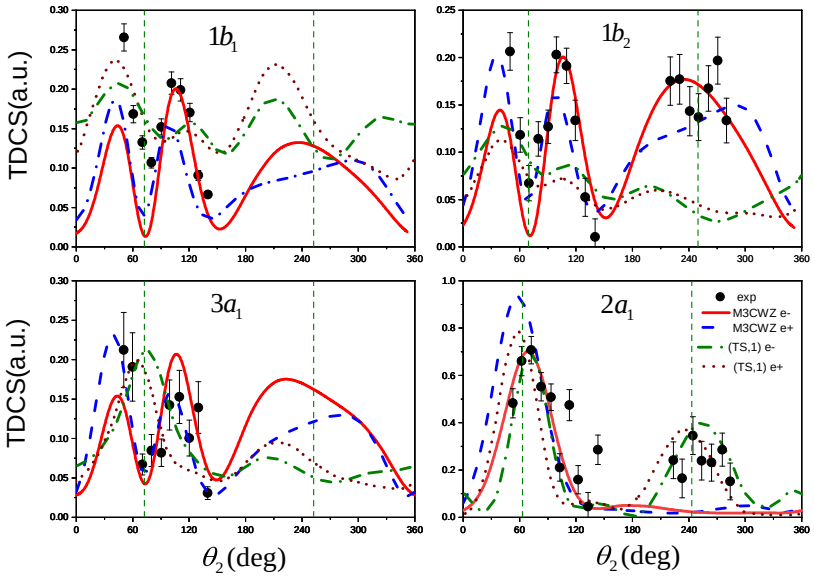


**Figure 4.4:** The triple differential cross section (TDCS) for ionization of the $1b_1$, $1b_2$, $2a_1$, and $3a_1$ molecular orbitals of $H_2O$ is presented for both positron and electron impact at a projectile energy of 250 eV. The projectile is scattered at a fixed angle of $\theta_1 = 15°$ and detected in coincidence with the ejected electron, which has an energy of $E_2 = 10$ eV for all orbitals except $3a_1$, where $E_2 = 8$ eV. Experimental electron-impact data (full circles) are taken from [34]. The M3CWZ theoretical predictions are shown as a red solid line for electrons and a blue dashed line for positrons. Results from the (TS,1) model [35] are plotted as a green dash-dot line for electrons and a wine-colored short-dash line for positrons. All experimental and theoretical results have been normalized to the M3CWZ data in the binary region. The dashed vertical lines mark the direction of the momentum transfer $\vec{K}$ and its opposite, $-\vec{K}$.

electron impact, although the magnitudes differ substantially. In the binary region, the first peak is more intense for positron impact than for electron impact (the second peak shows the opposite trend), while in the recoil region, the electron impact produces a stronger peak. Additionally, the peak positions are shifted: for electrons, the binary peaks are displaced toward the forward direction relative to the momentum transfer $\vec{K}$, while for positrons they shift backward; the recoil peaks exhibit the reverse behavior. These trends were previously predicted by DuBois and de Lucio [36] and recently confirmed for argon [37]. The differences between electron and positron impact TDCSs are attributed to post-collision interaction (PCI) effects in the exit channel. In the binary region, PCI enhances the probability of electron ejection for positron impact compared to electron impact. Conversely, in the recoil region, the residual ion elastically attracts the ejected electron, reducing its ejection probability. Peak position shifts are also interpreted in terms of PCI: in the binary region, the ejected electron is pulled backward for positron

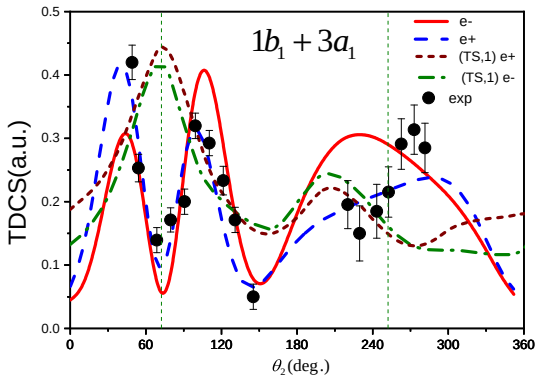


**Figure 4.5:** Same as 4.4 but for the summed TDCS ($1b_1 + 3a_1$) of $H_2O$

impact, whereas in the recoil region it is pulled forward. Figure 4.5 illustrates the TDCS for the combined ($1b_1$ + $3a_1$) orbital, demonstrating good agreement with experimental observations.

Overall, the M3CWZ model reproduces the angular distributions observed in (e,2e) experiments across all regions. The binary peak amplitudes are enhanced for positron impact, whereas in the recoil region, enhancement is observed for electron impact. The peak positions are consistent with the trends discussed in Figure 4.4. For instance, for the $2a_1$ orbital, the momentum transfer $\vec{K}$ is located at approximately 63.2°, while the binary peaks appear at 59° and 72° for positron and electron impact, respectively, illustrating the forward and backward shifts.

For a more comprehensive analysis, we perform a comparative study with the theoretical (TS,1) model [35], which is based on a full distorted-wave Born approximation (DWBA). In this approach, the distorted wave of the ejected electron is determined using an averaged nuclear field screened by the potential of the residual electrons. It is important to note that our results are presented on an absolute scale, whereas the (TS,1) results and experimental data have been normalized to our calculations in the binary region.

The first observation is that the (TS,1) model reproduces the angular distributions for the inner $2a_1$ orbital fairly well for electron impact, in contrast to M3CWZ, which fails to capture the recoil peak intensity accurately. For positron impact, the binary peak is shifted backward, while the recoil peak moves forward, in line with expectations. For the outer orbitals ($1b_1$, $3a_1$, and $1b_2$), however, M3CWZ provides a much better description. In particular, the (e,2e) data display a double-peak structure in the binary region, with the second peak being larger than the first for electron impact. (TS,1) fails to reproduce this feature, and the discrepancy is even more pronounced for the $3a_1$ orbital, where the binary double-peak structure is entirely absent. Additionally, for positron impact, the

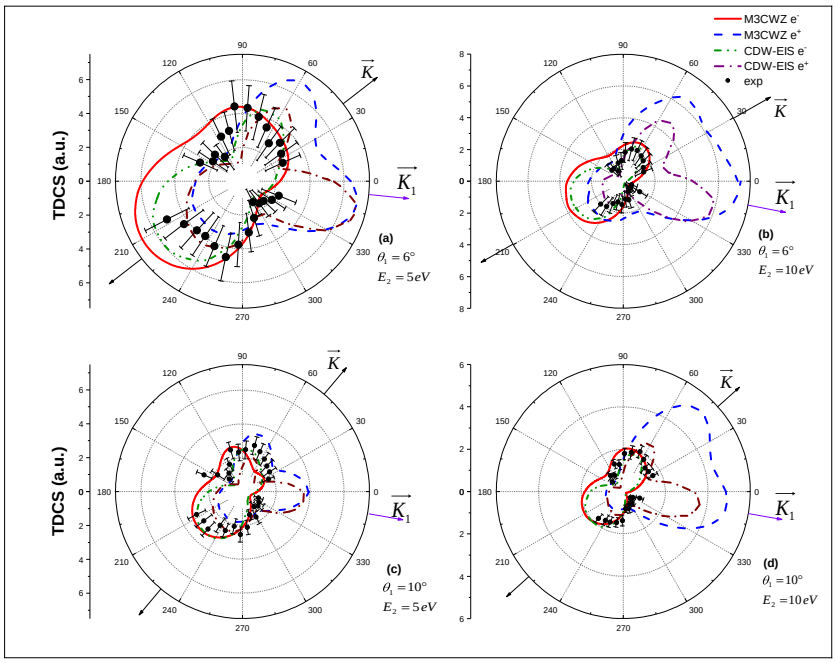


**Figure 4.6:** Polar plot of the summed TDCS for the ionization of the $1b_1$ and $3a_1$ orbitals of $H_2O$ by positron and electron impact at 81 eV impact energy as a function of the ejection angle $\theta_2$. The projectile is scattered at a fixed scattering angle $\theta_1 = 6°$ and detected in coincidence with the ejected electron having an energy $E_2 = 5$ eV (panel a) and $E_2 = 10$ eV (panel b). ALSO The projectile is scattered at a fixed scattering angle $\theta_1 = 10°$ and detected in coincidence with the ejected electron having an energy $E_2 = 5$ eV (panel c) and $E_2 = 10$ eV (panel d). The cross-normalized experimental data (see text) are black circles for electron impact taken from Ref. [37]. M3CWZ theoretical results are represented by a red solid line for electron impact and by a blue dashed line for positron impact. The green dash-dotted line and the wine dashed-dot line correspond to the CDW-EIS model [38] for electron impact and positron impact, respectively. The arrows indicate the directions of the momentum transfer $\vec{K}$ and the momentum of the scattered projectile $\vec{k}_1$.

recoil region peaks predicted by (TS,1) are overestimated compared to electron impact, which disagrees with experimental observations and theoretical expectations. Overall, M3CWZ is more effective in describing the ionization dynamics under these kinematics, except for the $2a_1$ orbital where the recoil peak remains inadequately reproduced.

We next consider a scenario with a projectile energy of 81 eV in four different kinematics: scattering angles of $\theta_1 = 6°$ and $10°$ and ejected electron energies of $E_2 = 5$ and 10 eV. The TDCSs are reported for the combined ($1b_1$ + $3a_1$) orbitals, because the $1b_1$ and $3a_1$ orbitals are not resolved as highlighted above at 250 eV impact energy, this limitation is a common experimental challenge faced by molecular targets. This investigation employs the M3CWZ model, and the results are compared with recent experimental measurements [37] as well as with theoretical predictions from the sophisticated CDW-EIS model [38]. The CDW-EIS model is a fully distorted-wave approach in which the

projectile-target interaction is described using eikonal functions. In this framework, the projectile differentiates between the Coulomb fields of the target ion and the active electron as it approaches the target. It is worth noting that the current experiments were conducted using a COLTRIMS reaction microscope (C-REMI) [39], a technique that provides high-efficiency measurements. The experimental data are cross-normalized to establish an absolute scale, applying a common factor to align theory and experiment. In this study, the global normalization factor was determined by fitting the data to our M3CWZ results for $\theta_1 = 10^\circ$ and $E_2 = 10$ eV, yielding a scaling factor of 3.09, which was then applied across all other kinematics.

The present kinematics correspond to dipole-dominated regimes, where a recoil peak is observed in all cases. In these conditions, the ejected electron experiences elastic scattering from the residual ion and backscatters opposite to the momentum transfer direction, producing a recoil peak. Figure 4.6 (panels a and b) presents TDCS results for a scattering angle of $\theta_1 = 6^\circ$ and ejection energies $E_2 = 5$ eV and $E_2 = 10$ eV, corresponding to momentum transfers of 0.39 and 0.47 a.u., respectively. For clarity, the results are shown in polar plots to facilitate visual comparison with previous CDW-EIS results by Acebal and Otranto [38]. Numerical TDCSs calculated with both M3CWZ and CDW-EIS models are presented for electron and positron impact, alongside experimental electron-impact data [37]. All theoretical results are provided on an absolute scale, while the experimental data are cross-normalized as described above. For electron impact, the data exhibit a pronounced recoil peak in both kinematic cases, which is generally well reproduced by M3CWZ. However, M3CWZ slightly overestimates the recoil intensity in the ejection angle range of approximately 210°–255°. Comparison with CDW-EIS shows that both models produce similar TDCS shapes for electron impact, though M3CWZ predicts a somewhat broader binary peak at 5 eV (panel a). The agreement between M3CWZ and CDW-EIS improves at 10 eV (panel b), although CDW-EIS reproduces the recoil region slightly more accurately.

For positron impact, both theoretical models predict a double-peak structure in the binary region, with higher intensities compared to electron impact. In the recoil region, a single peak is observed in both models, though the intensities are lower than for electron impact. These trends are consistent with the theoretical predictions discussed previously for the 250 eV impact energy kinematics, confirming the reliability of the models across different energies.

Considering the kinematics shown in Figure 4.6 (panels c and d) for a scattering angle of $\theta_1 = 10^\circ$ and the same ejection energies, similar overall trends are observed. Both theoretical models exhibit reasonable agreement with the electron-impact experimental data. For positron impact, two prominent peaks appear in the binary region, while

for electron impact at $E_2 = 5$ eV (panel c), M3CWZ predicts a double-peak structure in the binary region. This feature is attributed to kinematics close to the Bethe ridge regime, where the momentum transferred to the target is nearly fully absorbed by the ejected electron. Indeed, at $\theta_1 = 10°$ and $E_2 = 5$ eV, the momentum transfer $K$ and the momentum of the ejected electron $k_2$ are comparable ($k_1 = 0.51$ and $k_2 = 0.61$ a.u.). It is worth noting that, under these conditions, the CDW-EIS model does not reproduce the double-peak structure observed in M3CWZ for electron impact.

For positron impact, the binary region consistently displays a double-peak structure, while a single recoil peak is predicted by both theoretical models. The amplitudes of the binary peaks increase with both ejection energy and momentum transfer, whereas the recoil region exhibits the opposite trend. The positions of the peaks in the binary region for positron impact also deserve attention. As previously predicted by the CDW-EIS model [38], the first binary peak is located near the momentum transfer direction $\vec{K}$, while the second aligns with the scattered projectile momentum $\vec{k_1}$ (approximately $\theta_1 = 6°$ in Figure 4.6 (panels a and b) and $\theta_1 = 10°$ in Figure 4.6(panels c and d)). This behavior is not observed for electron impact, as the ejected electron is repelled by the projectile. The observed trends for positron impact are explained by post-collision interactions, which attract the ejected electron along $\vec{k_1}$, enhancing ejection in this direction, in agreement with prior CDW-EIS predictions [38].

The study is further extended to lower incident energies. Recent COLTRIMS experiments at 65 eV provide absolute TDCS data [4], allowing comparison with our theoretical predictions. Previous investigations using Moccia's wave function showed good agreement for electron impact [3]. In the present work, we focus on two kinematic conditions within the M3CWZ framework, where the target is described using the updated wave function introduced in [11], considering a scattering angle $\theta_1 = 10°$ and ejection energies $E_2 = 5$ and 10 eV within the scattering plane. The primary objective of this study is to investigate in detail the ionization process by electron and positron impact, aiming to elucidate the influence of the projectile charge on the TDCS at these lower incident energies. In Figure 4.7, the summed TDCS for the combined ($1b_1 + 3a_1$) orbitals is presented as a function of the ejection angle for a scattering angle of $\theta_1 = 10°$ and ejection energies $E_2 = 5$ eV (panel a) and $E_2 = 10$ eV (panel b), for both positron and electron impact. Also included are the experimental measurements and M3DW theoretical results for electron impact. The experimental data display a single peak in both regions, with the recoil peak notably more pronounced for both ejection energies. M3CWZ predictions for electron impact show good agreement with the absolute measurements, accurately reproducing both the shape and magnitude of the TDCS. Comparison with the more sophisticated M3DW model indicates even better agreement in the binary region, although discrepancies re-

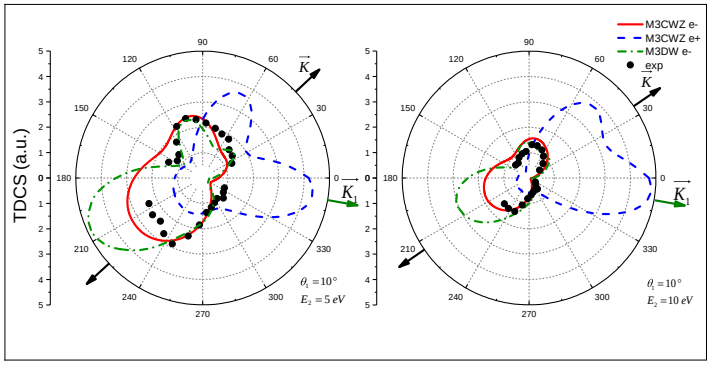


**Figure 4.7:** Polar plot of the absolute summed TDCS for the ionization of the $1b_1$ and $3a_1$ orbitals of $H_2O$ by positron and electron impact at a projectile energy of 65 eV, as a function of the ejection angle $\theta_2$. The projectile is scattered at a fixed angle $\theta_1 = 10°$ and detected in coincidence with the ejected electron ($E_2 = 5$ eV in panel a, $E_2 = 10$ eV in panel b). Absolute experimental data for electron impact (black circles) are taken from [4]. M3CWZ theoretical results are shown as a red solid line for electrons and a blue dashed line for positrons. Results from the M3DW model [4] for electron impact are shown as a green dash-dotted line. Arrows indicate the directions of the momentum transfer $\vec{K}$ and scattered projectile momentum $\vec{k}_1$.

main in the recoil region. For positron impact, a double-peak structure is evident in the binary region, while a single, less pronounced peak appears in the recoil region for both ejection energies. The binary peak magnitudes exceed those for electron impact, whereas the opposite trend is observed in the recoil region. The positions of the peaks for positron impact are consistent with prior observations: the first peak aligns approximately with the momentum transfer $\vec{K}$, and the second with the scattered projectile momentum $\vec{k}_1$. These features, already discussed at 81 eV impact energy, are directly associated with post-collision interaction (PCI), which is incorporated in the M3CWZ calculations. Notably, to our knowledge, no theoretical results for positron impact are available at these kinematics. It should also be noted that the distinctive positron-impact features observed at lower energies (65 and 81 eV) are not present at the higher intermediate energy of 250 eV.

Finally, we discuss the strengths and limitations of the M3CWZ model. The method approximates distortion effects using a variable charge $Z(r)$, rather than solving the full second-order differential equation for a true distorted wave. However, PCI is treated exactly within M3CWZ, allowing the model to be applied even at low impact energies, as demonstrated here for $E_i = 65$ eV. The computational efficiency of M3CWZ is also an advantage, providing a single TDCS point within a few hours compared to several

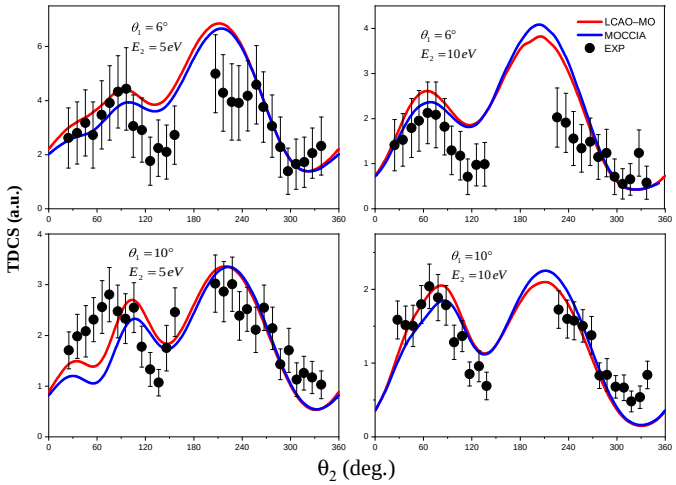


**Figure 4.8:** Summed TDCS for the ionization of the $1b_1$ and $3a_1$ orbitals of $H_2O$ as a function of the ejection angle at 81 eV in coplanar asymmetric geometry. The projectile is scattered at $\theta_1 = 6°$ or $10°$ in coincidence with the ejected electron ($E_2 = 5$ or 10 eV). Theoretical results are shown as a red solid line (M3CWZ with new MO) and a blue dashed line (M3CWZ with Moccia MO). Cross-normalized experimental data (black circles) are from [37].

days required by other models. The results indicate that the model accurately reproduces the TDCS for the outermost orbitals of $H_2O$ but fails to fully capture the intensity distribution in the recoil region for the inner $2a_1$ orbital. This limitation likely arises from the single-electron approximation, which treats inner electrons as part of a frozen core, excluding their contribution to the reaction. Extending the model to include these electrons would significantly increase computational demands. An alternative approach would be to describe the ejected electron with a true distorted wave rather than a Coulomb wave with variable charge.

We now perform a comparative analysis between the molecular orbitals employed in the present work and those of Moccia [18] to assess their impact on the computed TDCSs. For this purpose, we focus on the same kinematics considered above at projectile energies of 81 eV and 65 eV in coplanar asymmetric geometries, with the corresponding results shown in Figures 4.8 and 4.9. In Figure 4.8, experimental measurements at 81 eV impact energy [37] are presented for scattering angles of $\theta_1 = 6°$ and $10°$ and ejection energies of $E_2 = 5$ and 10 eV; the data are cross-normalized as previously described for Figure 4.6. Overall, both sets of molecular orbitals produceangular distributions that are very similar in shape and magnitude, and both reproduce the experimental trends comparably well. A slight enhancement in the binary-region intensity is observed when using the new molecular orbitals, although this difference is minor, indicating that neither set of bound states significantly affects the TDCS calculations. Figure 4.9 presents the TDCSs calculated

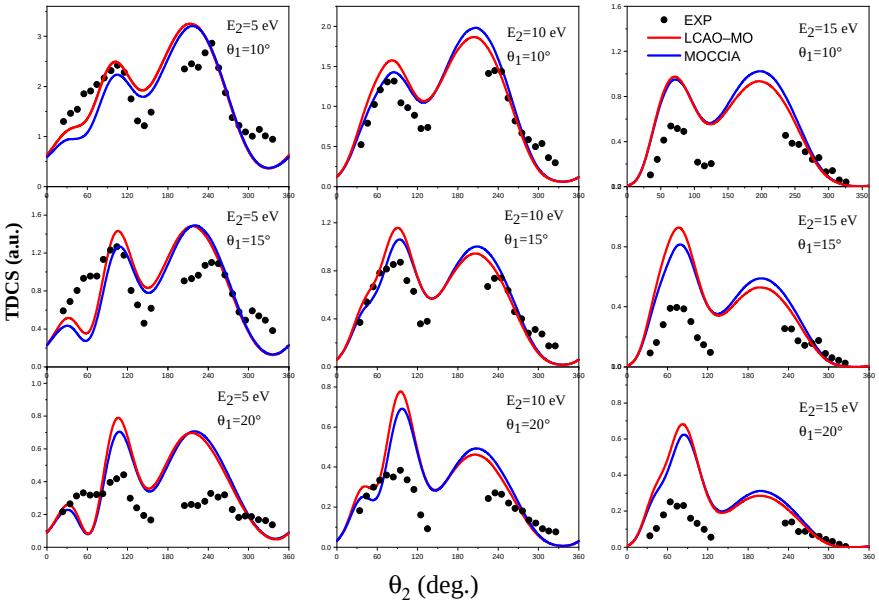


**Figure 4.9:** Summed TDCS for the ionization of the $1b_1$ and $3a_1$ orbitals of $H_2O$ as a function of the ejection angle at 65 eV in coplanar asymmetric geometry. The projectile is scattered at $\theta_1 = 10°$, 15°, or 20° in coincidence with the ejected electron ($E_2 = 5$, 10, or 15 eV). Theoretical results are shown as a red solid line (M3CWZ with new MO) and a blue dashed line (M3CWZ with Moccia MO). Absolute experimental data (black circles) are from [4].

with M3CWZ compared to absolute measurements [4] at 65 eV for three scattering angles ($\theta_1 = 10°$, 15°, and 20°) and three ejection energies ($E_2 = 5$, 10, and 15 eV). The trends observed are consistent with those shown in Figure 4.8, with the binary peak slightly enhanced for the new molecular orbitals. This indicates that the TDCS predictions within the M3CWZ model are largely insensitive to the choice of molecular orbitals, whether Moccia's [18] or the new orbitals employed here. Differences between these bound states are mainly reflected in the molecular properties of $H_2O$, where the new orbitals provide improved agreement with experimental data (Table 4.1).

## 4.5 Influence of the Initial-State Wavefunction on the (e,3e) Differential Cross Sections of $H_2O$ at a Fixed Molecular Orientation

We consider the double ionization of $H_2O$ in its ground state by electron impact, which can be schematically represented as:

$$e^-(E_i,\vec{k}_i) + \mathrm{H_2O} \longrightarrow \mathrm{H_2O^{++}} + e^-(E_s,\vec{k}_s) + e^-(E_1,\vec{k}_1) + e^-(E_2,\vec{k}_2), \tag{4.29}$$

where $\vec{k}_i(E_i)$, $\vec{k}_s(E_s)$, $\vec{k}_1(E_1)$ $\vec{k}_2(E_2)$ denote the momenta (energies) of the incident projectile, the scattered projectile, first ejected and second ejected electrons respectively. For an $(e,3e)$ reaction, energy conservation requires:

$$E_i = E_s + E_1 + E_2 + I^{++} \qquad \text{and} \qquad \vec{k}_i = \vec{k}_s + \vec{k}_1 + \vec{k}_2 + \vec{q}$$

$I^{++}$ and $\vec{q}$ are respectively the ionization potential and the recoil momentum.

It should be noted that in the case of double ionization of multicentric targets, the two ejected electrons may originate from the same molecular orbital or from two different molecular orbital. In the present work, we consider the double ionization of single-oriented water by electron impact, where both electrons are ejected from the same molecular orbital (see table 4.2 taken from [20]).

**Tableau 4.2:** Double ionization energies $I^{++}$ (eV) for the various states of the water molecule.

| Molecular orbitals | Theoretical data | Experimental data |
|---|---|---|
| $1b_1^{-2}$ | 39.7 | 41.3 |
| $3a_1^{-2}$ | 44.4 | 46.1 |
| $1b_2^{-2}$ | 52.2 | 53.2 |
| $2a_1^{-2}$ | 83.3 | 82.2 |

### 4.5.1 Description of the initial state

In this work, we focus on the double ionization of the four orbitals of $H_2O$ ($1b_1$, $1b_2$, $2a_1$, and $3a_1$) in its ground state as in the SI part. The initial state of the collisional system is represented as the product of a plane wave, describing the incident electron, and the wavefunction of the $H_2O$ molecule:

$$\Psi_i = e^{i\vec{k}_i\cdot\vec{r}_0}\,\phi_{ij}(\vec{r}_1,\vec{r}_2,\ldots,\vec{r}_{10}) \tag{4.30}$$

We adopt the description of Hafied et al. [11] for the wavefunctions of the initial state of the water molecule $\phi_{ij}(\vec{r}_1, \vec{r}_2, \ldots, \vec{r}_{10})$ (Section 4.2). It should be noted that the exchange effects between the incident electron and the ejected electrons is neglected, since the incident and scattered electrons move much faster than the ejected ones.

### 4.5.2 Description of the final state

In the final state of the ollisional system, three electrons are emitted. In the full six-Coulomb-wave (6C) model, each electron interacts with the residual ion and with the other two electrons, leading to extremely high-dimensional integrations for molecular targets (see chapter 3). In the first Born approximation, the scattered electron is treated as a plane wave, while the two ejected electrons are described by Coulomb waves interacting only with the residual ion [40]. In this work, we employ the 2CWG models; the formalism and computational approach were already presented in Chapter 3 for atomic double ionization, and here we extend it to the molecular case, where the main modification concerns the calculation of the differential cross section. The final state is given by

$$\Psi_f = e^{i\vec{k}_s\cdot\vec{r}_0}\,\Phi_{ij}(\vec{k}_1, \vec{k}_2, \vec{r}_1, \ldots, \vec{r}_{10})\varphi_G(k_{12}) \tag{4.31}$$

Where $\Phi_{ij}(\vec{k}_1, \vec{k}_2, \vec{r}_1, \ldots, \vec{r}_{10})$ is the wave function for the double continuum state of the water molecule.

### 4.5.3 Six-Fold Differential Cross Section

Within the first Born approximation, the six-fold differential cross section (6DCS) for a given molecular orientation defined by the Euler angles $(\alpha, \beta, \gamma)$, is expressed as:

$$\sigma^{(6)}(\alpha, \beta, \gamma) = \frac{d^6\sigma}{d\Omega_{\text{Euler}}\, d\Omega_1\, d\Omega_2\, d\Omega_s\, dE_1\, dE_2} = \frac{k_1 k_2 k_s}{k_i}\left|f_{B1}\right|^2 \tag{4.32}$$

where $d\Omega_{\text{Euler}} = \sin\beta\, d\beta\, d\alpha\, d\gamma$, $d\Omega_s$, $d\Omega_1$, and $d\Omega_2$ are the solid angle elements of the scattered and two ejected electrons, and $dE_1$ and $dE_2$ denote the energy intervals of the ejected electrons.

The scattering amplitude, which depends on the target orientation, is expressed for the process as:

$$f_{B1} = -\frac{1}{2\pi}\langle\Psi_f|V|\Psi_i\rangle \tag{4.33}$$

where $|\Psi_i\rangle$ denotes the wavefunction of the initial state of the system, $|\Psi_f\rangle$ corresponds to the final state, and $V$ represents the interaction between the incident electron and the

target and is written as

$$V = -\frac{8}{r_0} - \frac{1}{|\vec{r}_0 - \vec{R}_1|} - \frac{1}{|\vec{r}_0 - \vec{R}_2|} + \sum_{i=1}^{10} \frac{1}{r_{0i}} \tag{4.34}$$

where $R_1 = R_2 = R_{\mathrm{OH}} = 1.812$ a.u., $r_i$ is the position vector of the $i$-th bound electron relative to the oxygen nucleus, $r_0$ is the coordinate of the incident electron, and $r_{0i} = |\vec{r}_0 - \vec{r}_i|$.

Furthermore, the reduction of this ten-electron target problem to a two-electron system is carried out within the frozen-core approximation [30, 41]. Therefore, the scattering amplitude simplifies to (see Chapter 3):

$$f_{B1} = \frac{-2\sqrt{2}}{K^2} \left\langle \varphi(\vec{k}_1, \vec{r}_1)\varphi(\vec{k}_2, \vec{r}_2) \left| e^{i\vec{K}\cdot\vec{r}_1} + e^{i\vec{K}\cdot\vec{r}_2} - 2 \right| \phi_{ij}(\vec{r}_1, \vec{r}_2) \right\rangle \varphi_G(k_{12}) \tag{4.35}$$

with $\vec{K} = \vec{k}_i - \vec{k}_s$ being the momentum transfer.

### 4.5.4 Results

In this section, we study the variation of the sixfold differential cross sections as a function of the ejection directions for the ionization of the four outer molecular orbitals of an oriented water molecule, referred to as $1b_1$, $3a_1$, $1b_2$, and $2a_1$ by electron impact using single–center molecular orbitals [11], at both low and high incident energies, for three particular orientations. These orientations are defined by the Euler angle triplets $(0, 0, 0)$, $(0, \pi/2, 0)$, and $(0, \pi/2, \pi/2)$, as previously used by Champion et al. [9] and Dal Cappello et al. [10] in their studies on the double ionization of the water molecule, employing the molecular orbitals of Moccia [18].

In this context, the first configuration corresponds to a water molecule located in the $yz$ plane with its bisector along the $z$-axis, whereas the second and third configurations correspond to a water molecule lying, respectively, in the $xy$ and $xz$ planes, with its bisector along the $x$-axis. Note that, in all cases, the incident momentum $\vec{k_i}$ is collinear with the $z$-axis (see Table 4.3 [9]).

Furthermore, we consider the kinematic conditions reported in Refs. [9, 10], where $E_1 = E_2 = 10$ eV, $\theta_s = 0°$, and the scattered electron energy is $E_s = 250$ eV for the low energy case, while the incident electron energy is $E_i = 1000$ eV for the high energy case.

**Tableau 4.3:** Schematic representation of the three particular water molecule orientations: $(0, 0, 0)$, $(0, \pi/2, 0)$, and $(0, \pi/2, \pi/2)$.

| | | |
|---|---|---|
| 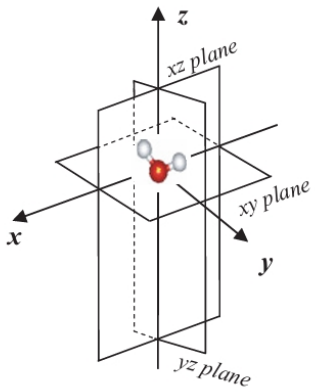 | 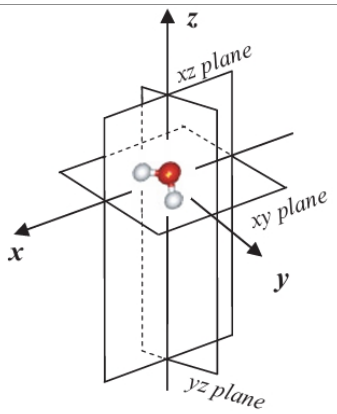 | 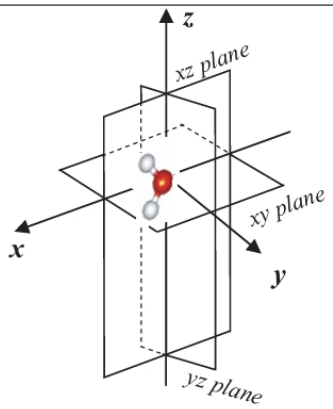 |
| $(\alpha, \beta, \gamma) = (0, 0, 0)$<br>$H_2O$ in the $yz$ plane | $(\alpha, \beta, \gamma) = (0, \pi/2, 0)$<br>$H_2O$ in the $xy$ plane | $(\alpha, \beta, \gamma) = (0, \pi/2, \pi/2)$<br>$H_2O$ in the $xz$ plane |

### 4.5.5 Low Impact Energy ($E_s = 250$ eV)

In Figure 4.10, we first examine the case $(\alpha, \beta, \gamma) = (0, 0, 0)$, and we analyze the 6DCSs for an (e,3e) experiment as a function of the ejected angles $\theta_1$ and $\theta_2$ in a coplanar geometry ($\varphi_s = \varphi_1 = \varphi_2 = 0°$). The ejected electron energies are $E_1 = E_2 = 10$ eV, and the scattered polar angle is $\theta_s = 0°$.

In Figure 4.10 (a), we first report the results obtained for the $1b_1$ molecular orbital. We clearly observe four hills: a first one extending from $\theta_1 = 77°$ to $\theta_1 = 151°$ (with $\theta_2$ ranging from $\theta_2 = 207°$ to $\theta_2 = 281°$), and a second one (with a less pronounced maximum) extending from $\theta_1 = 18°$ to $\theta_1 = 140°$ (with $\theta_2$ ranging from $\theta_2 = 220°$ to $\theta_2 = 340°$), the two other hills being simply obtained by symmetry. We find results close to those already reported by Dal Cappello et al. [10] for oriented $1b_1$ water orbital in the direction $(0, 0, 0)$ and for the same kinematic conditions. Thus, these four hills may be classified into two groups of maxima characterized by $|\theta_1 - \theta_2| \approx 120°$ and $|\theta_1 - \theta_2| \approx 240°$, respectively, identifying the signature of the two-step1 (TS1) mechanism, in which an incoming electron collides with a target electron that is first ejected along the direction of the momentum transfer or in the opposite direction, symmetrically. In a second step, this first ejected electron collides with a second target electron and ejects it during a quasi-elastic" collision characterized by a strong electrostatic repulsion, leading to a $|\theta_1 - \theta_2|$ angle greater than $90°$.

Considering now Figure 4.10 (b), which presents the predicted 6DCSs for the $2a_1$ orbital, we observe both SO and TS1 mechanisms. The maxima are not localized at a single angle but appear as lobes extending from 150° to 220°, centered around 180°. This

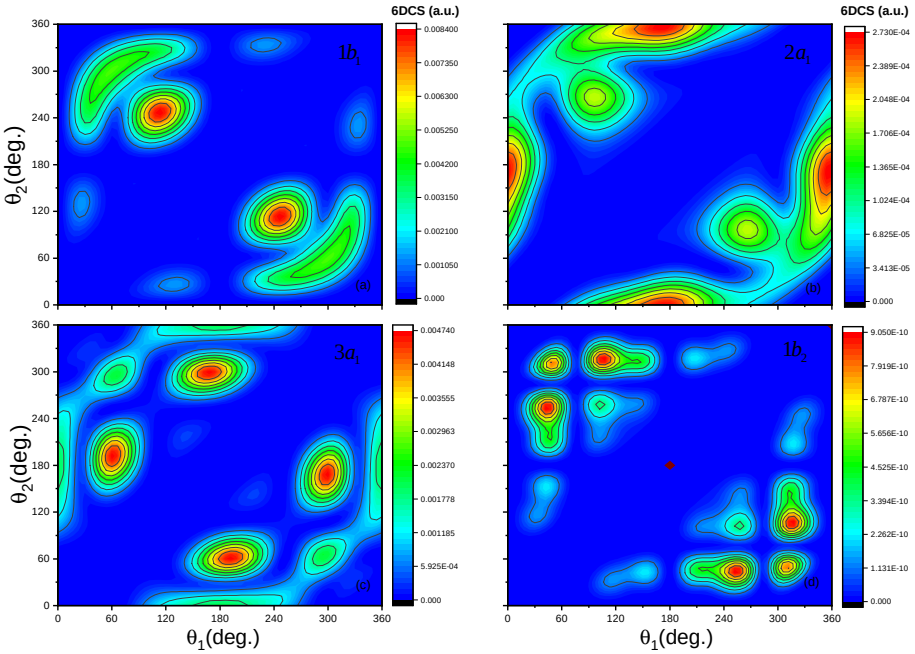


**Figure 4.10:** (Color online) Sixfold differential cross sections (expressed in (a.u.) for the double ionization of the water molecule oriented in the direction $(\alpha, \beta, \gamma) = (0, 0, 0)$ for $\theta_s = 0°$. The ejected energies are $E_1 = E_2 = 10$ eV and $E_s = 250$ eV. (a) $1b_1$ orbital; (b) $2a_1$ orbital; (c) $3a_1$ orbital; and (d) $1b_2$ orbital.

indicates the presence of SO–TS1 interferences.

Figure 4.10 (c) shows the results for the $3a_1$ molecular orbital. Once again, the TS1 features are evident, particularly for $|\theta_1 - \theta_2| \approx 130°$, leading to forward scattering with maxima at $(\theta_1, \theta_2) = (60°, 190°)$ and backward scattering with maxima at $(\theta_1, \theta_2) = (168°, 298°)$, along with two other symmetric hills.

For the $1b_2$ molecular state, Figure 4.10 (d) , shows that the 6DCS is very small (on the order of $10^{-10}$). This result is consistent with those reported by Champion et al. [9] and Dal Cappello et al. [10].

When rotations of the molecular target are applied, corresponding to $(\alpha, \beta, \gamma) = (0, \pi/2, 0)$ and $(\alpha, \beta, \gamma) = (0, \pi/2, \pi/2)$ (see Figures 4.11 and 4.12, respectively), we obtain the following rules [9], which are consistent with the observations reported by Champion et al. [9].

$$D_0(0, \pi/2, 0): \quad \begin{cases} P_X \to P_Z, \\ P_Y \to P_Y, \\ P_Z \to P_X, \end{cases}$$

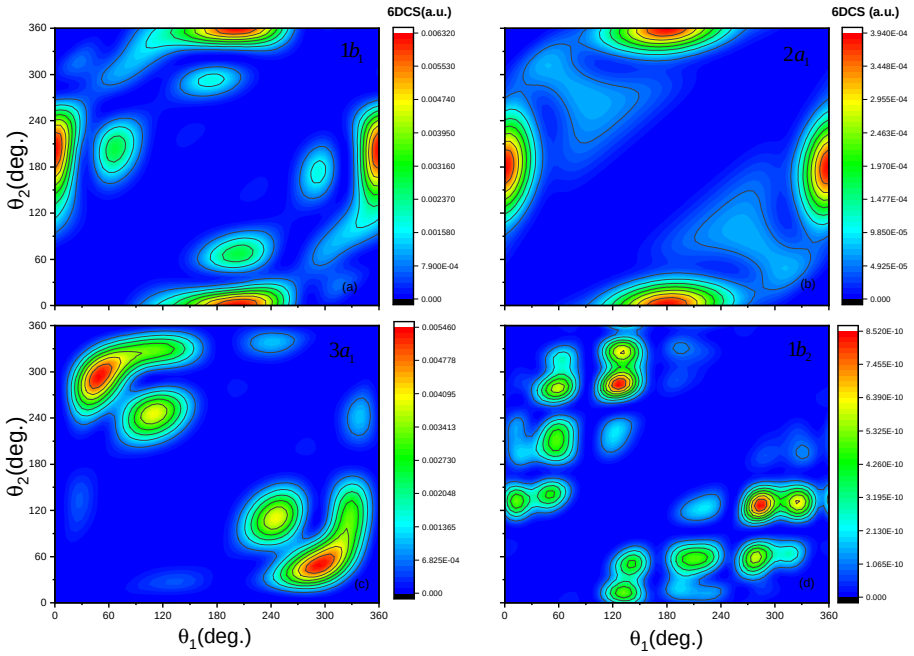


**Figure 4.11:** Same as Figure 4.10, but for $(\alpha, \beta, \gamma) = (0, \pi/2, 0)$. (a) $1b_1$ orbital; (b) $2a_1$ orbital; (c) $3a_1$ orbital; and (d) $1b_2$ orbital.

$$D_0(0, \pi/2, \pi/2): \quad \begin{cases} P_X \rightarrow P_Y, \\ P_Y \rightarrow P_Z, \\ P_Z \rightarrow P_X. \end{cases}$$

Thus, for example, in the case $(\alpha, \beta, \gamma) = (0, \pi/2, 0)$, the $3a_1$ molecular orbital, originally dominated by a $P_Z$ atomic component, displays an overall "$P_X$"-like behavior [Figure 4.11(c)] and exhibits a TS1 feature, closely resembling that previously identified for the $1b_1$ molecular orbital( Figure 4.10(a)). For the $1b_1$ and $2a_1$ orbitals (Figures 4.11(a) and 4.11(b), respectively), which are primarily characterized by $P_X$ and $s$ atomic components, the double ionization mechanisms are clearly manifested. This indicates that the SO mechanism plays a significant role.

It should be noted that for the $1b_2$ molecular state in the configuration $(\alpha, \beta, \gamma) = (0, \pi/2, 0)$, the 6DCSs are very small (on the order of $10^{-10}$), while for the $1b_1$ state in the configuration $(\alpha, \beta, \gamma) = (0, \pi/2, \pi/2)$, the 6DCSs are negligible (on the order of $10^{-15}$). These results are also consistent with those reported by Champion *et al.* [9] and Dal Cappello *et al.* [10].

To further evaluate the reliability of the theoretical description, a comparative analysis is carried out between the molecular orbitals employed in the present work and those of

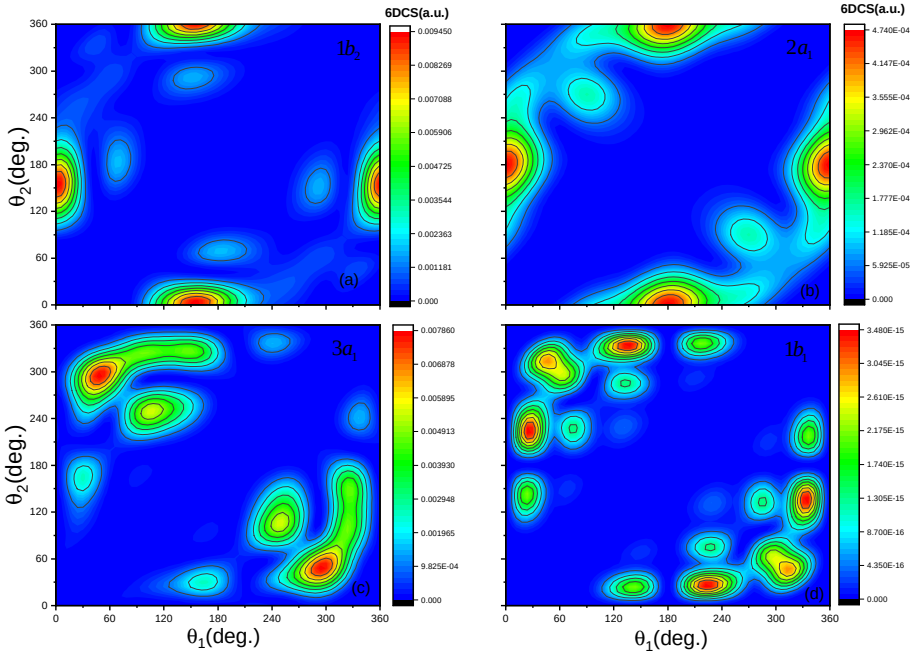


**Figure 4.12:** Same as Figure 4.10, but for $(\alpha, \beta, \gamma) = (0, \pi/2, \pi/2)$. a)$1b_2$ orbital; b)$2a_1$ orbital; c) $3a_1$ orbital; and (d) $1b_1$ orbital.

Moccia [18], in order to investigate their influence on the calculated 6DCSs. The study is performed for a projectile energy of $E_s = 250$ eV in a coplanar geometry, with a scattering angle of $\theta_s = 0°$ and equal ejected electron energies $E_1 = E_2 = 10$ eV, for the double ionization of the water molecule oriented along the direction $(\alpha, \beta, \gamma) = (0, 0, 0)$. The corresponding results are presented in Figure 4.13.

For the $1b_1$ orbital (Figures 4.13(a) and 4.13(b)), it is observed that the two bound states yield angular distributions of similar shape; however, new maximum with an interesseting magnitude appear on the second lobe when using the new function (the amplitude corresponding to forward scattering is reduced, while that associated with back scattering is enhanced). In general, both distributions exhibit the characteristic signature of the two-step 1 (TS1) mechanism. In contrast, for the $2a_1$ orbital (Figures 4.13(c) and 4.13(d)), the angular distributions and magnitudes differ significantly. The calculation using Moccia's molecular orbital structure [18] yields higher magnitudes and reveals the TS1 mechanism with a back to back emission if we considere the center of the maximum lobe in addition of a dominant TS1 contribution for the middel lobe($60° - 300°$), whereas the use of the new molecular orbital [11] indicates the presence of SO–TS1 interferences. Similarly, for the $3a_1$ orbital (Figures 4.13(e) and 4.13(f)), it is observed that the maxima obtained using Moccia's molecular orbital [18] occur at $|\theta_1 - \theta_2| \approx 180°$, which corresponds to the signature of the SO mechanism. In contrast, the results obtained with

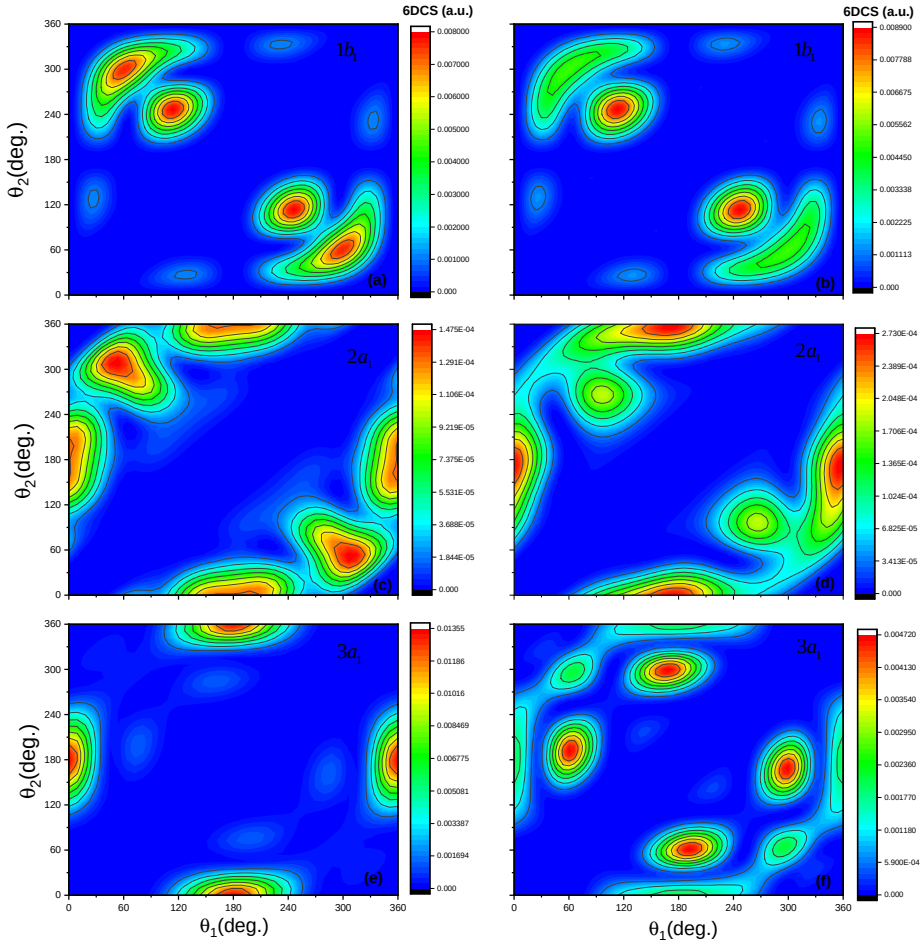


**Figure 4.13:** (Color online) Sixfold differential cross sections (expressed in a.u.) for the double ionization of the water molecule oriented in the direction $(\alpha, \beta, \gamma) = (0, 0, 0)$ for $\theta_s = 0°$. The ejected energies are $E_1 = E_2 = 10$ eV and $E_s = 250$ eV. Panels (a), (c), and (e) represent 2CWG theoretical results using the new MO [11], while (b), (d), and (f) represent 2CWG theoretical results using the Moccia MO [18].

the new molecular orbital [11] show that the TS1 mechanism can intervened in an interference phenomena, with a noticeably lower amplitude.

### 4.5.6 High Impact energy ($E_i = 1000eV$)

Here, we consider only the case $(\alpha, \beta, \gamma) = (0, 0, 0)$ to examine the difference between intermediate and high energies. The kinematic conditions are the same as in Figure 4.10, except that the incident energy here is $E_i = 1000$ eV.

We observe in Figure 4.14 for the four orbitals an increase in the magnitude of the 6DCS (The $1b_2$ orbital still exhibits a small 6DCS magnitude). In Figures 4.14(a) and 4.14(c), corresponding to the $1b_1$ and $3a_1$ orbitals, respectively, we obtained results

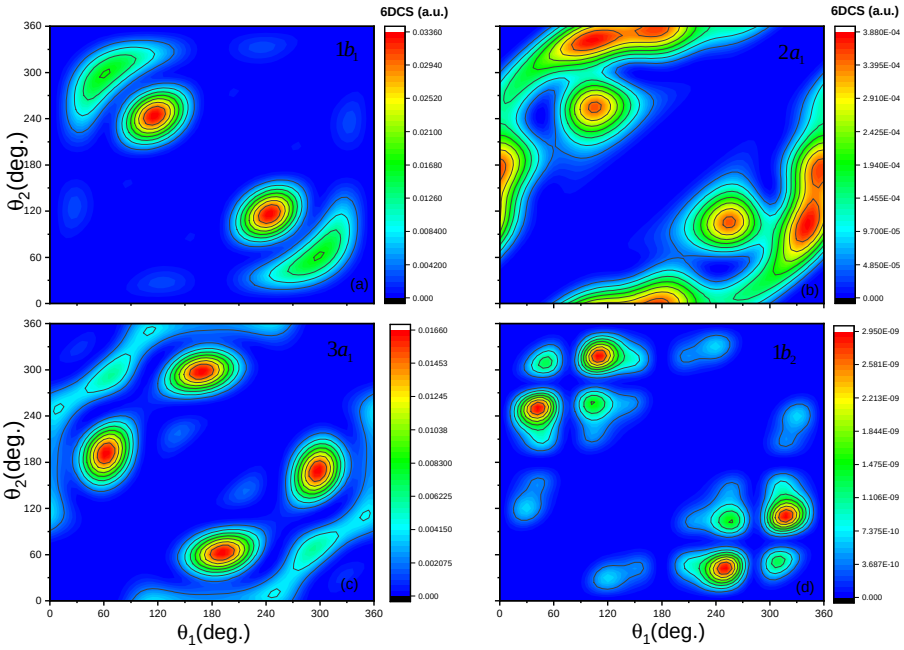


**Figure 4.14:** (Color online) Sixfold differential cross sections (expressed in (a.u.) for the double ionization of the water molecule oriented in the direction $(\alpha, \beta, \gamma) = (0, 0, 0)$ for $\theta_s = 0°$. The ejected energies are $E_1 = E_2 = 10$ eV and $E_i = 1000$ eV. (a) $1b_1$ orbital; (b) $2a_1$ orbital, (c) $3a_1$ orbital, and (d) $1b_2$ orbital.

similar to those shown in Figures 4.10(a) and 4.10(c). Hence, the TS1 mechanism is identified as the main contributing mechanism in this case. For the $2a_1$ orbital Figure 4.14(b), the structure of the 6DCS changes with aparition of a large hill containing two lobes of maxima indicating an interference process between SO and TS1 with a propable dominance of SO emission.

## 4.6 Conclusion

In this chapter, we have conducted a detailed theoretical investigation of the ionization of the water molecule by electron and positron impact. The first part focused on single ionization, where the M3CWZ model was applied to study the influence of the projectile charge over a range of low to intermediate energies. The results showed that for the outer orbitals, the model reproduces the experimental data well, whereas for the inner $2a_1$ orbital, the recoil peak is not captured, reflecting the limitations of the single-particle approximation in the molecular case . At lower energies (65–81 eV), post-collision interactions were found to play a crucial role, giving rise to a double-peak structure in the binary region for positron impact—a feature absent at higher energies.

In the second part, we extended the study to the double ionization of oriented wa-

ter molecule by electron impact using 2CWG model. The first Born approximation was employed together with a single-center molecular wave function [11] to describe the initial state. This wave function significantly affect the transition amplitudes compared with earlier theoretical studies and modified the shape of the 6DCS by presenting new peaks favorating intervention of added processes. This effect highlights the strong sensitivity of double ionization to the description of the initial state. Moreover, our analysis revealed clear signatures of the Shake-Off (SO) and Two-Step 1 (TS1) mechanisms, as well as a pronounced dependence of the cross sections on molecular orientation under the specific (e,3e) kinematical conditions investigated.

Overall, the present work demonstrates both the capabilities and the limitations of current theoretical models in describing ionization dynamics in water—one of the most relevant molecular targets in physics, chemistry, and biology. While the M3CWZ model provides reliable results for outer-shell single ionization and offers valuable insight into projectile charge effects, further refinement is still required for inner orbitals. In the case of double ionization, the 2CWG and BBK models capture the essential mechanisms and structural features but emphasize the importance of employing accurate initial-state wave functions and incorporating electron–electron correlation effects. These findings highlight the need for continued theoretical and experimental efforts, particularly since experimental data for molecular double ionization remain scarce and are currently limited to a few systems such as hydrogen and methane.

# Bibliography

[1] D. T. Goodhead and H. Nikjoo. *Int. J. Radiat. Biol.*, 55:513, 1989.

[2] H. Nikjoo, S. Uehara, W. E. Wilson, M. Hoshi, and D. T. Goodhead. *Int. J. Radiat. Biol.*, 73:355, 1998.

[3] A. Tamin, S. Houamer, T. Khatir, C. Dal Cappello, and L. U. Ancarani. *J. Chem. Phys.*, 161:164305, 2024.

[4] J. Zhou, E. Ali, M. Gong, S. Jia, Y. Li, Y. Wang, Z. Zhang, X. Xue, D. V. Fursa, I. Bray, X. Chen, D. Madison, A. Dorn, and X. Ren. *Phys. Rev. A*, 104:012817, 2021.

[5] M. Gong, X. Li, S. B. Zhang, S. Niu, X. Ren, E. Wang, A. Dorn, and X. Chen. *Phys. Rev. A*, 98:042710, 2018.

[6] M. Brauner, J. S. Briggs, and H. Klar. *J. Phys. B: At. Mol. Phys.*, 22:2265–2287, 1989.

[7] M. Chinoune, S. Houamer, C. Dal Cappello, and A. Galstyan. *J. Phys. B*, 49:205201, 2016.

[8] S. Mekhalfa, S. Houamer, A. Mansouri, I. Khiat, A. Tamin, C. Dal Cappello, and P.-A. Hervieux. *J. Electron Spectrosc. Relat. Phenom.*, 281:147545, 2025.

[9] C. Champion, D. Oubaziz, H. Aouchiche, Yu. V. Popov, and C. Dal Cappello. *Phys. Rev. A*, 81:032704, 2010.

[10] C. Dal Cappello, C. Champion, I. Kada, and A. Mansouri. *Phys. Rev. A*, 83:062716, 2011.

[11] H. Hafied, A. Eschenbrenner, C. Champion, M. F. Ruiz-López, C. Dal Cappello, I. Charpentier, and P. A. Hervieux. *Chem. Phys. Lett.*, 439:55, 2007.

[12] C. Champion, C. Dal Cappello, S. Houamer, and A. Mansouri. *Phys. Rev. A*, 73:012717, 2006.

[13] T. Khatir. PhD thesis, University of Setif 1, 2021.

[14] M. J. Frisch et al. *Gaussian 03, Revision B.05.* Gaussian, Inc., Wallingford, 2004.

[15] K. Kaufmann and W. Baumeister. *J. Phys. B*, 22:1, 1989.

[16] C. Dal Cappello, A. C. Roy, X. G. Ren, and R. Dey. *Nucl. Instrum. Methods Phys. Res. B*, 266:570–576, 2008.

[17] A. O. Bawagan, C. E. Brion, E. R. Davidson, and D. Feller. *Chem. Phys.*, 113:19, 1987.

[18] R. Moccia. *J. Chem. Phys.*, 40:2164, 1964.

[19] I. Kada. PhD thesis, University of Setif1, 2009.

[20] D. Oubaziz. PhD thesis, University of Tizi-ouzou, 2011.

[21] W. S. Benedict, N. Gailar, and E. K. Plyler. *J. Chem. Phys.*, 24:1139, 1956.

[22] S. A. Clough, Y. Beers, G. P. Klein, and L. S. Rothman. *J. Chem. Phys.*, 59:2254, 1973.

[23] B. Winter, R. Weber, W. Widdra, M. Dittmar, M. Faubel, and I. V. Hertel. *J. Phys. Chem. A*, 108:2625, 2004.

[24] A. Messiah. *Quantum Mechanics, Vol. 2.* Dunod, 1974.

[25] K. Bechane, S. Houamer, T. Khatir, A. Tamin, and C. Dal Cappello. *Phys. Rev. A.* 109:012812, 2024.

[26] O. Zaidi, A. Mansouri, S. Houamer, A. Tamin, T. Khatir, and C. Dal Cappello. *Eur. Phys. J. D*, 78:140, 2024.

[27] I. Khiat, S. Houamer, I. Kada, S. Mekhalfa, A. Tamin, and C. Dal Cappello. *Eur. Phys. J. D*, 79:68, 2025.

[28] D. H. Madison and O. Al-Hagan. *J. At. Mol. Opt. Phys.*, 2010:367180, 2010.

[29] A. Tamin. PhD thesis, University of Setif1, 2025.

[30] H. Hda, C. Dal Cappello, and J. Langlois. *Zeitschrift für Physik D*, 29:25, 1994.

[31] L. D. Landau and E. M. Lifshitz. *Quantum Mechanics: Non-Relativistic Theory.* Pergamon Press, Oxford, 1981.

[32] M. A. Kornberg and J. E. Miraglia. *Phys. Rev. A*, 48:3714, 1993.

[33] E. Ali, H. S. Chakraborty, and D. H. Madison. *J. Chem. Phys.*, 152:124303, 2020.

[34] D. S. Milne-Brownlie, B. Lohmann S. Cavanagh, C. Champion, P. A. Hervieux, and J. Hanssen. *Phys. Rev. A*, 69:032701, 2004.

[35] I. Toth, L. Nagy, and R. I. Campeanu. *Eur. Phys. J. D*, 68:369, 2014.

[36] R. D. DuBois and O. G. de Lucio. *Atoms*, 9:78, 2021.

[37] X. Ren, S. Amami, K. Hossen, E. Ali, C. Ning, J. Colgan, D. Madison, and A. Dorn. *Phys. Rev. A*, 95:022701, 2017.

[38] E. Acebal and S. Otranto. *Eur. Phys. J. D*, 73:91, 2019.

[39] T. Pflüger, O. Zatsarinny, K. Bartschat, A. Senftleben, X. Ren, J. Ullrich, and A. Dorn. *Phys. Rev. Lett.*, 110:153202, 2013.

[40] R. El Mir. PhD thesis, University of Lorraine, 2015.

[41] J. W. Cooper and R. W. Van Boeyen. *J. Phys. B*, 37:L77, 2004.

# General Conclusion

This thesis has provided a detailed theoretical analysis of single and double ionization processes in atomic and molecular systems, with particular focus on beryllium atom and water molecule under electron and positron impact. The core of our study was to apply Coulomb-wave-based models in ionization processes, namely, 2CWG, 2CWWM, and BBK for double ionization and M3CWZ for single ionization. These models incorporate post-collision interactions (and charge variability in the case of M3CWZ)to account for correlation effects and long-range Coulomb potential.

The first part of the work established the fundamental theoretical framework of scattering theory theory, introducing differential and total cross sections, and explored the formal solution of the Schrödinger equation using Green's functions. This framework then provided the foundation for the detailed studies of ionization processes.

Our study then turned to the mechanisms of single and double ionization, with particular attention to electron correlation and wavefunction-based approaches. In the case of single ionization, the (e,2e) process revealed its richness through the dependence of cross sections on geometry, energy, and projectile type. Double ionization, on the other hand, underscored the essential role of correlation and the coexistence of different mechanisms, such as shake-off and two-step processes. To account for these dynamics, theoretical frameworks like BBK and DWBA were examined, highlighting the importance of post-collision interactions and distortion effects in achieving an accurate description of the electron motion.

Building on this theoretical framework, our investigation extended to practical applications in atomic and molecular ionization, within the First Born Approximation (FBA). The study of double ionization of the beryllium atom using the BBK, 2CWG and 2CWWM models revealed the crucial role of post-collision interactions and electron correlation in shaping the Five-fold differential cross sections (FDCSs). Hence, two dominant mechanisms were clearly identified: the shake-off (SO) and two-step 1 (TS1) processes. Comparisons with existing theoretical results highlighted both the strengths and limitations of current treatments and underscored the challenges of accurately describing two-electron

ejection processes in few-body systems. Notably, while shake-off and TS1 mechanisms were clearly identified, the TS2 contribution was absent in our results, reflecting the constraints of the employed first Born approximation models.

For the double ionization of the oriented water molecule, the study was restricted to the 2CWG model due to the long computational time required for the calculations using BBK model, and because the main objective was to examine the influence of molecular orientation. Here, the analysis also demonstrated clear signatures of the shake-off (SO) and two-step 1 (TS1) mechanisms, as well as a pronounced sensitivity of sixfold differential cross sections (6DCS) to molecular orientation. The use of the LCAO-MO wavefunction significantly affected the transition amplitudes and the shapes of the 6DCS, emphasizing the critical role of accurate initial-state descriptions in molecular ionization. Notably, while the SO and TS1 mechanisms were clearly identified, the two-step 2 (TS2) contribution was absent from our results, reflecting the inherent limitations of the employed the FBA framework. Finally, it should be noted that, at this stage, no direct comparison with experiment is possible; however, we hope that in the near future, these theoretical predictions will be confirmed by experimental observations.

For the single ionization of the water molecule, calculations performed within the M3CWZ framework successfully reproduced the experimental features for the outer orbitals, especially for positron impact. However, discrepancies were observed for the inner $2a_1$ orbital at 250 eV, where a recoil peak reported in experiments was absent in both electron and positron impact cases. It is worth noting that the use of the LCAO-MO wavefunction in this context had only a minor effect compared to the case of double ionization.

Overall, this thesis demonstrates that Coulomb-wave-based models, when combined with post-collision interactions and charge variability, provide a realistic and reliable framework for studying single ionization processes at low and intermediate energies. While substantial progress has been achieved, certain challenges remain, particularly in the treatment of inner orbitals in molecules for both single and double ionization. Moreover, the reliance on the First Born Approximation (FBA) imposes inherent limitations in describing both processes, such as the absence of TS2 contributions and discrepancies in inner-shell ionization. Future work should therefore focus on incorporating higher-order treatments such as the Second Born Approximation (SBA), improving target descriptions, extending the models to full double-ionization calculations for molecules, and enabling systematic comparisons with experimental measurements.

# Appendix A

# The Scattering Amplitude $f_{B1}$ in BBK, 2CWG, and 2CWWM Models for Double Ionization

We consider the two active electron, where the $f_{B1}$ is given by:

$$f_{B1} = -\frac{1}{2\pi}\left\langle \phi_f(\vec{k}_1,\vec{k}_2,\vec{r}_1,\vec{r}_2)\, e^{i\vec{k_s}\cdot\vec{r}_0} \mid V' \mid e^{i\vec{k}_i\cdot\vec{r}_0}\, \Psi_{nlm}(\vec{r}_1,\vec{r}_2)\right\rangle \tag{A.1}$$

where the Coulomb interaction potential between the incident electron and the two active electrons is given by:

$$V' = -\frac{2}{r_0} + \frac{1}{|\vec{r}_0 - \vec{r}_1|} + \frac{1}{|\vec{r}_0 - \vec{r}_2|}. \tag{A.2}$$

## A.1 The Scattering Amplitude $f_{B1}$ in BBK model

In BBK model, the final state is given by:

$$\phi_f(\vec{k}_1,\vec{r}_1,\vec{k}_2,\vec{r}_2) = \frac{1}{\sqrt{2}}\Big[\phi_c^-(\vec{k}_1,\vec{r}_1)\phi_c^-(\vec{k}_2,\vec{r}_2) + \phi_c^-(\vec{k}_1,\vec{r}_2)\phi_c^-(\vec{k}_2,\vec{r}_1)\Big] C(a_{12},\vec{k}_{12},\vec{r}_{12}) \tag{A.3}$$

The integration over the projectile coordinates $\vec{r}_0$ can be performed analytically using the Bethe transformation:

$$\int \frac{e^{i\vec{k}\cdot\vec{r}_0}}{|\vec{r}_0 - \vec{r}_i|}\, d\vec{r}_0 = \frac{4\pi}{k^2} e^{i\vec{k}\cdot\vec{r}_i} \tag{A.4}$$

Then expression A.1 will be:

$$\begin{aligned} f_{B1} &= -\frac{2\sqrt{2}}{K}\left\langle \phi_c^-(\vec{k}_1,\vec{r}_1)\phi_c^-(\vec{k}_2,\vec{r}_2) C(a_{12},\vec{k}_{12},\vec{r}_{12}) \mid -2 + e^{i\vec{K}\cdot\vec{r}_1} + e^{i\vec{K}\cdot\vec{r}_2} \mid \Psi_{nlm}(\vec{r}_1)\Psi_{nlm}(\vec{r}_2)\right\rangle \\ &= I_0 + I_{01} + I_{02}. \end{aligned} \tag{A.5}$$

where $\vec{K} = \vec{k}_i - \vec{k}_s$. We use the version introduced by Miraglia that applies the Fourier transform, given by:

$$f(\vec{r}) = \frac{1}{(2\pi)^3} \int e^{i\vec{p}\cdot\vec{r}} d\vec{p} \int e^{-i\vec{p}\cdot\vec{r}'} f(\vec{r}') d\vec{r}' \tag{A.6}$$

The application of A.6 to the PCI term $C(\alpha_{12}, \vec{k}_{12}, \vec{r}_{12})$ gives:

$$C(\alpha_{12}, \vec{k}_{12}, \vec{r}_{12}) = \frac{1}{(2\pi)^3} \int e^{i\vec{p}\cdot\vec{r}_{12}} d\vec{p} \int e^{-i\vec{p}\cdot\vec{r}'_{12}} C(\alpha_{12}, \vec{k}_{12}, \vec{r}'_{12}) d\vec{r}'_{12} \tag{A.7}$$

hence the term $I_0$ in Eq. A.5 becomes:

$$\begin{aligned}
I_0 =& \frac{4}{K^2} \left\langle \phi_c^-(\vec{k}_1, \vec{r}_1)\phi_c^-(\vec{k}_2, \vec{r}_2) C(a_{12}, \vec{k}_{12}, \vec{r}_{12}) \;\middle|\; \Psi_{nlm}(\vec{r}_1)\Psi_{nlm}(\vec{r}_2) \right\rangle \\
&= \frac{4}{(2\pi)^3 K^2} \lim_{\lambda\to 0} \int \Big[ \int \phi_c(\vec{k}_1, \vec{r}_1) e^{i\vec{p}\cdot\vec{r}_1} \psi_{nlm}(\vec{r}_1) d\vec{r}_1 \\
&\quad \times \int \phi_c(\vec{k}_2, \vec{r}_2) e^{-i\vec{p}\cdot\vec{r}_2} \psi_{nlm}(\vec{r}_2) d\vec{r}_2 \\
&\quad \times \int e^{i(\vec{k}_{12}-\vec{p})\cdot\vec{r}'_{12}} e^{-i\vec{k}_{12}\cdot\vec{r}'_{12}} C^*(\alpha_{12}, \vec{k}_{12}, \vec{r}'_{12}) e^{-\lambda r'_{12}} d\vec{r}'_{12} \Big] d\vec{p} \\
&= \frac{4}{(2\pi)^{3/2} K^2} \lim_{\lambda\to 0} \int \Big[ \int \phi_c^-(\vec{k}_1, \vec{r}_1) e^{i\vec{p}\cdot\vec{r}_1} \psi_{nlm}(\vec{r}_1) d\vec{r}_1 \\
&\quad \times \int \phi_c^-(\vec{k}_2, \vec{r}_2) e^{-i\vec{p}\cdot\vec{r}_2} \psi_{nlm}(\vec{r}_2) d\vec{r}_2 \\
&\quad \times \int \phi_c^-(\alpha_{12}, \vec{k}_{12}, \vec{r}'_{12}) e^{i(\vec{k}_{12}-\vec{p})\cdot\vec{r}'_{12}} e^{-\lambda r'_{12}} d\vec{r}'_{12} \Big] d\vec{p}
\end{aligned} \tag{A.8}$$

The same calculation will be applying to $I_{01}$ and $I_{02}$:

$$\begin{aligned}
I_{01} =& \frac{2}{(2\pi)^{3/2} K^2} \lim_{\lambda\to 0} \int \Big[ \int \phi_c^-(\vec{k}_1, \vec{r}_1) e^{i(\vec{K}+\vec{p})\cdot\vec{r}_1} \psi_{nlm}(\vec{r}_1) d\vec{r}_1 \\
&\quad \times \int \phi_c^-(\vec{k}_2, \vec{r}_2) e^{-i\vec{p}\cdot\vec{r}_2} \psi_{nlm}(\vec{r}_2) d\vec{r}_2 \\
&\quad \times \int \phi_c^-(\alpha_{12}, \vec{k}_{12}, \vec{r}'_{12}) e^{i(\vec{k}_{12}-\vec{p})\cdot\vec{r}'_{12}} e^{-\lambda r'_{12}} d\vec{r}'_{12} \Big] d\vec{p}
\end{aligned} \tag{A.9}$$

$$\begin{aligned}
I_{02} =& \frac{2}{(2\pi)^{3/2} K^2} \lim_{\lambda\to 0} \int \Big[ \int \phi_c^-(\vec{k}_1, \vec{r}_1) e^{i\vec{p}\cdot\vec{r}_1} \psi_{nlm}(\vec{r}_1) d\vec{r}_1 \\
&\quad \times \int \phi_c^-(\vec{k}_2, \vec{r}_2) e^{-i(\vec{K}+\vec{p})\cdot\vec{r}_2} \psi_{nlm}(\vec{r}_2) d\vec{r}_2 \\
&\quad \times \int \phi_c^-(\alpha_{12}, \vec{k}_{12}, \vec{r}'_{12}) e^{i(\vec{k}_{12}-\vec{p})\cdot\vec{r}'_{12}} e^{-\lambda r'_{12}} d\vec{r}'_{12} \Big] d\vec{p}
\end{aligned} \tag{A.10}$$

## A.2 The Scattering Amplitude $f_{B1}$ in 2CWG model

In 2CWG model, the final state is given by:

$$\phi_f(\vec{k}_1,\vec{r}_1,\vec{k}_2,\vec{r}_2)=\frac{1}{\sqrt{2}}\Big[\phi_c^-(\vec{k}_1,\vec{r}_1)\phi_c^-(\vec{k}_2,\vec{r}_2)+\phi_c^-(\vec{k}_1,\vec{r}_2)\phi_c^-(\vec{k}_2,\vec{r}_1)\Big]\phi(\vec{k}_{12}) \tag{A.11}$$

where $\phi(\vec{k}_{12})$ is the Gamow factor $\phi_G(k_{12})$ (see chapter 3).

The integration over the projectile coordinates $\vec{r}_0$ in Eq. A.1 gives:

$$\begin{aligned} f_{B1} &= -\frac{2\sqrt{2}}{K}\left\langle \phi_c^-(\vec{k}_1,\vec{r}_1)\phi_c^-(\vec{k}_2,\vec{r}_2)\;\middle|\; -2+e^{i\vec{K}\cdot\vec{r}_1}+e^{i\vec{K}\cdot\vec{r}_2}\;\middle|\; \Psi_{nlm}(\vec{r}_1)\Psi_{nlm}(\vec{r}_2)\right\rangle\phi(\vec{k}_{12}) \\ &= I_0+I_{01}+I_{02} \end{aligned} \tag{A.12}$$

The calculation here is simpler and does not require applying the Fourier transform; hence, the expressions for $I_0$, $I_{01}$, and $I_{02}$ are given by:

$$I_0=\frac{4\sqrt{2}}{K^2}\phi(\vec{k}_{12})\int\phi_c^-(\vec{k}_1,\vec{r}_1)\psi_{nlm}(\vec{r}_1)d\vec{r}_1\times\int\phi_c^-(\vec{k}_2,\vec{r}_2)\psi_{nlm}(\vec{r}_2) \tag{A.13}$$

$$I_{01}=\frac{2\sqrt{2}}{K^2}\phi(\vec{k}_{12})\int\phi_c^-(\vec{k}_1,\vec{r}_1)e^{i\vec{K}\cdot\vec{r}_1}\psi_{nlm}(\vec{r}_1)d\vec{r}_1\times\int\phi_c^-(\vec{k}_2,\vec{r}_2)\psi_{nlm}(\vec{r}_2) \tag{A.14}$$

$$I_{02}=\frac{2\sqrt{2}}{K^2}\phi(\vec{k}_{12})\int\phi_c^-(\vec{k}_1,\vec{r}_1)\psi_{nlm}(\vec{r}_1)d\vec{r}_1\times\int\phi_c^-(\vec{k}_2,\vec{r}_2)e^{i\vec{K}\cdot\vec{r}_2}\psi_{nlm}(\vec{r}_2) \tag{A.15}$$

For the calculation of $f_{B1}$ using the 2CWWM model, the procedure is the same as in the 2CWG model, except that here we multiply by the Ward–Macek factor $\phi_{WM}(k_{12},r_{12ave})$ instead of the Gamow factor.